Shear Flow Through a Cascade

W. R. HAWTHORNE and W. D. ARMSTRONG

(*Cambridge University*)

SUMMARY: When a flow with a non-uniform velocity passes through a cascade, the blades impose on each layer of the flow local pressure changes which are roughly proportional to the dynamic head in the layer. This results in local pressure differences which, within the blade passages, produce rotational secondary flows and which also cause overall spanwise accelerations and displacements. These effects are analysed for frictionless flow by treating the blade row as an actuator plane whose outlet angle is determined by the secondary velocities in the blade passages.

At low outlet angles or large deflections the secondary flows effectively control the downstream flow angles. When the outlet angle is large the displacement effect can result in downstream flow angles of opposite sign to those induced by the secondary flow alone.

Measurements on cascades with small spanwise variations induced in the approaching stream confirm the main predictions of the first order theory.

1. Introduction

Flow with a non-uniform velocity through a cascade of aerofoils is of interest in the theory of axial-flow turbo-machines because the non-uniform flow in the boundary layer region near the annular walls causes a loss in efficiency and a reduction of the effective area for flow.

In some theoretical[1], [2] approaches to the study of three-dimensional flow in turbo-machinery use has been made of the actuator disc concept in which the blade row is replaced by an infinitely thin axially symmetrical disc which, as in propeller theory, imposes a sudden change. More detailed studies[3], [4] of the behaviour of the fluid in the passages between the blades have shown that, in regions of initially non-uniform flow, secondary velocities normal to the main direction of flow are generated, with consequent changes in the lift and circulation about the blades.

This paper describes a theoretical and experimental study of the flow through a cascade of untwisted aerofoils placed in a wind tunnel of rectangular cross section in which the approach velocity was varied artificially in the spanwise direction only. The variation in velocity was obtained by placing an obstruction upstream, which gave a two-dimensional wake which was symmetrical about the

Received June 1955

[Aeronautical Quarterly, Vol. VII, November 1956]

centre of the blade span. The velocity in the wake varied approximately sinusoidally in the spanwise direction.

The non-uniform flow in the wake produced secondary flows in the blade passages which altered the circulation about the blades, and caused the angle of flow leaving the blades to depart from the angle usually measured in uniform flow. As the secondary flows were not large, the theory of Ref. 4 could be used to predict the variation in outlet angle.

The row of blades was then imagined to be an actuator plane, which produced a deflection of the flow and which had an outlet angle at the trailing edge position given by the two-dimensional value modified to take into account the effect of the secondary flow in the blade passages. This enabled the flow angles and velocities far downstream to be determined and compared with the results of the experiments.

The theory is developed for inviscid, incompressible flow and the experiments were performed with turbine or accelerating cascades to reduce the possibility of boundary layer separation on the blades.

NOTATION

a velocity decrement defined by equation (23)

C constant

$K = 1 - \exp(-\pi x_e/\delta)$

$m = t^2/(2+t^2)$

$m' = t^2(1+K)/[2+(1+K)t^2]$

p_0 stagnation pressure

s blade spacing

$s' = s\cos\bar{\alpha}_{02}$

$t = \tan\alpha_{02}$ (independent of z)

$t' = t - \tan\alpha_{02}$ (a function of z)

$t'' = t - \tan\alpha_2$

u, v, w velocity components (*see* Fig. 1)

$u' = \frac{1}{2}(u_2 - u_1)$

$\bar{u}_1$ value of u_1 outside the non-uniform region

$\bar{u}_2$ value of u_2 outside the non-uniform region

u_e axial velocity at the trailing edge

$u_d = u - u_2$

$U_1 = u_1 \sec\alpha_1$

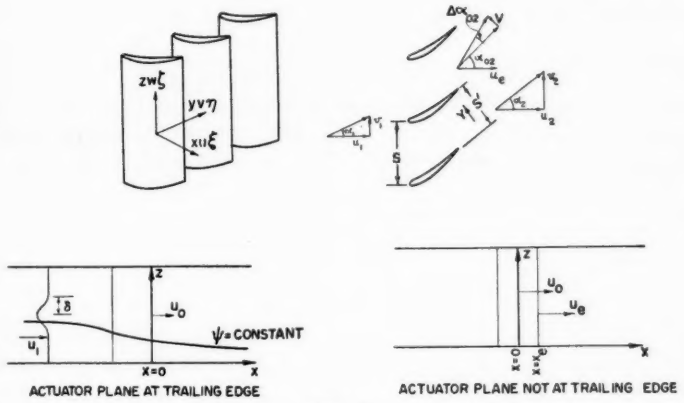

Fig. 1.
Diagrams showing nomenclature.

V velocity vector with components u, v, w

$\overline{V}$ average value of velocity V in the Y-direction

x, y, z Cartesian co-ordinates (*see* Fig. 1)

x_e distance from actuator plane location to the trailing edge

Y co-ordinate normal to the undisturbed stream at outlet

α_1 upstream angle of approach to the cascade

α_{02} the angle at which the flow leaves the trailing edge

$\overline{\alpha}_{02}$ the angle at which the flow leaves the trailing edge outside the non-uniform region

$\delta = \frac{1}{2}$ (boundary layer thickness)

ε deflection $(\overline{\alpha}_{02} - \alpha_1)$

ρ density

ψ stream function

χ stream function of the secondary motion

$\boldsymbol{\Omega}$ curl **V**, vorticity vector with components ξ, η, ζ

ξ, η, ζ vorticity components

Suffixes

0 refers to conditions at the actuator plane

1 refers to conditions upstream of the cascade

2 refers to conditions downstream of the cascade

WAYNE STATE UNIVERSITY LIBRARIES
KRESGE-HOOKER SCIENCE LIBRARY

2. Actuator Plane Theory

2.1. General Solution

The nomenclature and co-ordinate system used is shown in Fig. 1. The flow is separated into two regimes on either side of the actuator plane. In each regime the equations of motion and continuity may be written in the form

$$\text{grad}\left(\frac{p_0}{\rho}\right)=\mathbf{V}\times\boldsymbol{\Omega} \quad . \quad . \quad . \quad . \quad . \quad . \quad (1)$$

$$\text{and div } \mathbf{V}=0 \quad . \quad . \quad . \quad . \quad . \quad . \quad . \quad (2)$$

where p_0 is the stagnation pressure, ρ the density, $\mathbf{V}$ the velocity vector with components u, v and w and $\boldsymbol{\Omega}=\text{curl } \mathbf{V}$, the vorticity vector, with components ξ, η, ζ. These velocity and vorticity components correspond to the Cartesian co-ordinates x, y, z, where z is the spanwise direction (*see* Fig. 1). If the cascade is assumed to be many-bladed and therefore infinite in the $y-$direction, variations in this direction will not occur and the components of vorticity may be written

$$\left.\begin{aligned}\xi&=-\frac{\partial v}{\partial z}\\ \eta&=\frac{\partial u}{\partial z}-\frac{\partial w}{\partial x}\\ \zeta&=\frac{\partial v}{\partial x}.\end{aligned}\right\} \quad . \quad . \quad . \quad . \quad . \quad . \quad (3)$$

The $z-$component of equation (1) therefore becomes

$$\frac{\partial\,(p_0/\rho)}{\partial z}=u\eta-v\xi$$

$$=u\eta+v\,\frac{\partial v}{\partial z}. \quad . \quad . \quad . \quad . \quad . \quad . \quad . \quad (4)$$

The continuity equation becomes

$$\frac{\partial u}{\partial x}+\frac{\partial w}{\partial z}=0. \quad . \quad . \quad . \quad . \quad . \quad . \quad . \quad . \quad (5)$$

It is therefore possible to select a stream function $\psi(x, z)$ which is independent of y and which enables the intercepts of the stream surface, $\psi=$constant, on any plane $y=$constant to be determined. From equation (5),

$$\frac{\partial\psi}{\partial x}=-w \qquad \text{and} \qquad \frac{\partial\psi}{\partial z}=u. \quad . \quad . \quad . \quad (6)$$

Since the pressure is independent of y, the second Euler equation becomes

$$u\frac{\partial v}{\partial x}+w\frac{\partial v}{\partial z}=0, \quad . \quad . \quad . \quad . \quad . \quad . \quad (7)$$

whence v is constant along a stream surface intercept, $\psi=$constant.

The second Helmholtz equation yields

$$u\frac{\partial \eta}{\partial x}+w\frac{\partial \eta}{\partial z}=\xi\frac{\partial v}{\partial x}+\zeta\frac{\partial v}{\partial z} \quad . \quad . \quad . \quad . \quad . \quad (8)$$

and, on substitution for ξ and ζ from equation (3), the right hand side equates to zero. Hence η is also constant for constant ψ.

The solution of the equations of motion for each regime is generally intractable without some approximation. If the non-uniformity of velocity in the approaching stream is also small, then terms such as $\partial u/\partial z$, $\partial v/\partial z$ and η are small, and therefore the spanwise velocity or w/u is also small. Since, from equations (3) and (7),

$$\zeta=\frac{\partial v}{\partial x}=-\frac{w}{u}\frac{\partial v}{\partial z}, \quad . \quad . \quad . \quad . \quad . \quad . \quad (7a)$$

ζ and the variation of v with x are the product of two small terms and may be neglected.

Similarly from equation (8)

$$\frac{\partial \eta}{\partial x}=-\frac{w}{u}\frac{\partial \eta}{\partial z}, \quad . \quad . \quad . \quad . \quad . \quad . \quad (8a)$$

and the variation of η with x may also be neglected. This type of approximation was suggested by Ruden[5] for annular cascades. An exact analysis[2] of the flow through an annular cascade confirms that it is reasonable.

Since the vorticity components are now, to the first approximation, independent of x, physical consideration of the axial velocity field induced by the $\eta-$components of vorticity on both sides of the actuator plane leads to the result that at the plane, $x=0$, the axial velocity is the mean of the values at $x=-\infty$ and $+\infty$.

$$i.e. \quad u_0=\tfrac{1}{2}(u_1+u_2). \quad . \quad . \quad . \quad . \quad . \quad (9)$$

Across the actuator plane, by continuity,

$$u_{01}=u_{02}=u_0. \quad . \quad . \quad . \quad . \quad . \quad . \quad (10)$$

Since the flow is inviscid, p_0 is unchanged, and since there are no blade forces in the $z-$direction,

$$w_{01}=w_{02}=w_0. \quad . \quad . \quad . \quad . \quad (11)$$

The second of these conditions and the assumptions for η and v may be applied to equation (4) to give

$$u_0\eta_1+v_1\frac{\partial v_1}{\partial z}=u_0\eta_2+v_2\frac{\partial v_2}{\partial z}, \quad . \quad . \quad . \quad . \quad . \quad (12)$$

where the values at $x=\pm\infty$ may be used for η_1 and η_2, and v_1 is obtained from the known value of the upstream angle of approach to the cascade, α_1, *i.e.* $v_1=u_1\tan\alpha_1$. To obtain v_2, knowledge of the outlet angle at the trailing elge of the blades is assumed.

There is some evidence to show that the actuator plane should be located at the centre of pressure of the blading. The equations are somewhat simpler when it is located at the trailing edge and this position will be assumed first. The modifications required in the analysis for other locations are given in the Appendix. With the actuator plane at the trailing edge, $v_2=u_0\tan\alpha_{02}$, where α_{02} is the angle at which the flow leaves the trailing edge.

Substituting in equation (12),

$$u_0\frac{du_1}{dz}+u_1\tan\alpha_1\frac{d}{dz}(u_1\tan\alpha_1)=u_0\frac{du_2}{dz}+u_0\tan\alpha_{02}\frac{d}{dz}(u_0\tan\alpha_{02}) \quad . \quad (13)$$

Taken with equation (9), this gives a non-linear first order differential equation for u_2 which may be solved numerically or graphically.

The equation shows that, if α_1 and α_{02} are independent of z, then outside the region in which u_1 varies with z, u_0 and u_2 are constant. This implies that the width of the non-uniform region, *i.e.* thickness of wake or boundary layer, does not increase, and is a consequence of the approximations made in deriving equation (12).

Equation (13) may be linearised by writing $u_2-u_1=2u'$ and assuming that u' is small compared to u_1, so that terms of order u'^2 may be neglected. Then

$$u_1(2+\tan^2\alpha_{02})\frac{du'}{dz}+u'\frac{d}{dz}(u_1\tan^2\alpha_{02})=u_1\tan\alpha_1\frac{d}{dz}(u_1\tan\alpha_1)-$$
$$-u_1\tan\alpha_{02}\frac{d}{dz}(u_1\tan\alpha_{02}). \quad . \quad (14)$$

With $\tan\alpha_1$ and $\tan\alpha_{02}$ constant this may be solved to give

$$u'=\tfrac{1}{2}\left(\frac{\cos^2\alpha_{02}}{\cos^2\alpha_1}-1\right)u_1+\tfrac{1}{2}Cu_1^{-m}$$

or
$$u_2=\frac{\cos^2\alpha_{02}}{\cos^2\alpha_1}u_1+Cu_1^{-m}, \quad . \quad . \quad . \quad . \quad . \quad (15)$$

where $m=t^2/(2+t^2)$ and $t=\tan\alpha_{02}$, and C is a constant which may be found by applying the continuity condition.

Now $v_2 = u_0 \tan \alpha_{02} = u_2 \tan \alpha_2$, and with the same degree of approximation

$$\frac{\tan \alpha_{02} - \tan \alpha_2}{\tan \alpha_{02}} = \tfrac{1}{2}\left[\frac{\cos^2 \alpha_{02}}{\cos^2 \alpha_1} - 1\right] + \tfrac{1}{2}C u_1^{-(m+1)} \quad . \quad . \quad (16)$$

2.2. Approximate Solution for α_1 Constant and α_{02} Varying Slightly

When α_{02} varies, an approximate solution may be obtained by writing $\tan \alpha_{02} = t + t'$, where t is independent of z and t' varies with z. Assuming that t' is small, so that terms in t'^2 and $u't'$ may be neglected, equation (14) becomes, with $\tan \alpha$ constant,

$$(2 + t^2)\frac{du'}{dz} + \frac{u't^2}{u_1}\frac{du_1}{dz} = \tan^2 \alpha_1 \frac{du_1}{dz} - t^2 \frac{du_1}{dz} - \frac{t}{u_1}\frac{d(u_1^2 t')}{dz}. \quad . \quad (17)$$

If $\tan \alpha_2$ may be written $\tan \alpha_2 = t + t''$,

then, since $v_2 = u_0 \tan \alpha_{02} = u_2 \tan \alpha_2$,

$$(u_1 + u')(t + t') = (u_1 + 2u')(t + t'').$$

Whence, neglecting terms in $u't'$ and $u't''$,

$$u't = u_1(t' - t''). \quad . \quad . \quad . \quad . \quad . \quad (18)$$

Substituting for u' in equation (17),

$$\frac{d}{dz}(u_1 t'') + mt''\frac{du_1}{dz} = -\frac{m}{t}(\tan^2 \alpha_1 - t^2)\frac{du_1}{dz} + \frac{2u_1 t'}{u_1^m}\frac{du_1^m}{dz} + (m+1)\frac{d(u_1 t')}{dz} \quad (19)$$

If outside the non-uniform region u_1 reaches a constant value $\bar{u}_1$ and $t' \longrightarrow 0$, the solution is

$$t'' = -\frac{t}{2}\left(\frac{\cos^2 \bar{\alpha}_{02}}{\cos^2 \alpha_1} - 1\right)\left(1 - \left[\frac{\bar{u}_1}{u_1}\right]^{m+1}\right) + (m+1)t' + (1-m)\left(\frac{\bar{u}_1}{u_1}\right)^{m+1} \int_1^{u_1/\bar{u}_1} \left(\frac{u_1}{\bar{u}_1}\right) t' d\left(\frac{u_1}{\bar{u}_1}\right)^m$$

. . . . . (20)

omitting an arbitrary constant.

The last term, which is in general small, may be further simplified by noting that, if the variation in u_1 is small,

$$u_1^m \simeq \bar{u}_1^m \left[1 - m\left(1 - \frac{u_1}{\bar{u}_1}\right)\right].$$

Hence the equation becomes

$$t'' = -\frac{t}{2}\left(\frac{\cos^2\bar{\alpha}_{02}}{\cos^2\alpha_1} - 1\right)\left(1 - \left[\frac{\bar{u}_1}{u_1}\right]^{m+1}\right) + (m+1)\,t' + m\,(1-m)\left(\frac{\bar{u}_1}{u_1}\right)^{m+1}\int_1^{u_1/\bar{u}_1}\left(\frac{u_1}{\bar{u}_1}t'\right)d\left(\frac{u_1}{\bar{u}_1}\right) \quad . \quad . \quad . \quad . \quad . \quad (21)$$

omitting an arbitrary constant.

The expression for u' in equation (17) may be similarly treated to give

$$u_2 = u_1 + 2u' = \frac{\cos^2\bar{\alpha}_{02}}{\cos^2\alpha_1}\left[u_1 - \bar{u}_1\left(\frac{\bar{u}_1}{u_1}\right)^m\right] + \bar{u}_2\left(\frac{\bar{u}_1}{u_1}\right)^m -$$

$$- 2mu_1t'/t - 2m\,(1-m)\,u_1\left(\frac{\bar{u}_1}{u_1}\right)^{m+1}\int_1^{u_1/\bar{u}_1}\left(\frac{u_1}{\bar{u}_1}\frac{t'}{t}\right)d\left(\frac{u_1}{\bar{u}_1}\right), \quad . \quad (22)$$

where $\bar{u}_2$ is the value of u_2 far outside the non-uniform region where it is assumed that $t' \longrightarrow 0$. The value of $\bar{u}_2$ is determined from continuity. Outside the region of varying u_1, $\bar{u}_2 - u_2 = 2m\bar{u}_1\,t'/t$, so that u_2 will rise or fall to its final value beyond the non-uniform region, depending on the sign of t'.

2.3. The Effect of Secondary Flow in the Blades

The secondary flow in the passages between the blades alters the value of α_{02} from that found in two-dimensional flow. The variation in α_{02} is calculated by the method suggested in Ref. 4. The calculations are performed for a non-uniform flow which varies sinusoidally within a "boundary layer" region. The velocity within the boundary layer region of thickness 2δ is given by

$$\frac{u_1}{\bar{u}_1} = 1 - \frac{a}{\bar{u}_1}\left[1 + \cos\left(\frac{\pi z}{\delta}\right)\right] \quad . \quad . \quad . \quad . \quad . \quad (23)$$

The stream function χ of the secondary motion within the blade passages is given by

$$\frac{\partial^2\chi}{\partial Y^2} + \frac{\partial^2\chi}{\partial Z^2} = -2\varepsilon\frac{dU_1}{dZ}, \quad . \quad . \quad . \quad . \quad (24)$$

where ε is the deflection $(\bar{\alpha}_{02} - \alpha_1)$, U_1 the approach velocity $(= u_1 \sec\alpha_1)$, and Y is the co-ordinate normal to the unperturbed direction of the stream at outlet, *i.e.* a direction making an angle $\bar{\alpha}_{02}$ with the x-axis (Fig. 1). The boundary conditions are $\chi = 0$ at $Y = 0$ and s', where $s' = s\cos\bar{\alpha}_{02}$ and s is the blade spacing, and $\chi = 0$ at $z = 0$ and $z = \infty$. The latter boundary condition implies that the region of uniform flow outside the "boundary layer" region is large.

Writing

$$2\varepsilon = \sum_{n=1,3,5}^{\infty}\frac{8\varepsilon}{n\pi}\sin n\pi\frac{Y}{s'}, \quad . \quad . \quad . \quad . \quad . \quad (25)$$

a solution is of the form

$$\chi = \Sigma\,\chi_n(z)\sin n\pi\frac{Y}{s'}. \quad . \quad . \quad . \quad . \quad . \quad (26)$$

This satisfies the boundary conditions at $Y=0$ and s' and gives,

when $0<z<\delta$, $$\chi_n'' - \left(\frac{n\pi}{s'}\right)^2 \chi_n = -\frac{8\varepsilon}{n\pi}\frac{dU_1}{dz}, \quad . \quad . \quad . \quad . \quad . \quad (27a)$$

and when $z>\delta$, $$\chi_n'' - \left(\frac{n\pi}{s'}\right)^2 \chi_n = 0. \quad . \quad . \quad . \quad . \quad . \quad (27b)$$

When solutions to these two equations for χ_n and χ_n' are matched at $z=\delta$:—

for $0<z<\delta$,

$$\chi_n = \frac{8\varepsilon s'}{(n\pi)^2}\left\{\sinh\frac{n\pi z}{s'}\int_z^\delta \frac{dU_1}{d\lambda}e^{-(n\pi\lambda/s')}d\lambda + e^{-n\pi z/s'}\int_0^z \frac{dU_1}{d\lambda}\sinh\left(\frac{n\pi\lambda}{s'}\right)d\lambda\right\}. \quad (28a)$$

and for $z>\delta$,

$$\chi_n = \frac{8\varepsilon s'}{(n\pi)^2}e^{-n\pi z/s'}\int_0^\delta \frac{dU_1}{d\lambda}\sinh\left(\frac{n\pi\lambda}{s'}\right)d\lambda. \quad . \quad . \quad . \quad . \quad (28b)$$

These equations satisfy the boundary conditions at $z=0$ and ∞. Now the velocity V in the $Y-$direction is $\partial\chi/\partial z$. Hence the average value of V at any z is given by

$$\bar{V} = \frac{1}{s'}\int_0^{s'} V\,dy = \frac{2}{\pi}\Sigma\frac{\chi_n'}{n} \quad . \quad . \quad . \quad . \quad . \quad (29)$$

and the maximum value by

$$V_{max} = -\Sigma(-1)^{\frac{n+1}{2}}\chi_n' \quad . \quad . \quad . \quad . \quad (29a)$$

and the corresponding change in average outlet angle (Fig. 1) by

$$\Delta\alpha_{02} = \frac{\bar{V}}{u_0\sec\bar{\alpha}_{02}} \simeq \frac{2}{\pi}\frac{\cos\bar{\alpha}_{02}}{u_1}\Sigma\frac{\chi_n'}{n}. \quad . \quad . \quad . \quad (30)$$

The change in maximum outlet angle

$$\Delta\alpha_{02max} \simeq -\frac{\cos\bar{\alpha}_{02}}{u_1}\Sigma(-1)^{\frac{n+1}{2}}\chi_n' \quad . \quad . \quad . \quad . \quad (30a)$$

Now $$r' = \Delta\tan\alpha_{02} \simeq \sec^2\bar{\alpha}_{02}\Delta\alpha_{02}$$

$$= \frac{2\sec\bar{\alpha}_{02}}{\pi u_1}\Sigma\frac{\chi_n'}{n}. \quad . \quad . \quad . \quad . \quad . \quad . \quad (31)$$

Using the value of u_1 from equation (23) and differentiating equation (28*a*):—

For $0 < z < \delta$,

$$\chi_n' = \frac{8\varepsilon a \sec\alpha_1}{n\pi}\left\{\cosh\left(\frac{n\pi z}{s'}\right)\int_z^\delta \sin\frac{\pi\lambda}{\delta}\,e^{-\frac{n\pi\lambda}{s'}}\,d\left(\frac{\pi\lambda}{\delta}\right) - \right.$$

$$\left. - e^{-\frac{n\pi z}{s'}}\int_0^z \sin\left(\frac{\pi\lambda}{\delta}\right)\sinh\left(\frac{n\pi\lambda}{s'}\right)d\left(\frac{\pi\lambda}{\delta}\right)\right\}$$

$$= \frac{8\varepsilon a}{n\pi}\,\frac{\sec\alpha_1}{\left(1+\left[\frac{n\delta}{s'}\right]^2\right)}\left\{\cos\left(\frac{\pi z}{\delta}\right)+e^{-\frac{n\pi\delta}{s'}}\cosh\left(\frac{n\pi z}{s'}\right)\right\}. \quad . \quad . \quad . \quad (32a)$$

For $z > \delta$,

$$\chi_n' = -\frac{8\varepsilon a}{n\pi}\,\frac{\sec\alpha_1}{1+\left(\frac{n\delta}{s'}\right)^2}\,e^{-\frac{n\pi z}{s'}}\sinh\left(\frac{n\pi\delta}{s'}\right). \quad . \quad . \quad . \quad (32b)$$

Hence, for $0 < z < \delta$,

$$t'\left(\frac{u_1}{\bar{u}_1}\right) = 16\varepsilon\sec\alpha_{02}\sec\alpha_1\left(\frac{a}{\bar{u}_1}\right)\sum_{n=1,3,5}\frac{\left(\cos\frac{\pi z}{\delta}+e^{-\frac{n\pi\delta}{s'}}\cosh\frac{n\pi z}{s'}\right)}{n^2\pi^2\left[1+\left(\frac{n\delta}{s'}\right)^2\right]} \quad . \quad (33a)$$

and for $z > \delta$,

$$t' = -16\varepsilon\sec\alpha_{02}\sec\alpha_1\left(\frac{a}{\bar{u}_1}\right)\sum_{n=1,3,5}\frac{e^{-\frac{n\pi z}{s'}}\sinh\frac{n\pi\delta}{s'}}{n^2\pi^2\left[1+\left(\frac{n\delta}{s'}\right)^2\right]} \quad . \quad . \quad (33b)$$

In general, terms above $n=1$ in these series are small enough to be neglected.

2.4. Approximate Solution for Downstream Angle

Equations (33*a*) and (33*b*), together with equation (21), enable the variation of angle far downstream to be determined. The general behaviour is first shown by an approximate analysis. The integral term in equation (21) is neglected, as are terms above $n=1$ in equation (33*a*).

If $a/\bar{u}_1$ is small, then from equation (23),

$$1-\left(\frac{\bar{u}_1}{u_1}\right)^{m+1} = -(m+1)\frac{a}{\bar{u}_1}\left(1+\cos\frac{\pi z}{\delta}\right) \quad . \quad . \quad . \quad (34)$$

Therefore, for $z < \delta$,

$$t'' = \frac{t}{2}\left(\frac{\cos^2\bar{\alpha}_{02}}{\cos^2\alpha_1} - 1\right)(m+1)\frac{a}{\bar{u}_1}\left(1+\cos\frac{\pi z}{\delta}\right) + 16\,(m+1)\,(\bar{\alpha}_{02} - \alpha_1)\times$$

$$\times \sec\bar{\alpha}_{02}\sec\alpha_1\left(\frac{a}{\bar{u}_1}\right)\left(1+\frac{a}{\bar{u}_1}\left[1+\cos\frac{\pi z}{\delta}\right]\right)\left[\frac{\cos\frac{\pi z}{\delta} + e^{-\frac{\pi\delta}{s'}}\cosh\frac{\pi z}{s'}}{\pi^2\left(1+\left[\frac{\delta}{s'}\right]^2\right)}\right] . \quad (35)$$

2.5. Compressor Cascade

For a compressor cascade $|\alpha_{02}| < |\alpha_1|$, and for a turbine $|\alpha_{02}| > |\alpha_1|$, so that the signs of both terms on the right hand side of equation (35) are reversed as the cascade changes from a compressor to a turbine. For a compressor cascade the first term, representing the effect of the spanwise displacement which occurs throughout the field of flow, is positive for all values of z in the non-uniform region. The second term is negative for small values of z, is positive at the boundary where $z=\delta$ and passes through zero at the point where $\cos(\pi z/\delta) + e^{-\pi\delta/s'}\cosh(\pi z/s') = 0$. It is possible therefore, to have either positive or negative values of t'', *i.e.* the change in $\tan\alpha_2$ from some constant value well outside the non-uniform region, at and near $z=0$, but the value will always be positive at $z=\delta$. A positive value of t'', *i.e.* an increase of α_2 above the main stream value, implies an "under-turning" or decrease in deflection, a negative value an increase. At $z=0$ the condition that t'' is positive and hence that there are no negative values of t'' and there is no increase in deflection at any z is, from equation (35),

$$\frac{\sin\bar{\alpha}_{02}\cos\alpha_1}{16\,(\alpha_1 - \bar{\alpha}_{02})}\left[\frac{\cos^2\alpha_{02}}{\cos^2\alpha_1} - 1\right] > \frac{(1+2\,a/\bar{u}_1)\,(1+e^{-\pi\delta/s'})}{\pi^2\,[1+(\delta/s')^2]} \quad . \quad . \quad (36)$$

2.6. Turbine Cascade

For a turbine cascade, $|\alpha_{02}| > |\alpha_1|$, the effects are the opposite as far as the signs of t'' and the terms in equation (35) are concerned. However, a positive value of t'' implies "over-turning" or an increase in deflection, and expression (36) represents the condition that t'' is always negative and there is no *increase* in deflection at any z.

For both turbine and compressor cascades the secondary flow tends to increase the deflection at small values of z.

2.7. Numerical Illustrations

To illustrate the effect on angle, a number of calculations have been made, based on the sinusoidal velocity distribution of equation (23) and on equations (21) and (33). Fig. 2 shows results for a compressor cascade with $\alpha_1 = 50°$, $\alpha_{02} = 30°$ and

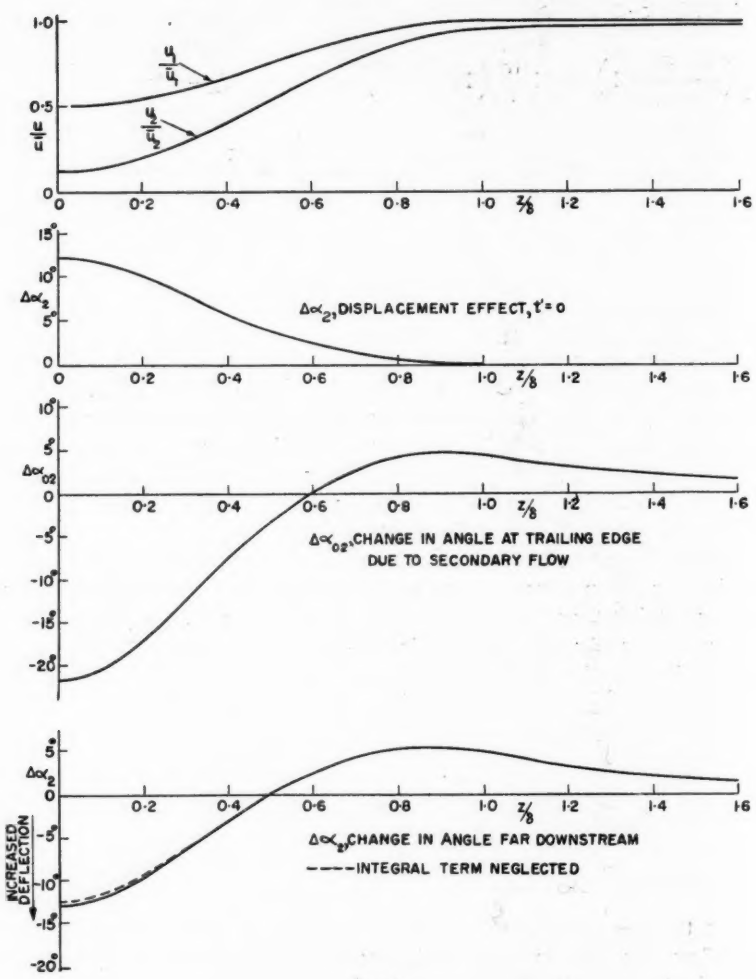

Fig. 2.

Downstream angles for compressor cascade.

$a/\bar{u}_1=0{\cdot}25$, $\alpha_1=50°$, $\alpha_{02}=30°$, $\delta/s'=0{\cdot}5$, $\delta/s=0{\cdot}433$.

$\delta/s'=0{\cdot}5$, for a velocity profile for which the value of u_1 at $z=0$ is half the main stream value, *i.e.* $a/\bar{u}_1=\frac{1}{4}$. The figure shows first the effect due to the spanwise displacement only (*i.e.* with $t'=0$). There is an increase of angle, *i.e.* a decrease of deflection in the wake. Next is shown the variation in angle at the trailing edge due to the secondary flow in the blade passage. There is first an increase in deflection at the centre of the wake which is reduced until a decrease in deflection is

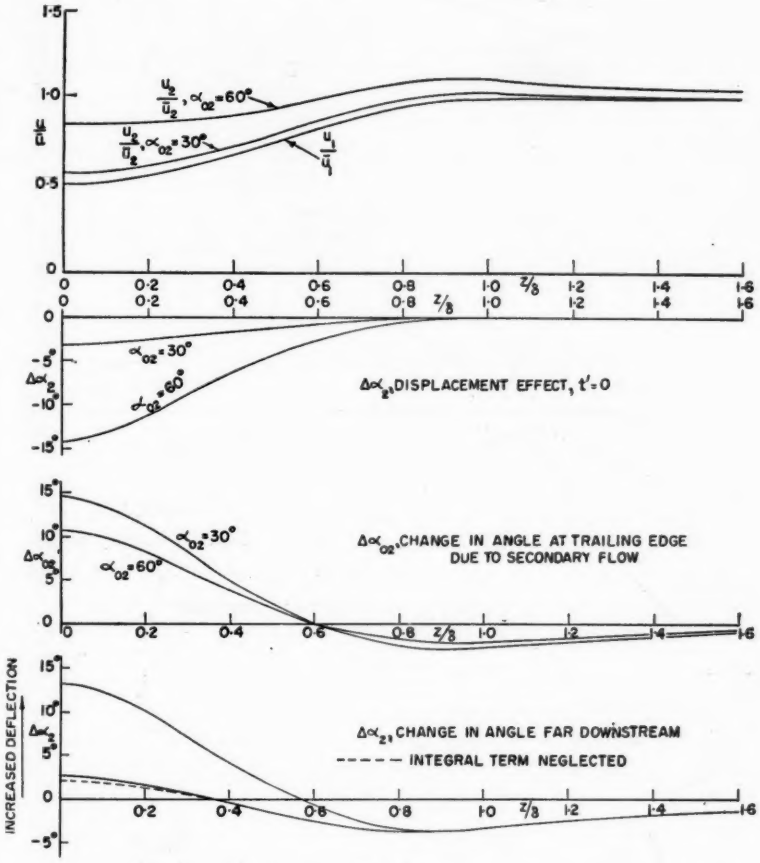

Fig. 3.

Downstream angles for two turbine cascades of 20° deflection.
$\alpha_1=10°$, $\alpha_{02}=30°$, $a/\bar{u}_1=0{\cdot}25$, $\delta/s'=0{\cdot}5$, $\delta/s=0{\cdot}433$
$\alpha_1=40°$, $\alpha_{02}=60°$, $a/\bar{u}_1=0{\cdot}25$, $\delta/s'=0{\cdot}5$, $\delta/s=0{\cdot}25$

noted at the edge of the wake. The combined effects which are not purely additive (*see* equation (21)) are finally shown in a curve at the bottom of Fig. 2. The slight effect of omitting the integral term in equation (21) is also shown.

Figure 3 shows the results for a very low deflection turbine cascade. Two sets of curves are shown; one for an outlet angle of 30°, for which the change of angle due to the secondary flow appears to dominate the variation of α_2 far downstream; in the other, for $\alpha_{02}=60°$, the displacement effects become more important. In both cases the deflection is 20°. In Figs. 2 and 3 the effect of neglecting the integral term in equation (21) is seen to be slight, and it is omitted in subsequent figures.

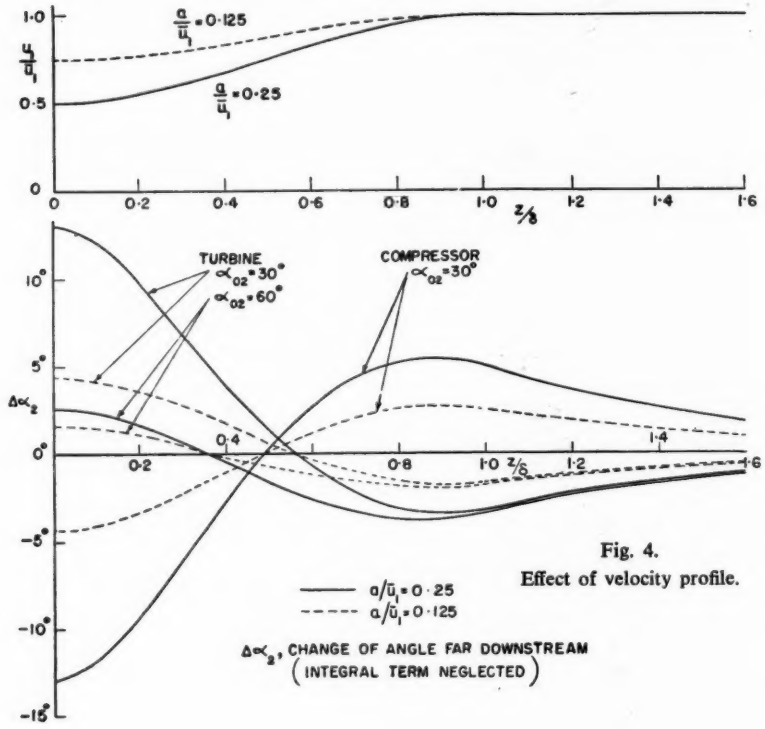

Fig. 4.
Effect of velocity profile.

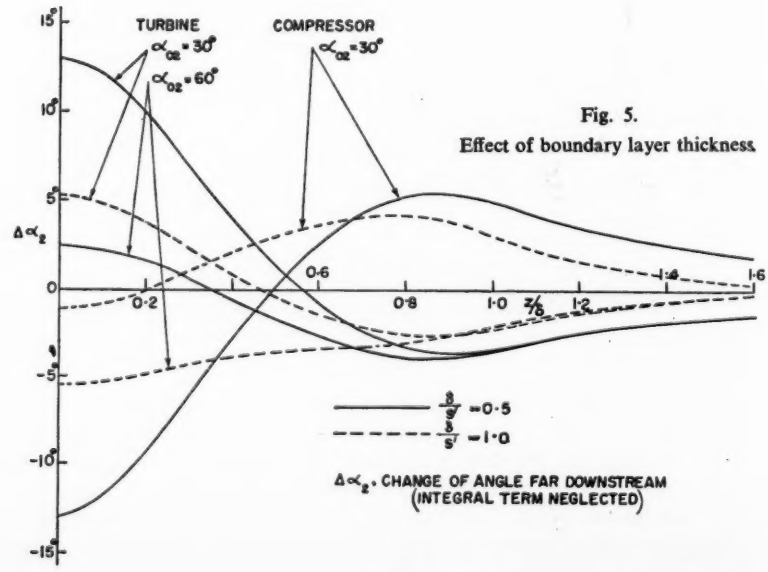

Fig. 5.
Effect of boundary layer thickness.

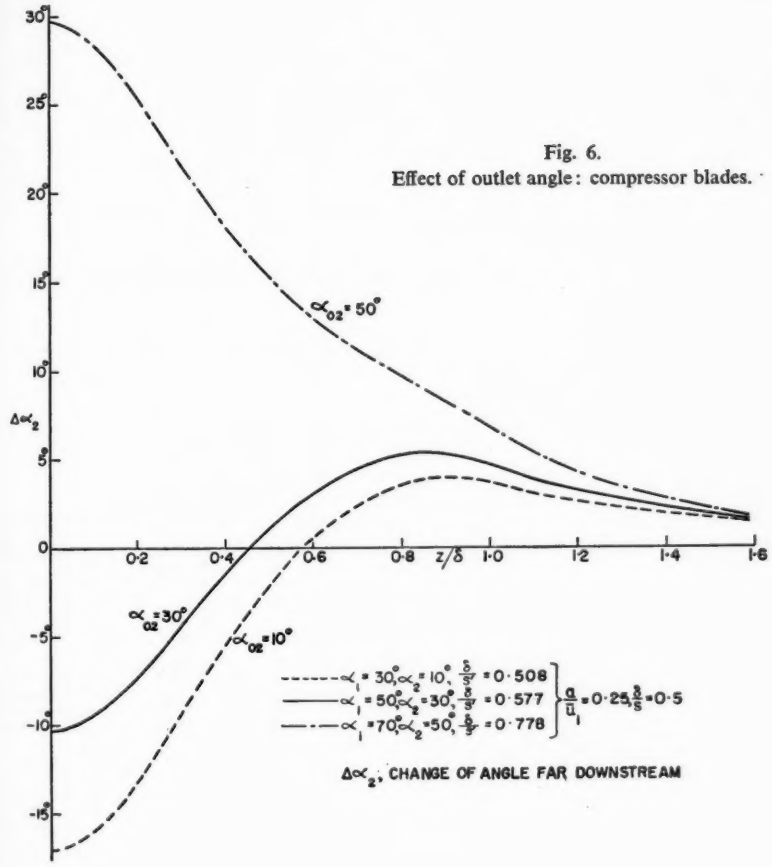

Fig. 6.
Effect of outlet angle: compressor blades.

Fig. 4 shows the effect of the magnitude of the velocity reduction in the wake. As might be expected from equation (35), the smaller is $a/\overline{u}_1$, *i.e.* the smaller the velocity variation in the wake, the less is the magnitude of the angle variations.

The effect of boundary layer thickness is shown in Fig. 5, in which curves for $\delta/s' = \frac{1}{2}$ and 1 are presented. As the δ/s' term enters only into the expression for t', change in δ/s' does not affect the spanwise displacement (the first term in equation (21)). The larger is δ/s', the smaller is the value of the angle change t' due to secondary flow. For the turbine with $\alpha_{02} = 60°$, the reduction of the secondary flow effect between $\delta/s' = \frac{1}{2}$ and $\delta/s' = 1$ is large enough to change the sign of $\Delta\alpha_2$ at small values of z/δ. The change of boundary layer thickness also has a large effect on the value of $\Delta\alpha_2$ for the compressor cascade shown.

Figure 6 shows the effect of varying the outlet angle of a compressor cascade at constant deflection. The conditions are similar to those in Fig. 3, except that the ratio of boundary layer thickness δ to blade spacing s is constant ($\delta/s = \frac{1}{2}$), so

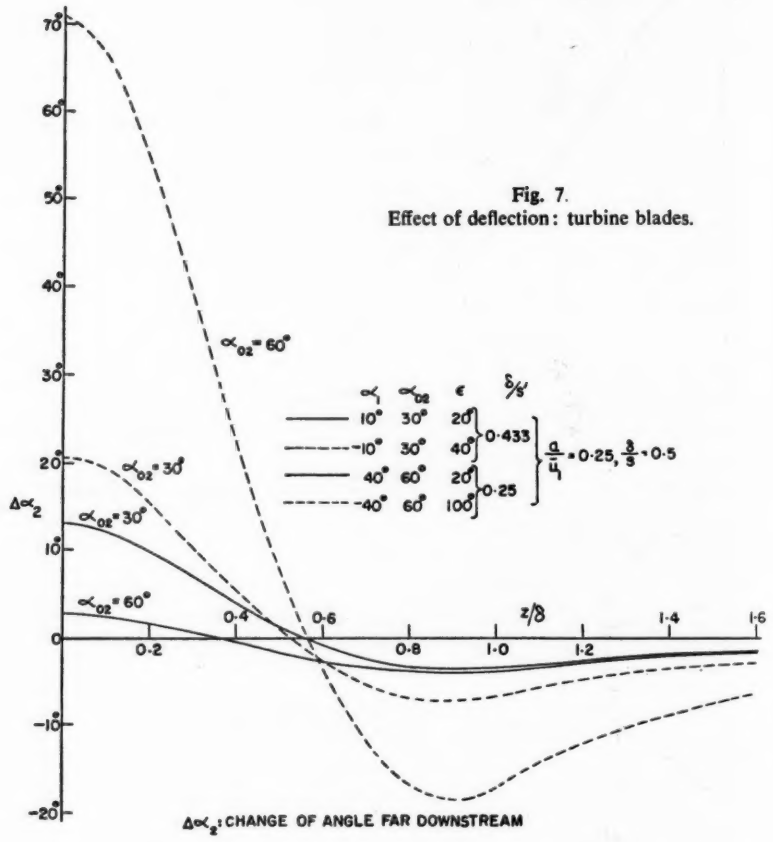

Fig. 7.
Effect of deflection: turbine blades.

that as α_{02} is varied from 10° to 50°, δ/s varies from 0·51 to 0·78 approximately. The increasingly large displacement effect with higher outlet angle is shown by the change in sign of $\Delta\alpha_2$ between the curves for $\alpha_{02}=30°$ and $\alpha_{02}=50°$. Comparison of Figs. 3 and 7 shows the large effect of deflection on the change in angle due to secondary flow. In Fig. 7 the large values for $\alpha_{02}=60°$ and $\epsilon=100°$ are clearly beyond the limits of the analysis.

In the curves in Figs. 2-7 the actuator plane is located at the trailing edge of the blades. This has been done to simplify the analysis. The modification to equation (21) necessary to allow approximately for other locations is given in the Appendix and curves showing the approximate effect of locating the actuator plane at the mid-chord position are given in Figs. 13-15. Moving the actuator plane forward from the trailing edge reduces the displacement effect, but does not alter the general inferences which have been drawn from the numerical results shown in Figs. 2-7.

2.8. Downstream Velocity Profile

The axial velocity u_2 far downstream may either be obtained from equation (22) or from equation (18). In some cases when the span is large compared to the thickness δ of the non-uniform region, $\bar{u}_2=\bar{u}_1$, which gives

$$u_2=u_1+2u'=u_1\left(1-\frac{2(t''-t')}{t}\right). \quad . \quad . \quad . \quad (37)$$

With the approximations made in deriving equation (35),

$$\frac{2(t''-t')}{t}=\left(\frac{\cos^2\bar{\alpha}_{02}}{\cos^2\alpha_1}-1\right)(m+1)\frac{a}{\bar{u}_1}\left(1+\cos\frac{\pi z}{\delta}\right)+$$

$$+\frac{32(\bar{\alpha}_{02}-\alpha_1)\sin\bar{\alpha}_{02}}{(2+\tan^2\bar{\alpha}_{02})\cos\alpha_1}\frac{a}{\bar{u}_1}\left[1+\frac{a}{\bar{u}_1}\left(1+\cos\frac{\pi z}{\delta}\right)\right]\left[\frac{\cos(\pi z/\delta)+e^{-\pi\delta/s'}\cosh(\pi z/s')}{\pi^2[1+(\delta/s')^2]}\right]$$

$$. \quad . \quad . \quad . \quad . \quad . \quad (38)$$

The resulting variation of u_2 is the same as that for constant α_{02}, equation (15) modified by an amount which is approximately proportional to $2mt'/t$, *i.e.* the third term on the right hand side of equation (22). Since $2m/t=2t/(2+t^2)$ this term will be zero for $\bar{\alpha}_{02}=0$ and 90°, and reaches a maximum of $1/\sqrt{2}$ at $\tan\bar{\alpha}_{02}=\sqrt{2}$. So that, over a range of values of t, u_2 will not be a strong function of t'. At the edge of the boundary layer $z=\delta$, $t''-t'$ will have the same sign as t', *i.e.* positive for a compressor and negative for a turbine. Hence, at $z=\delta$, u_2 will be less than $\bar{u}_2$ for a compressor cascade and greater for a turbine.

At the centre of the wake, $z=0$, if the value of t' is small, $t''-t'$ will be positive for a compressor and negative for a turbine. Hence, at $z=0$, u_2 will tend to be less than u_1 for a compressor and greater for a turbine. This conclusion remains approximately true provided that

$$\frac{1}{8}\sec^2\alpha_{02}\left(\frac{\cos^2\alpha_{02}}{\cos^2\alpha_1}-1\right)\frac{\cos\alpha_1}{(\alpha_1-\alpha_{02})\sin\bar{\alpha}_{02}}>\frac{(1+2a/\bar{u}_1)(1+e^{-\pi\delta/s'})}{\pi^2[1+(\delta/s')^2]} \quad . \quad (39)$$

If this does not hold, u_2 will tend to be greater than u_1 at $z=0$ for a compressor and less for a turbine.

Velocity profiles based on the assumption that $\bar{u}_2=\bar{u}_1$ are shown in Figs. 2 and 3. These profiles follow the general conclusions already given. As shown in the Appendix and in Figs. 13-15, the results are somewhat modified by any movement of the actuator disc from the trailing edge.

3. Experimental Work

3.1. Experimental Conditions

The results of two sets of experiments from somewhat similar cascades are available for comparison with the theory. In both experiments a stream with an artificially produced velocity profile symmetrical about the mid-span position was

allowed to pass through the cascade, and measurements of velocity and angle were made at distances far enough downstream to be equivalent to the downstream infinity location.* The first set of experiments described were made by W. D. Armstrong[6] and the second by E. A. Pinsley[7].

In each set of experiments, only small deflections were used and the blades were arranged as a cascade of turbine blades, so that there was a pressure drop through the cascade. In this way it was hoped to minimise losses. Three widely different outlet angles were used in each set of experiments and measurements of the cascade performance with a uniform inlet velocity were made in each case to establish the two-dimensional properties of the cascade.

3.2. Armstrong's Experiments

In these tests,† a cascade was set up in the working section (5 in. × 10 in.) of a pressure tunnel, supplied with air from a 1½ h.p. fan. The major dimensions were:—blade chord 0·90 in., pitch 1·08 in. and blade span 10·00 in. The blades, of which seven to nine were used, were constructed on a 33° circular arc camber line using the profile shape given in Fig. 8. At the ends of the blades the cascade walls were continued downstream for several chords. Boundary layer control was applied to the tunnel walls lying parallel to the blade span. This enabled the main streamlines in the neighbourhood of the wall to be slightly re-orientated and thereby ensured a uniform flow onto all the blades.

The upstream velocity profile was artificially modified by producing a "wake" upstream of the mid-span position, this wake being shed from a perforated plate 12 in. long which divided the tunnel into two passages, each 5 in. square. The plate was at least 15 in. upstream of the centre point of the cascade.

In all experiments, measurements were made of the inlet angle α_1, which was uniform, and the velocity one chord upstream and the velocity and angles one chord downstream. The measured angles and velocity profiles are given in Figs. 10-12. The outlet angles presented are those measured one chord downstream at a point midway between two blades, *i.e.* the maximum and not the mean.

3.3. Pinsley's Experiments

A similar set of experiments was done earlier‡ by Pinsley[7]. The cascade tunnel and experimental techniques were very similar, although in this case the blades had a lower camber and there were no walls downstream of the cascade. The dimensions were:—chord 0·80 in., pitch 0·80 in., parabolic camber 22·6° and blade span 10·00 in. Fig. 9 shows the blade arrangements used, while Figs. 13-15 give details of the incident velocity profiles, the outlet velocity profiles and

*As may be seen from examining equations (A5) and (A6) in the Appendix and the details of the configurations tested, this condition is practically reached at a distance of one chord downstream.

†In the Engineering Laboratory, Cambridge University.

‡In the Gas Turbine Laboratory, Massachusetts Institute of Technology, U.S.A.

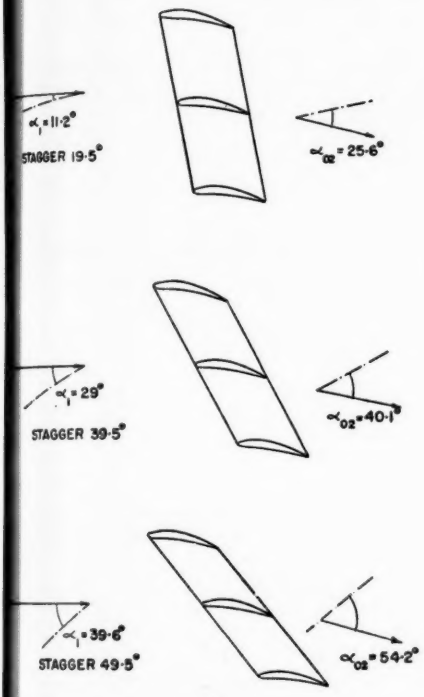

Fig. 8.

Arrangement of Cambridge cascades (*Armstrong*).

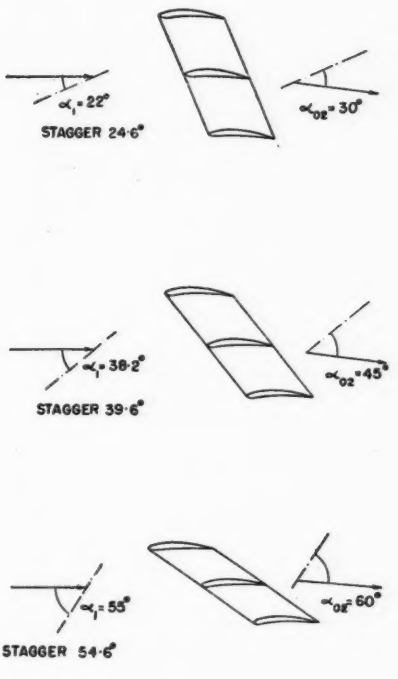

Fig. 9.

Arrangement of M.I.T. cascades (*Pinsley*).

Base Aerofoil

ion	0	2·5	5·0	10·0	20	40	60	80	100
hickness	0	2·27	3·08	4·02	4·83	4·89	4·09	2·75	0

(per cent chord)

Leading edge radius = 0·12 t, $t/c = 0{\cdot}10$,
Trailing edge radius = 0·12 t.

33° circular arc camber line.

Chord (c)	0·80 in.
Maximum camber	0·0482c
Distance from leading edge to point of maximum camber	0·4c
Maximum thickness	0·09c

the values of the velocity V in the $Y-$direction. The last were taken $1\frac{1}{4}$ chords downstream from the trailing edges, but the axial velocity measurements were made $2\frac{1}{2}$ chords downstream. The incident profiles were measured about 8 in. upstream of the cascade.

4. Comparison of Theory and Experiment

4.1. Armstrong's Experiments

Figure 10 shows the results of tests with a cascade with a nominal outlet angle of 25·5°. The upper curve shows the inlet velocity profile U_1. A cosine curve with the relation of equation (23) was fitted. In the calculation of the variation of velocity and angle downstream the actuator plane was located half a

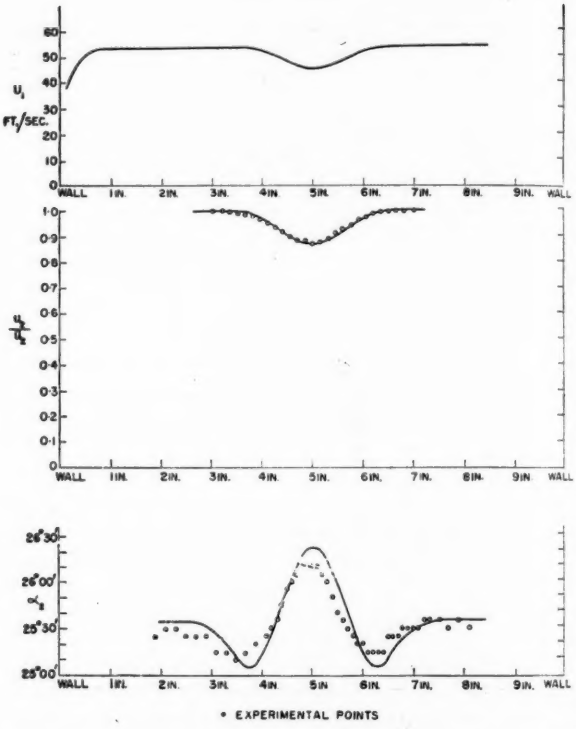

Fig. 10

Cambridge experiments. $\alpha_1 = 11{\cdot}2°$, Reynolds number $= 2{\cdot}72 \times 10^4$.

blade width upstream of the trailing edge. No pressure plots were made on the blades, so that the exact location of the centre of pressure is not known. This appeared, however, to be a reasonable position and the theoretical results with the plane located at the trailing edge give too much emphasis to the displacement effect. Consequently equations (A 12) and (A 14) in the Appendix were used to determine the outlet angle and downstream velocity profile. Equation (A 12) had to be slightly modified since, due to the difficulty of interpreting angle measurements in the wakes behind the blades, the angles measured were the maximum rather than the mean. The value of t' used in equation (A 12) was therefore determined from equation (30*a*) and not equation (30), but in calculating u_2 from equation (A 14) the mean value of t' was substituted.

The comparison between theory and experiment shown in Fig. 10 is good, and Fig. 11, for the cascade with a nominal outlet angle of 40°, shows similar satisfactory agreement. In Fig. 12, with an outlet angle of 54°, the agreement is still possibly satisfactory but better agreement could probably be obtained by placing the actuator plane slightly farther forward. Comparison of Figs. 10, 11 and 12 confirms the general prediction of the theory and shows that quite different variations of outlet angle α_2 and apparent deflection $(\alpha_2 - \alpha_1)$ are obtained in the three configurations.

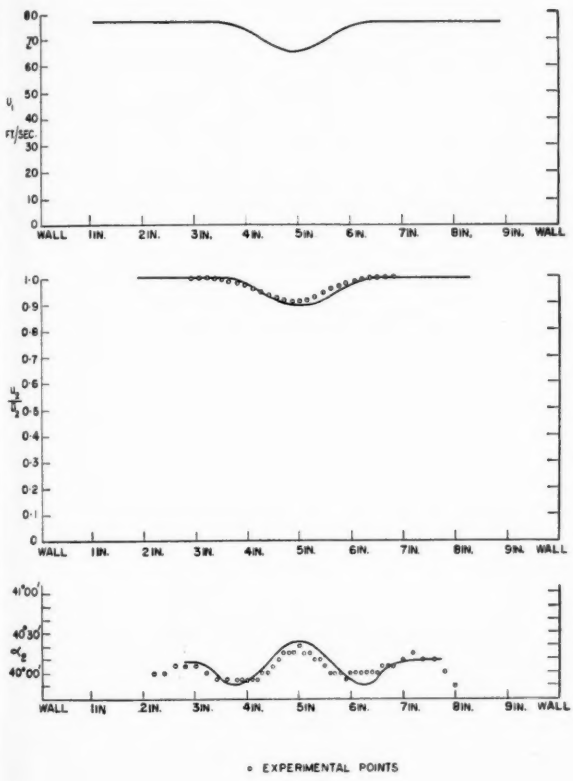

Fig. 11.

Cambridge experiments $\alpha_1 = 29°$, Reynolds number $= 3{\cdot}90 \times 10^4$.

4.2. Pinsley's Experiments

Figure 13 shows the results of tests with a nominal outlet angle of 30° and Figs. 14 and 15 the results with outlet angles of 45° and 60° respectively. The inlet velocity profiles used in these experiments gave larger velocity gradients and therefore inlet vorticity. The deflections were smaller, being of the order of 8°, 6·8° and 5° respectively compared with the values of 14·4°, 11° and 14·6° used in Armstrong's experiments. In view of this difference and its likely effect on the centre of pressure, theoretical calculations have been made with the actuator plane at the mid-chord position (full lines) and at the trailing edge (dashed lines). The value of δ has been rounded off at 2·0 in. and, while it is clear that this gives theoretical inlet velocity profiles slightly larger than the measured ones, the measuring station was so far upstream (about 8 in.) that some increase in thickness of this upstream wake is to be expected between the measuring point and the leading edge. The maximum values of V, the velocity in a plane of constant z in the $Y-$ direction (Fig. 1), *i.e.* normal to the nominal direction of flow, have been compared with the values reported by Pinsley. To calculate V the maximum value of $\Delta\alpha_2$

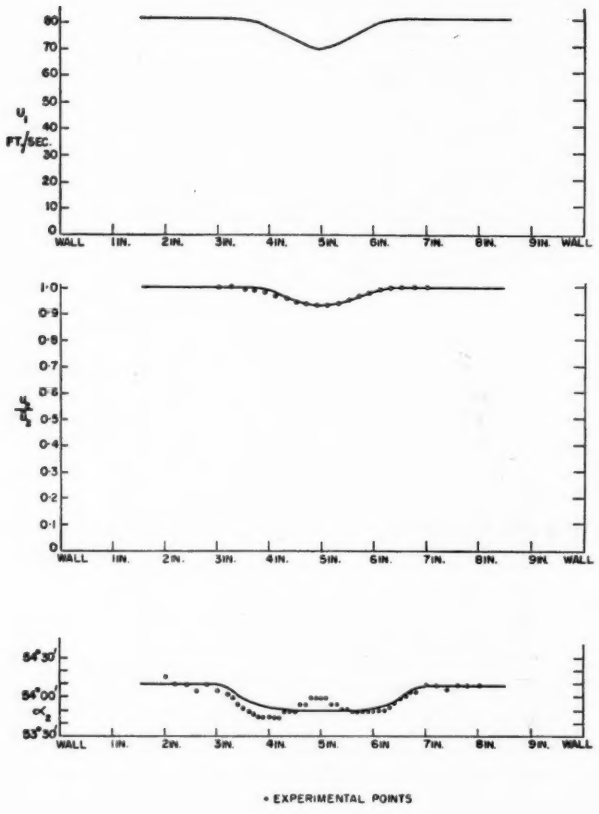

Fig. 12.

Cambridge experiments. $\alpha_1 = 39{\cdot}6°$, Reynolds number $= 4{\cdot}15 \times 10^4$

was used, together with Pinsley's measured velocity. These values of V differ from $\Delta\alpha_2$ only by a multiplying factor which is approximately constant. The agreement between theory and experiment shown in Fig. 13 is not as good as that shown in Fig. 10, although the character of the variation of outlet angle is very similar. The outlet angle is larger at the mid-span position than the value given by the full-line curve which is calculated with the actuator plane at the mid-chord position. Presumably if the actuator plane were placed at the leading edge better agreement would be obtained. The minimum of the experimental values occurs at $z = 3$in., whereas for both theoretical curves it is at about $z = 3\frac{1}{2}$ in. The experimental downstream velocity profile is also shallower than the theoretical one. This may be due partly to the effect of friction and mixing in the 10·5 in. between upstream and downstream measuring positions, which is ignored in the theoretical treatment.

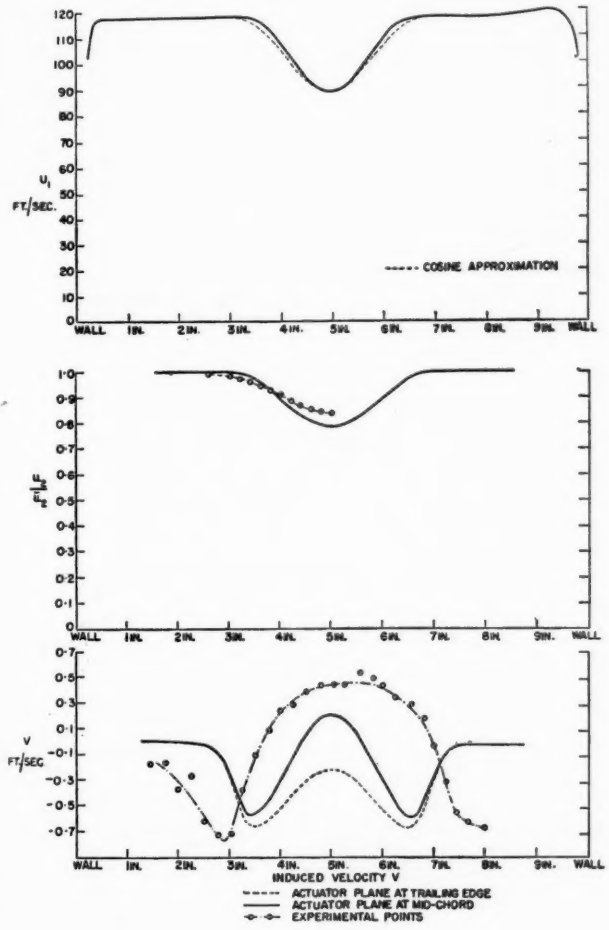

Fig. 13.

M.I.T. experiments. $\alpha_1 = 22°$, $\alpha_{02} = 30°$.

Similar differences between theory and experiment are noted in Fig. 14, $\bar{\alpha}_{02} \simeq 45°$, although the agreement for the value of V_{max} at the mid-span position is good when the actuator plane is placed at the mid-chord position.

The results shown in Fig. 15, $\bar{\alpha}_{02} \simeq 60°$, show a better correlation between theory and experiment with the actuator plane at the trailing edge. This is possibly justified, since the incidence decreases from $-10{\cdot}9°$ at $\bar{\alpha}_{02} \simeq 30°$ to $-13{\cdot}9°$ at $\bar{\alpha}_{02} \simeq 60°$.

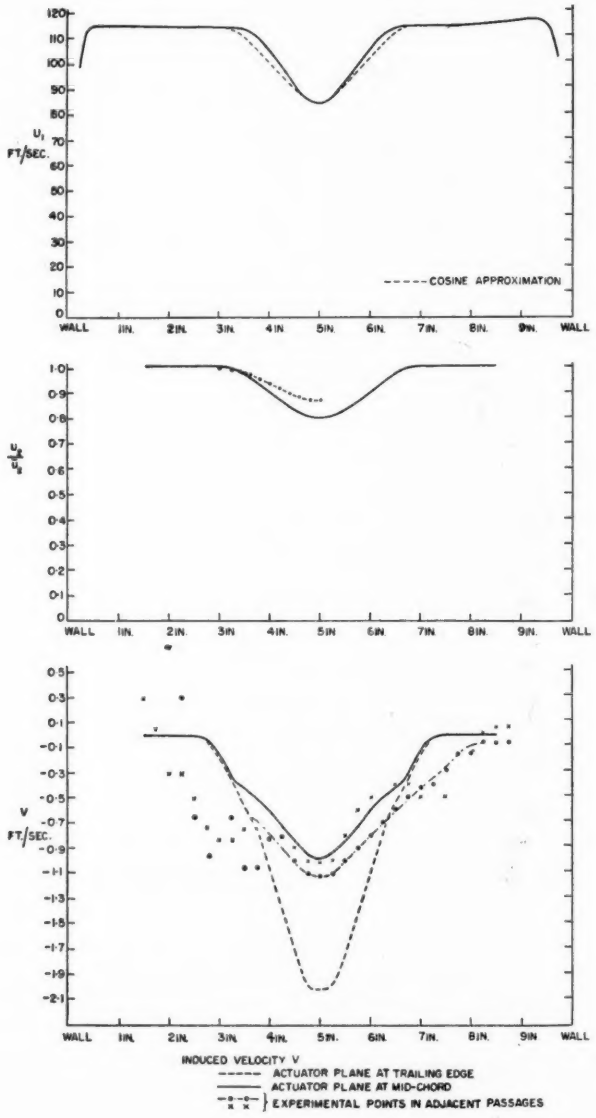
U, FT/SEC.
COSINE APPROXIMATION
WALL 1IN. 2IN. 3IN. 4IN. 5IN. 6IN. 7IN. 8IN. 9IN. WALL
V FT/SEC.
INDUCED VELOCITY V
ACTUATOR PLANE AT TRAILING EDGE
ACTUATOR PLANE AT MID-CHORD
EXPERIMENTAL POINTS IN ADJACENT PASSAGES

Fig. 14.

M.I.T. experiments. $\alpha_1 = 38{\cdot}2°$, $\alpha_{02} = 45°$.

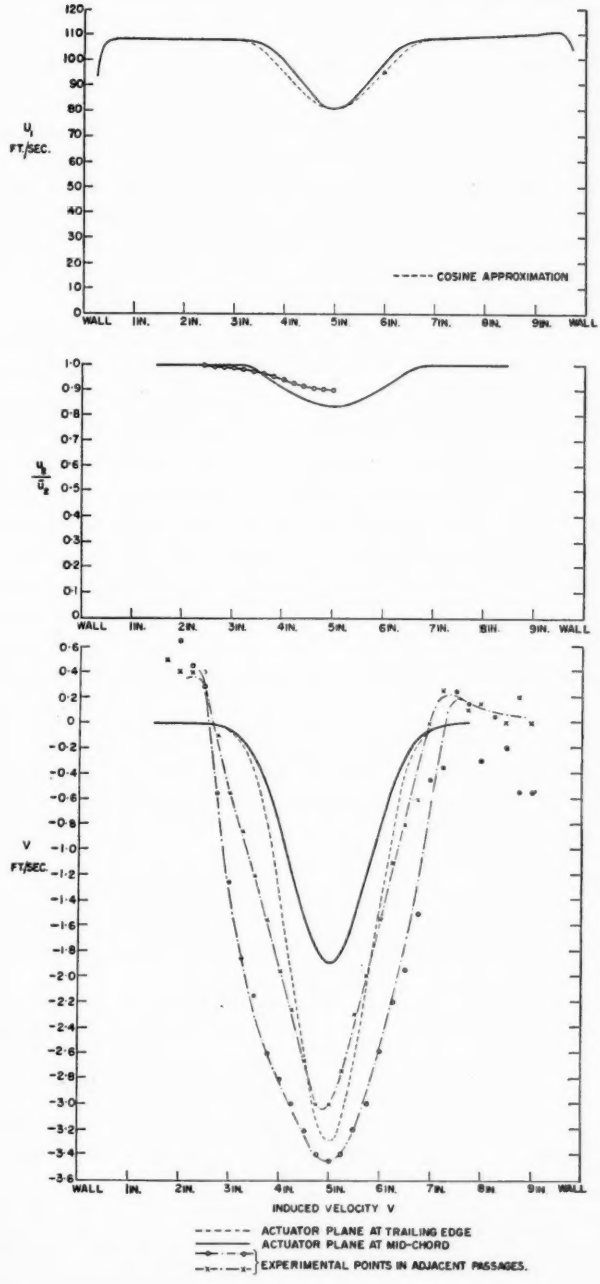

Fig. 15.
M.I.T. experiments. $\alpha_1 = 55°$, $\alpha_{02} = 60°$.

5. Conclusions

The theory predicts a variation of types of distribution of angle downstream which are, for instance, markedly different for differing cascade staggers. These predictions are largely confirmed by the experimental results. The correlation between theory and experiment is best when the vorticity initially present in the approaching flow is small, as in Armstrong's experiments. Reasonable correlation is achieved for Pinsley's results. The position chosen for the actuator plane is important and the correlation between theory and experiment reflects any uncertainty in the location of this position.

At small nominal outlet angles the secondary flow in the blade passages largely determines the variation in angle downstream. At large outlet angles the secondary flow effects are masked by the large spanwise displacements of the flow; this is accompanied by a marked smoothing of the axial velocity profile.

Other effects being equal, a thicker region of non-uniform flow reduces the initial vorticity and therefore the departure of downstream flow angles from the nominal values. The same applies to the effect of reducing the initial velocity variations. The larger the deflection is, the larger is the secondary flow in the blade passages and its influence on the downstream flow.

Although the analysis ignores losses and is only valid for initially small non-uniformities in velocity, it should be of some assistance in the interpretation of the behaviour of the boundary layers on the walls of cascades or compressors.

Acknowledgments

Acknowledgment is due to the Chief Scientist, Ministry of Supply, for permission to publish the results obtained from experiments in the Engineering Department, Cambridge University.

References

1. Marble, F. E. The Flow of a Perfect Fluid through an Axial Turbomachine with Prescribed Blade Loading. *Journal of the Aeronautical Sciences*, Vol. 15, p. 473, August 1948.
2. Bragg, S. L. and Hawthorne, W. R. Some Exact Solutions of the Flow through Annular Cascade Actuator Discs. *Journal of the Aeronautical Sciences*, Vol. 17, p. 243, April 1950.
3. Squire, H. B. and Winter, K. G. The Secondary Flow in a Cascade of Aerofoils in a Non-Uniform Stream. *Journal of the Aeronautical Sciences*, Vol. 18, p. 271, April 1951.
4. Hawthorne, W. R. and Armstrong, W. D. Rotational Flow Through Cascades. Part II. The Circulation about the Cascade. *Quarterly Journal of Mechanics and Applied Mathematics*. Vol. VIII, Part 3, p. 280, September 1955.
5. Ruden, F. Investigation of Single Stage Axial Flow Fans. N.A.C.A. T.M. 1062, 1944.
6. Armstrong, W. D. The Non-Uniform Flow of Air through Cascades of Blades. Cambridge University Ph.D. Thesis, 1954.
7. Pinsley, E. A. An Investigation of Secondary Cascade Flows. Massachusetts Institute of Technology M.Sc. Thesis, 1950.

Appendix

Effect of Actuator Plane Location

When the actuator plane is not located at the trailing edge it becomes necessary to estimate the value of the axial velocity u_e at the trailing edge, since the theory assumes that the angle α_{02} is the value at the trailing edge and hence $v_2 = u_e \tan \alpha_{02}$. From equation (3), the vorticity downstream of the actuator plane is given by

$$\eta = \frac{\partial u}{\partial z} - \frac{\partial w}{\partial x} = \frac{\partial u_2}{\partial z} + \frac{\partial u_d}{\partial z} - \frac{\partial w}{\partial x}, \quad . \quad . \quad . \quad . \quad . \quad \text{(A 1)}$$

where $u = u_2 + u_d$.

Since η does not vary with x within the limits of the assumption made in the main text, $\eta = \partial u_2 / \partial z$ and hence

$$\frac{\partial u_d}{\partial z} = \frac{\partial w}{\partial x} \quad . \quad . \quad . \quad . \quad . \quad . \quad . \quad \text{(A 2)}$$

Also, by continuity,
$$\frac{\partial u_d}{\partial x} + \frac{\partial w}{\partial z} = 0. \quad . \quad . \quad . \quad . \quad . \quad \text{(A 3)}$$

Hence
$$\frac{\partial^2 u_d}{\partial x^2} + \frac{\partial^2 u_d}{\partial z^2} = 0$$

and
$$\frac{\partial^2 w}{\partial x^2} + \frac{\partial^2 w}{\partial z^2} = 0. \quad . \quad . \quad . \quad . \quad . \quad \text{(A 4)}$$

The boundary conditions are that $w = 0$ at $z = 0$ and on any other wall. However, taking into account that, as mentioned in the discussion after equation (13), the assumptions for η imply that u_0 and u_2 are constant outside the region in which u_1 varies with z, it seems reasonable to assume that at the edge of the boundary layer $\partial u_d / \partial z = 0$. With these conditions

$$u_d = \Sigma b_m \cos \frac{m\pi}{\delta} z \, e^{-\frac{m\pi x}{\delta}} \quad . \quad . \quad . \quad . \quad . \quad . \quad \text{(A 5)}$$

where $m = 1, 2, 3$ and so on.

Neglecting all terms in the series except that for $m = 1$, the velocity at the trailing edge becomes

$$u_e = u_2 - (u_2 - u_0) \exp(-\pi x_e / \delta), \quad . \quad . \quad . \quad . \quad \text{(A 6)}$$

where x_e is the distance from the actuator plane location to the trailing edge.

Hence
$$v_2 = u_e \tan \alpha_{02} = (t + t')(u_1 + u' + Ku'), \quad . \quad . \quad . \quad \text{(A 7)}$$

where
$$K = 1 - \exp(-\pi x_e / \delta).$$

Neglecting terms in t'^2, u'^2 and $u't'$,

$$v_2 \frac{dv_2}{dz} = \tfrac{1}{2} \frac{d}{dz}(u_1^2 t^2 + 2u_1^2 tt' + 2u_1 t^2 u') + K \frac{d}{dz}(u_1 t^2 u'). \quad . \quad . \quad \text{(A 8)}$$

The additional term in K needs to be included in equation (17), giving

$$\left[2+(1+K)\,t^2\right]\frac{du'}{dz} + (1+K)\frac{u't^2}{u_1}\frac{du_1}{dz} = \tan^2\alpha_1 \frac{du_1}{dz} - t^2\frac{du_1}{dz} - \frac{t}{u_1}\frac{d}{dz}(u_1^2 t'). \quad \text{(A 9)}$$

Similar rearrangement gives, for equation (19),

$$\frac{d}{dz}(u_1 t'') + m' t'' \frac{du_1}{dz} = -\frac{m'}{t}\left(\frac{1-K}{1+K}\right)(\tan^2\alpha_1 - t^2)\frac{du_1}{dz} + \left[m'\left(\frac{1-K}{1+K}\right)+1\right]\frac{du_1 t'}{dz} + \\ + \frac{2}{1+K}\frac{u_1 t'}{u_1^{m'}}\frac{du_1^{m'}}{dz}, \quad . \quad \text{(A 10)}$$

$$\text{where} \qquad m' = t^2(1+K)/[2+(1+K)\,t^2]. \quad . \quad . \quad . \quad . \quad \text{(A 11)}$$

Hence the solution for t'' similar to equation (20) and omitting the integral term which has been shown to be small is

$$t'' = -(1-K)\left\{\frac{1+t^2}{1+(1+K)\,t^2}\right\}\frac{t}{2}\left(\frac{\cos^2\bar{\alpha}_{02}}{\cos^2\alpha_1} - 1\right)\left[1 - \left(\frac{\bar{u}_1}{u_1}\right)^{m'+1}\right] + \frac{2(1+t^2)}{2+(1+K)\,t^2}\,t'. \\ . \quad . \quad . \quad . \quad \text{(A 12)}$$

Putting $u_e \tan\alpha_{02} = u_2 \tan\alpha_2$, we obtain an equation analogous to equation (18)

$$u't(1-K) = u_1(t' - t''). \quad . \quad . \quad . \quad . \quad . \quad \text{(A 13)}$$

From which, assuming $\bar{u}_1 = \bar{u}_2$,

$$\frac{u_2}{\bar{u}_2} = \frac{u_1}{\bar{u}_1}\left[1 - \frac{2(t'' - t')}{t(1-K)}\right]. \quad . \quad . \quad . \quad . \quad \text{(A 14)}$$

The Design of Intermediate Vertical Stiffeners on Web Plates Subjected to Shear

K. C. ROCKEY, Ph.D., M.Sc.(Eng.), A.M.I.C.E.

(Engineering Department, University College of Swansea)

SUMMARY: The correct design of intermediate vertical stiffeners on web plates subjected to shear becomes very important when the web plates are designed to operate at loads close to their buckling loads. This paper presents details of an extensive series of tests conducted on stiffened web plates subjected to shear. From the analysis of the results obtained from these tests, new empirical relationships between the flexural rigidity and spacing of the intermediate stiffeners and the buckling stress of the stiffened web plate have been obtained.

One interesting and important feature of these new relationships is that they define more clearly than hitherto the difference in the behaviour of single- and double-sided stiffeners.

1. Introduction

Plate girders are extensively used in one form or another in all types of civil and aeronautical construction and, because of the obvious necessity of obtaining a correct design procedure, many investigations have been made to examine the behaviour of plate girders when under load. As a result, much is now known about the various buckling phenomena associated with plate girders.

However, one very important problem, which has not attracted as much attention as others, is the determination of the relationships which exist between the size and spacing of intermediate vertical stiffeners and the shear buckling stress of the stiffened web plate. The existing experimental evidence, while inconclusive in itself, has shown that in practical structures the flexural rigidity of the intermediate stiffeners has to be much greater than that required by the theoretical analyses. This is not surprising when it is appreciated that, to obtain the theoretical solutions, it has been necessary to make certain simplifying assumptions which are not strictly correct when practical structures are considered.

This paper presents the results obtained from an experimental investigation made in an attempt to obtain the relationships between the size and spacing of intermediate vertical stiffeners and the buckling stress of the stiffened web plate when it is subjected to shear. Tests were made on more than two hundred different plate-stiffener combinations and from the analysis of the results it has been possible to derive new empirical relationships.

Received September 1955.

NOTATION

t thickness of web plate

t_u thickness of attached stiffener leg

b spacing of intermediate stiffeners or width of unstiffened web plate

b_c clear web plate distance between stiffeners

d_c clear depth of web plate

α_e effective aspect ratio

$=b/d_c$ for unstiffened web plates or web plates reinforced by single-sided stiffeners

$=b_c/d_c$ for web plates reinforced by double-sided stiffeners

D flexural rigidity of unit width of plate $=Et^3/\{12(1-\mu^2)\}$

E Young's modulus

μ Poisson's ratio

I moment of inertia of stiffener

EI flexural rigidity of stiffener

$$\gamma=\frac{EI}{Db}=\frac{\text{stiffener rigidity}}{\text{rigidity of strip of web plate equal in width to stiffener spacing}}$$

I_c moment of inertia of the combination of a single-sided stiffener plus strip of web plate equal to stiffener spacing, calculated about the centroid of the combination

γ_L limiting value of γ

T shear stress

T_{cr} critical shear stress $=KD/(d_c^2t)$

K critical shear stress coefficient

K_L limiting value of K

2. Background

2.1. Summary of Existing Theoretical Knowledge

Theoretical studies[1, 2, 3] have established that the buckling stress T_{cr} of plane unstiffened rectangular panels can be determined from equation (1), in which K is a coefficient, the value of which depends upon the superficial dimensions of the panel and the type of edge support.

$$T_{cr}=\frac{K\pi^2D}{d_c^2t} \quad . \quad . \quad . \quad . \quad . \quad . \quad (1)$$

As Fig. 1 shows, the value of the critical shear stress coefficient K increases with decreasing values of the aspect ratio b/d_c. This explains why intermediate vertical stiffeners provide such an effective method of increasing the buckling stress

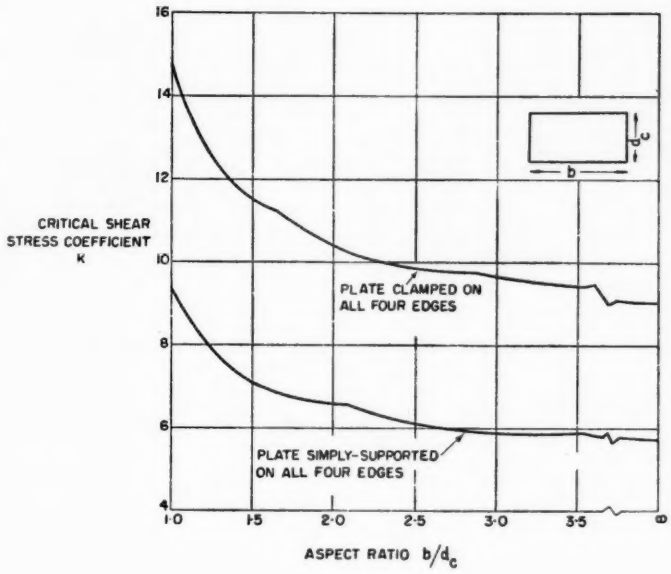

Fig. 1.

of rectangular panels. In view of the importance of obtaining the correct design of intermediate stiffeners, it is not surprising that a number of theoretical investigations have been made to determine the relationships between the size and spacing of intermediate stiffeners and the buckling stress of the stiffened web plate.

Schmieden[4], Seydel[5] and Wang[6] have obtained relationships between the size and spacing of relatively weak, but closely spaced, transverse stiffeners and the buckling stress of the stiffened web plate. The effect of such stiffeners may be considered as stiffening the plate in one direction, but not influencing the strength in the direction normal to the stiffeners and the problem reduces to a study of the buckling of an orthotropic plate. From the exact results obtained by Seydel, certain well known design formulae have been developed[7, 8].

In 1936, Timoshenko[1] and Way[9] obtained relationships between the non-dimensional parameter $\gamma (=EI/Db)$ and the shear stress coefficient K of simply-supported finite rectangular plates reinforced by one or two transverse stiffeners. They showed that if the transverse stiffeners were relatively flexible they would bend with the plate and not restrict the wave pattern, but that, by increasing the flexural rigidity of the stiffeners, a stage would be reached when they would remain straight, thus forming a nodal line. From their solution, Timoshenko and Way calculated the minimum flexural rigidity which stiffeners should possess if they are to remain straight and supply adjacent panels with a simple pin-joint support; the values they obtained are plotted in Fig. 2.

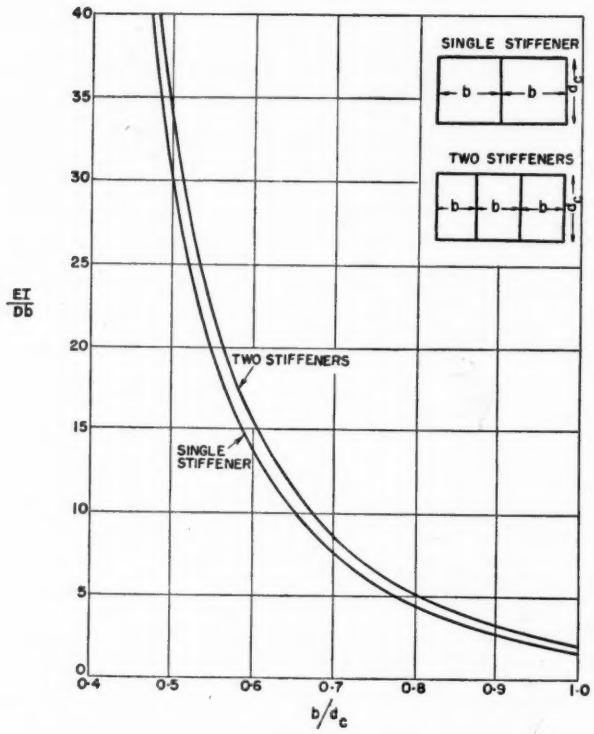

Fig. 2.

Timoshenko and Way's theoretical relationships for the condition that intermediate stiffeners supply a simple pin-edge support.

In 1949, Stein and Fralich[10] produced an excellent paper in which they made a thorough study of the behaviour of infinitely long, simply-supported plates reinforced by equally spaced transverse stiffeners. Now, theoretical work on plane rectangular panels has shown that buckling loads above the true minimum value will be obtained if an incorrect, that is ill-chosen or inadequate, expression is used to define the deflected form of the plate. In their paper, Stein and Fralich made a detailed study of this problem to ascertain which deflection expression would provide the correct, that is minimum, buckling load. The K/γ relationship they obtained, for one of the aspect ratios considered, is plotted in Fig. 3, and it will be noted that points of discontinuity occur on the K/γ curves. These points of discontinuity denote where changes in the governing buckle pattern occur. This work of Stein and Fralich showed that the earlier theoretical work of Timoshenko and Way overestimated the value of the critical shear stress coefficient K obtained with stiffeners of intermediate stiffness, and underestimated the value of K obtained with fairly rigid stiffeners.

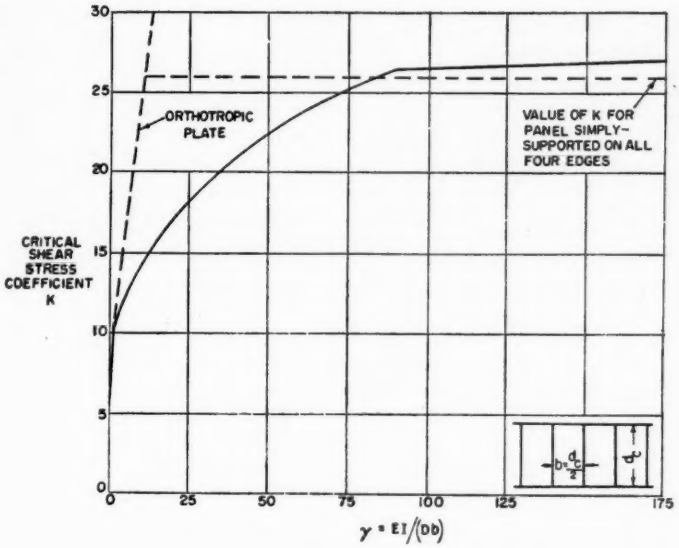

Fig. 3.

The theoretical K/γ relationships derived by Stein and Fralich for infinitely long plates simply-supported at the edges and reinforced by stiffeners $0{\cdot}5d_c$ apart.

2.2. Summary of Existing Experimental Investigations

Throughout the past century, a great number of tests have been carried out on plate girders in attempts to obtain a better understanding of the behaviour of the web plates when under load. However, on examining the technical literature, it will be found that very few of the investigations were primarily concerned with the influence of stiffener dimensions upon the stability of the web plate.

One notable exception was the investigation of Moore[11] who, in 1942, reported on his extensive tests on two aluminium alloy girders. Unfortunately, Moore failed to obtain values of the experimental buckling loads and had to resort to determining test loads corresponding to an arbitrary constant value of web or stiffener deflection. One great disadvantage of this procedure, and one which Moore himself recognised, was that the use, as a measure of the effectiveness of stiffeners, of a constant value of web or stiffener deflection at a load corresponding to the theoretical load for panels with all edges 50 per cent. fixed, will of necessity involve different degrees of buckling for panels of varying size and different aspect ratios.

Moore, working on these lines, produced the empirical design formulae

$$\gamma = \frac{14}{(b/d_c)^3} \quad . \quad . \quad . \quad . \quad . \quad . \quad (2)$$

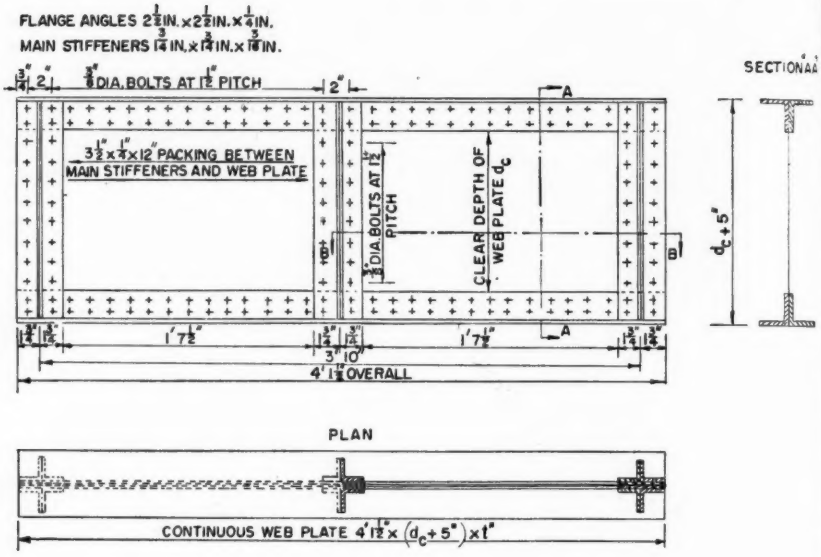

Fig. 4.
Design details of the BTG/– series of test girders.

Now, although a designer who might use this formula would not know the buckling load of the plate-stiffener combination, he would know that at loads corresponding to the theoretical buckling loads for panels with partially (50 per cent.) clamped edges, the web plate and stiffener deflections would be small.

A year later, Scott and Weber[12] reported on tests on stiffened shear and compression panels. Like Moore, they experienced difficulty in obtaining experimental values of the buckling load. As a result of their tests they found that an effective stiffener required a flexural rigidity greater than that predicted by Timoshenko and Way.

In the United Kingdom, Sparkes[13] has conducted an extensive programme of research on plate girders and, in the course of his tests, he also found that intermediate stiffeners having a flexural rigidity equal to twice Timoshenko's theoretical value failed to divide the web plate into separate panels.

From the foregoing it will be noted that, although the previous investigations failed to provide experimental relationships between the parameter γ and the shear stress coefficient K, they did establish the fact that intermediate stiffeners designed in accordance with Timoshenko's theoretical relationships would be unsatisfactory, in that they would not provide the necessary support to the plate.

3. The Experimental Investigation

3.1. Aim of Investigation

The testing programme was planned to provide information on the following points: —

(*i*) The relationships between the critical shear stress coefficient K and the non-dimensional parameter γ for varying values of the ratio (stiffener spacing)/(clear depth of web plate).

(*ii*) The difference in the behaviour of single- and double-sided stiffeners, which also involved an examination of the influence of the width of the attached leg.

3.2. The Design of the Plate Girders and Shear Panels

The plate girders and shear panels were designed to conform as nearly as possible with the following requirements: —

(*a*) that the web plates be subjected to pure shear,

(*b*) that the buckling stresses of the stiffened web plates be well below the 0·1 per cent. proof stress of the sheet material,

(*c*) that failure of the girder should be due to failure of the web plate.

Requirements (*a*) and (*c*) were satisfied by using relatively heavy flange members which ensured that the applied bending stresses were small. By constructing the girders and shear panels of H 10 WP[14] high strength aluminium alloy and using web plates having high d_c/t ratios, requirement (*b*) was satisfied.

The design details of the BTG/- series of test girders are shown in Fig. 4, while details of the shear panels are clear from Fig. 5, which shows a specimen in the testing machine.

3.3. The Testing Equipment

The plate girders and shear panels were tested in an Amsler testing machine, the general features of which can be seen in Fig. 6, which shows a girder in position. The girder was supported on roller bearings and loaded through a similar roller bearing, this ensuring that the flange members could expand or contract during a test.

The lateral deflections of the web plate were measured with accurate dial gauges graduated in units of either 0·0005 in. or 0·0001 in. To ensure that the dial gauges only recorded the lateral deflections of the web plate, they were attached to a special frame which was secured to the girder by three adjustable screws situated in the plane of the web plate. (For details, *see* Fig. 6.) This arrangement ensured that there would be no relative movement of the dial gauges with respect to the central plane of the girder, should the girder twist under load. During some of the tests, additional dial gauges which were not attached to the special frames were used. Unfortunately, the results obtained with these gauges were often

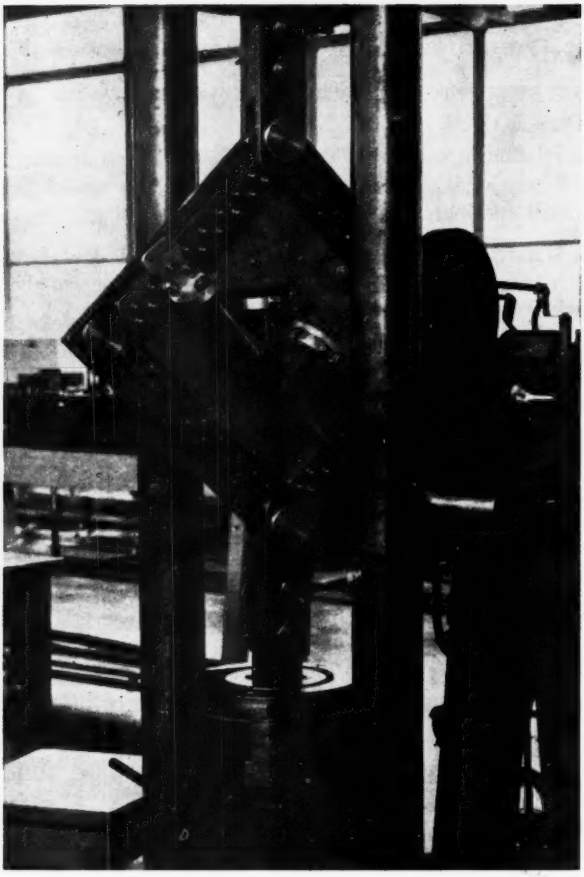

Fig. 5.
Shear panel in the testing machine.

unsatisfactory, since the gauges had recorded some overall movement of the girder in addition to the lateral deflection.

During certain tests, contour plots were taken of the buckled shape of the web plate. To obtain these contour plots, a series of gauge bars were held parallel to the central plane of the girder and the position of the web plate relative to these bars was determined before and during the test, using a dial gauge graduated in units of 0·0005 in.

In addition, electrical resistance strain gauges were used to record the strains in the web plate and stiffeners. The gauges used were British Thermostat Self-Adhesive gauges having an effective gauge length of $\frac{1}{2}$ in.

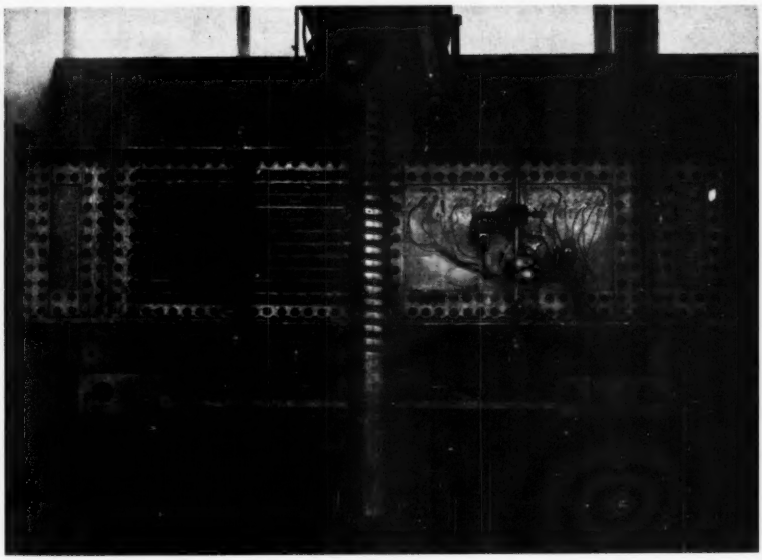

Fig. 6.
A test girder shown in position in the testing machine.

3.4. The Tests

The testing programme involved tests on 18 plate girders and 12 shear panels. Six of the test girders were of riveted construction, and 12, referred to as the BTG/- series of test girders, were of bolted construction. No details are given of the tests on the riveted test girders, since large lateral deformations were formed in the web plates during construction and consequently the buckling phenomenon was not well defined. These tests made it clear that little progress would be made towards obtaining the K/γ relationships unless the web plates of future girders were flat, thus ensuring that a well defined buckling phenomenon would be obtained. It was for this reason that the BTG/- series of test girders were of bolted construction.

The first girder of the BTG/- series was very carefully constructed and two tests were made on it. The first test, done before intermediate stiffeners were fitted, was to determine whether, in accordance with Ref. 15, the web plate was rigidly clamped at its edges. The web plate was flat and, as a result, extremely good plots of load against lateral deflection and load against strain were obtained. For the second test on girder BTG/1, the web plate was divided into three equal panels by employing two sets of very stiff double-sided stiffeners. During the initial stages of this test, electrical resistance strain gauge and dial gauge readings were taken at frequent intervals until it was apparent that the panels had buckled. Once again a very well defined buckling phenomenon was obtained, as shown in Fig. 7.

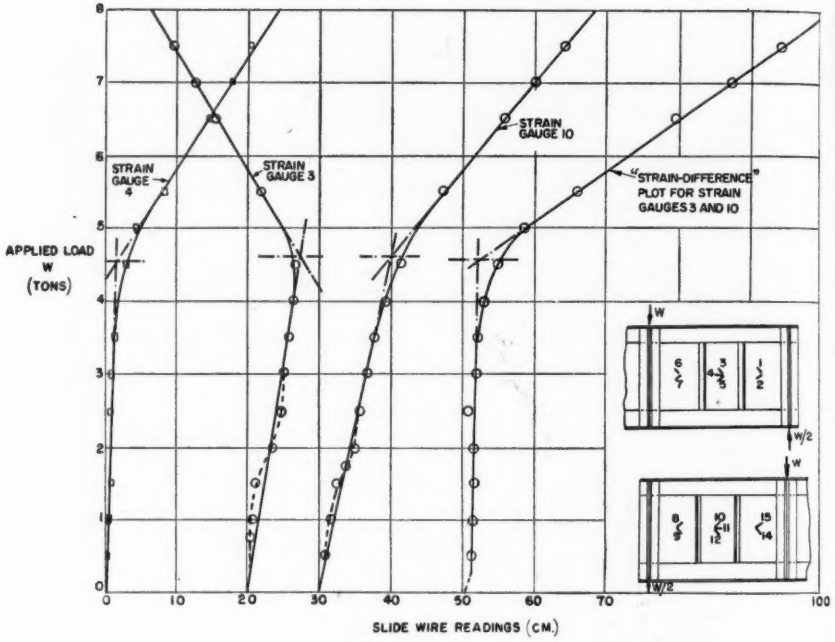

Fig. 7.
Load/strain plots obtained from test BTG/1/2.

Girder BTG/2 was fitted with a weaker set of double-sided stiffeners and a test similar to the second test on girder BTG/1 was done on it. Once again a well defined buckling load was obtained. These tests therefore showed that the degree of planeness of the web plate obtained with the method of construction was satisfactory.

The next step was to determine whether good results could be obtained when single-sided stiffeners were used, and tests involving single-sided stiffeners were conducted on girder BTG/3. At first a set of relatively flexible single-sided stiffeners were fitted and the girder slowly loaded, while dial gauge and strain gauge readings were taken at frequent intervals. When it was evident that the web plate had buckled the girder was unloaded. The resulting zero load readings were then compared with the initial zero load readings to determine whether the web plate had, in fact, returned to its original position. This was found to be the case. The intermediate stiffeners were then removed and, after fitting a slightly stronger set of intermediate stiffeners, the loading and unloading procedure was repeated. From the experimental readings obtained from both tests, well defined buckling loads were obtained.

The tests had clearly established the fact that, provided that the web plate was initially plane, well defined buckling loads could be obtained with both single- and doubled-sided stiffeners.

Since it was intended that many tests should be done on each of the remaining girders, it was considered that a check on the influence of repeated buckling upon the behaviour of a panel would be of value. A repeated loading test was, therefore, conducted on an unstiffened shear panel. (For details of the loading frame, *see* Fig. 5.)

During this test, the panel was repeatedly loaded up to a load corresponding to twice the initial buckling load of the panel, the buckling load of the panel being determined during certain of these operations. It was found, as was expected, that the buckling load was unaffected by the loading operations. This was of interest since, during certain shear tests on curved panels[16], it had been found that repeated buckling had lowered the buckling stress of the panels.

In all the subsequent tests on the test girders and shear panels the following procedure was adopted. The weakest set of intermediate stiffeners to be used on the given girder would be placed in position and the zero load readings taken. The girder was then gradually loaded, dial gauge readings, and in certain tests strain gauge readings, being taken at frequent load intervals. When it was apparent from these readings that the web plate had been loaded up to at least 30 per cent. beyond the buckling load, the girder was unloaded. The resulting dial and strain gauge readings were then compared with the initial zero load readings. If the dial gauge readings returned to within a few divisions of the initial readings (each division was 0·0001 in.), it was considered that the web plate had not been permanently deformed during the test and that a further test could be done on it. The intermediate stiffeners were then removed, another set of stiffeners fitted to the web plate, and the procedure repeated.

4. The Analysis of the Experimental Results

Altogether 220 different plate-stiffener combinations were tested, of which 125 involved single-sided stiffeners. The K/γ relationships obtained from most of the tests followed a well-defined pattern. However, there were a few cases with widely spaced stiffeners when, because of excessive scatter of the results, the relationships were not so apparent. With regard to the scatter of experimental results, it will be appreciated that if a few freak or poor results are obtained, then a much larger number of normal results are required before the correct or real relationships become apparent.

An examination of the results obtained from two sets of tests, one involving double-sided stiffeners, the other single-sided stiffeners, will illustrate the nature of the K/γ relationships.

Twenty-three tests involving single-sided stiffeners were done on three girders, BTG/7, 8 and 11, the stiffener spacing being $4\frac{7}{8}$ in. and clear depth of web plate 12 in. The experimental results have been plotted in Fig. 8; the value of the critical shear stress coefficient K increases with increasing values of γ, until a certain limiting value γ_L, which in this case is 124, is reached, while for values of γ greater than 124, the value of K remains approximately constant at the mean value of 43.

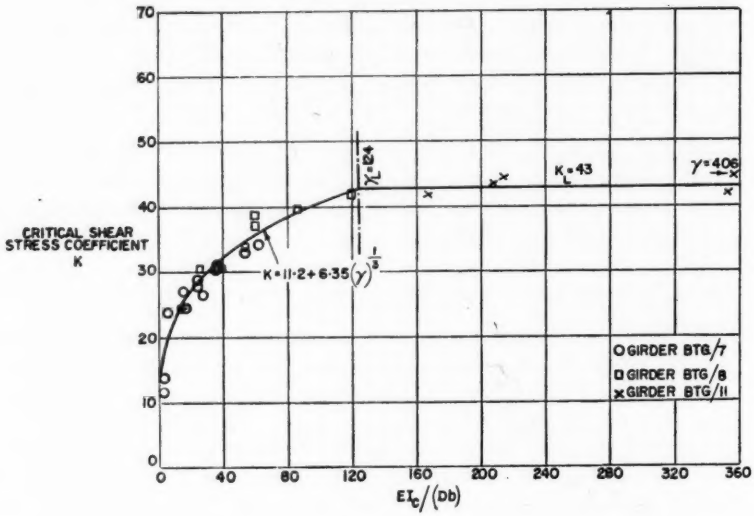

Fig. 8.

Results obtained when employing single-sided stiffeners at 4½ in. centres. The clear depth of web plate was 12 in.

It was found that the expression defining the relationship between K and γ over the range $0 \leqslant \gamma \leqslant 124$ was

$$K = 11{\cdot}2 + 6{\cdot}35\,(\gamma)^{\frac{1}{3}} \quad . \quad . \quad . \quad . \quad . \quad (3)$$

In addition 25 tests involving double-sided stiffeners were done on girders BTG/7 and 8 (*see* Fig. 9). As in the previous case, the value of K increases with increasing values of γ until γ reaches a certain limiting value and, for values of γ greater than the limiting value γ_L, K remains constant.

The K/γ relationship over the range $0 < \gamma < 216$ is

$$K = 11{\cdot}2 + 7{\cdot}3\,(\gamma)^{\frac{1}{3}} \quad . \quad . \quad . \quad . \quad . \quad (4)$$

Since the ratio (clear depth of web plate)/(stiffener spacing) was the same in both of these tests, the resulting K/γ relationships provide some interesting information. Firstly, the K/γ relationships are similar in form (*see* Fig. 10). Secondly, the tests have shown that, for a given stiffener spacing, higher critical shear stresses can be obtained when using double-sided stiffeners. This is because, with double-sided stiffeners, the effective panel width is approximately equal to the clear web distance between stiffeners, whereas with single-sided stiffeners it is closer to the actual stiffener spacing.

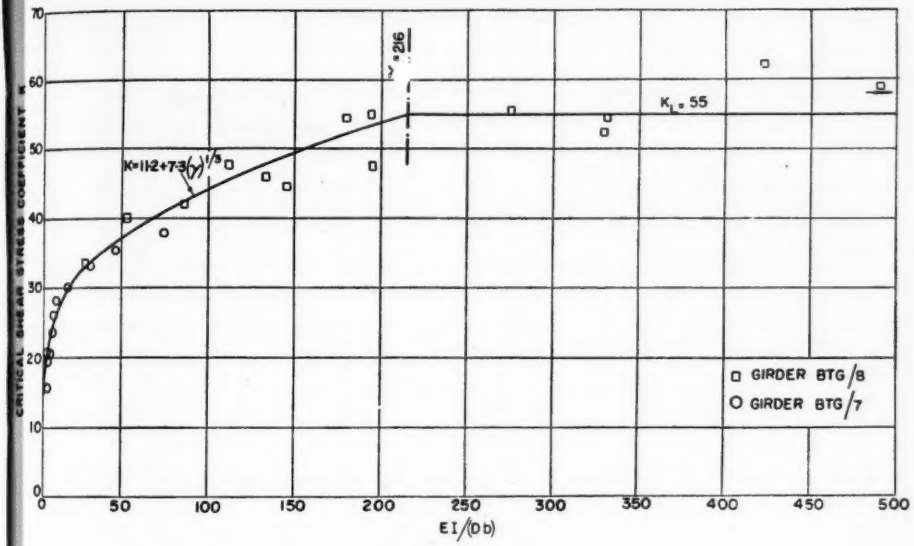

Fig. 9.

Results obtained when employing double-sided stiffeners at $4\frac{7}{8}$ in. centres. The clear depth of web plate was 12 in.

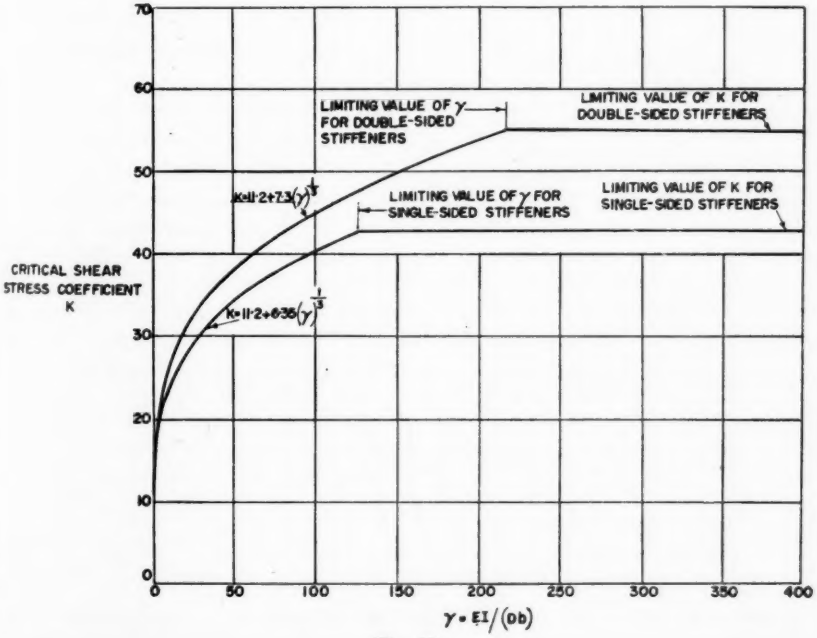
LIMITING VALUE OF γ FOR DOUBLE-SIDED STIFFENERS
LIMITING VALUE OF K FOR DOUBLE-SIDED STIFFENERS
K = 11·2+7·3(γ)^1/3
LIMITING VALUE OF γ FOR SINGLE-SIDED STIFFENERS
LIMITING VALUE OF K FOR SINGLE-SIDED STIFFENERS
CRITICAL SHEAR STRESS COEFFICIENT K
K = 11·2+6·36(γ)^1/3
γ = EI/(Db)

Fig. 10.

The experimental K/γ relationships obtained from tests involving double- and single-sided stiffeners at $4\frac{7}{8}$ in. centres on web plates having a clear depth of 12 in. *See* Figs. 8 and 9.

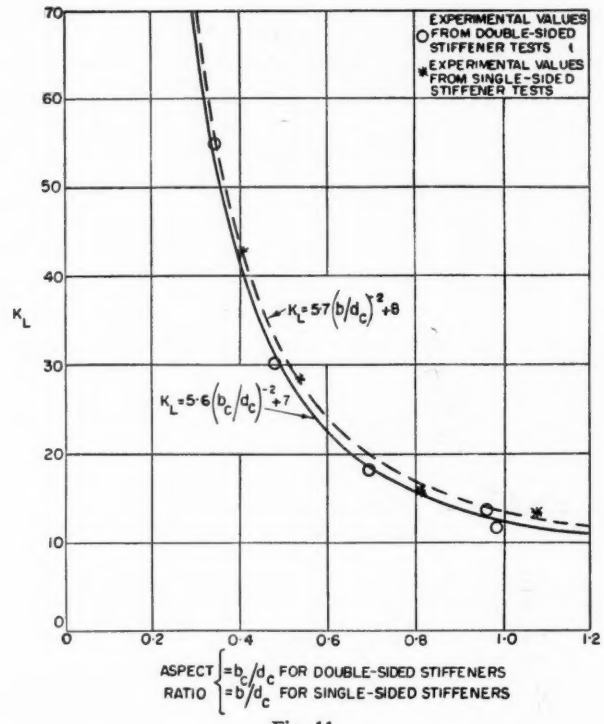

Fig. 11.

With reference to this last point, in order to determine the effect which the width of the attached stiffener leg has upon the critical shear stress of plates reinforced by single-sided stiffeners, some 28 tests were done using stiffeners with varying widths of attached legs. It was found that although, for a given value of γ, there was a tendency for the value of the critical shear stress to increase with increasing stiffener width, this increase was small and could be neglected. Fig. 10 shows that the K/γ relationships consist of two distinctly different sections. Over the first section, the value of K increases rapidly with increasing values of γ until a certain value of γ, termed the limiting value γ_L, is reached. Over the second section, that is for values of γ greater than γ_L, the value of K remains constant at K_L.

It has been seen that, over the first section, the K/γ relationship can be defined by a cubic expression similar to

$$\left.\begin{aligned} K &= K_u + A(\gamma)^{\frac{1}{3}} \\ K &= K_L \text{ for values of } \gamma \geqslant \gamma_L \end{aligned}\right\} \quad . \quad . \quad . \quad . \quad (4)$$

where K = critical shear stress coefficient of the stiffened web plate,

K_u = critical shear stress coefficient of the unstiffened plate.

Thus, provided that the values of γ_L and K_L were known, it would be a relatively simple procedure to calculate the critical shear stress of a plate stiffened by identical stiffeners equally spaced along the plate.

The values of K_L obtained from both the single- and double-sided stiffener tests have been plotted against the corresponding values of the effective aspect ratio α_e in Fig. 11.

The relationships between K_L and the effective aspect ratio α_e for single- and double-sided stiffeners are given respectively by

$$\text{Single-sided stiffeners: } K_L = 8{\cdot}0 + 5{\cdot}7\left(\frac{b}{d_c}\right)^{-2} \quad . \quad . \quad . \quad (5)$$

$$\text{Double-sided stiffeners: } K_L = 7{\cdot}0 + 5{\cdot}6\left(\frac{b_c}{d_c}\right)^{-2} \quad . \quad . \quad . \quad (6)$$

It is interesting to note that these relationships are similar in form to the approximate relationships between K and α_e for plates which are either clamped or simply-supported on all four edges[17].

The values of γ_L obtained from the tests have been plotted in Fig. 12 and the relationships between γ_L and the effective aspect ratio α_e for single- and double-sided stiffeners are respectively

$$\text{Single-sided stiffeners: } \gamma_L = 21{\cdot}5\left(\frac{b}{d_c}\right)^{-2} - 7{\cdot}5 \quad . \quad . \quad . \quad (7)$$

$$\text{Double-sided stiffeners: } \gamma_L = 27{\cdot}75\left(\frac{b_c}{d_c}\right)^{-2} - 7{\cdot}5 \quad . \quad . \quad . \quad (8)$$

The two K_L/α_e relationships are very close to each other, the curve for single-sided stiffeners lying just above the curve for double-sided stiffeners. It could be argued that the reason for this is that the effective panel width for single-sided stiffeners is a little less than the stiffener spacing and that for double-sided stiffeners is a little more than the clear web distance between stiffeners. If this is the case, then the effect would be to increase the gap between the two curves plotted in Fig. 12. It is therefore clear that different design rules should be used to determine the flexural rigidity which single- and double-sided stiffeners should possess.

With reference to Fig. 11, since the two curves are so close to each other, it is proposed that for design purposes the relationship for double-sided stiffeners (equation (6)) be used for both types of stiffening.

It is now generally accepted that, if the thickness of the attached stiffener leg is less than the thickness of the web plate, the effectiveness of the stiffener is reduced. Now, most of the tests in this investigation involved stiffeners having attached legs thicker than the web plate, because it was considered that little

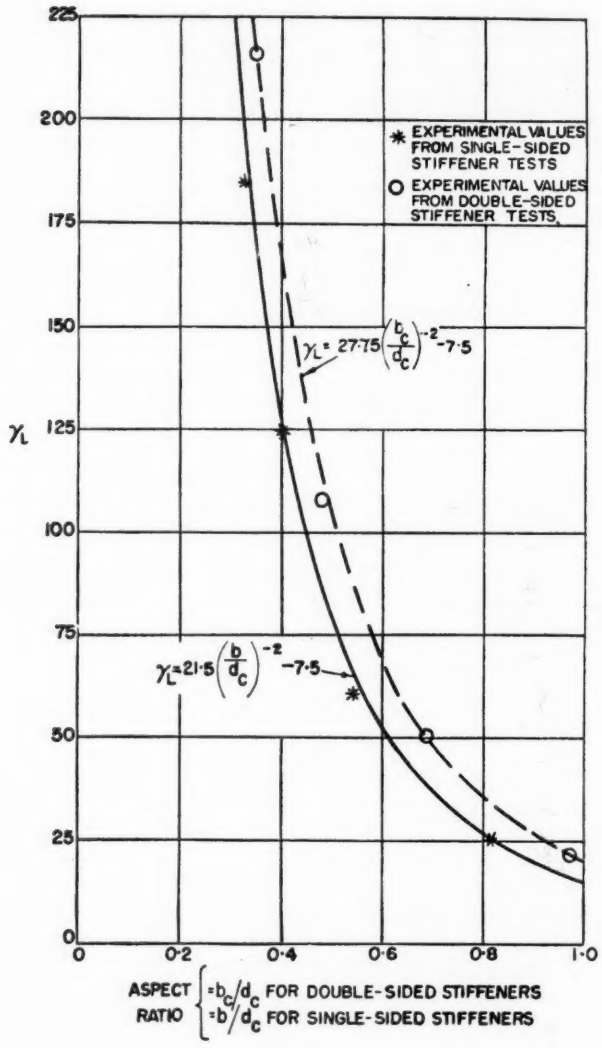

Fig. 12.

progress could be made towards estimating the influence of the t_u/t ratio until more was known about the general behaviour of intermediate stiffeners. Most of the stiffeners used had a thickness within the range t to $1{\cdot}6t$.

Therefore, until more is known about the influence of the t_u/t ratio, the empirical relationships given in equations (5) to (8) should only be used when the attached stiffener leg is equal to or greater than the thickness of the web plate.

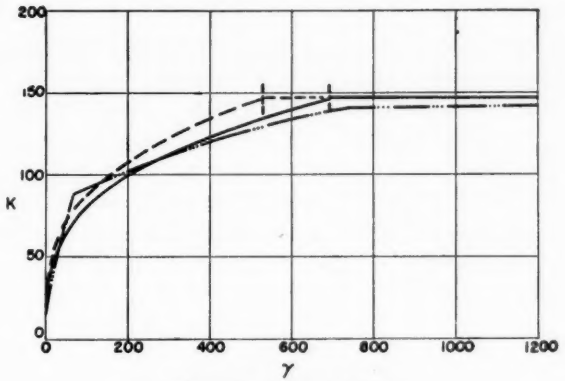

(a) EFFECTIVE ASPECT RATIO 0·2

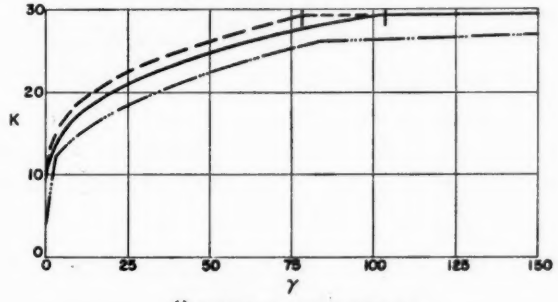

(b) EFFECTIVE ASPECT RATIO 0·5

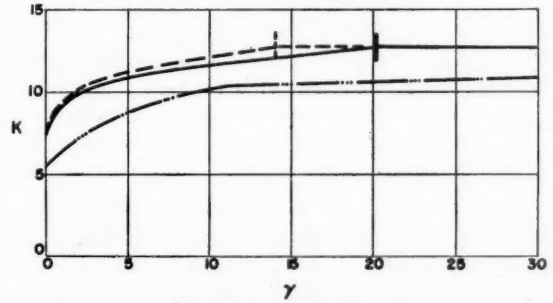

(c) EFFECTIVE ASPECT RATIO 1·0

——·——·—— STEIN AND FRALICH'S THEORETICAL RELATIONSHIPS[10]
– – – – – SINGLE-SIDED STIFFENERS. EQUATIONS (4) (6) AND (7)
——————— DOUBLE-SIDED STIFFENERS. EQUATIONS (4) (6) AND (8)

Fig. 13.

4.1. Summary of the Empirical Relationship Obtained from the Investigation

The analysis of the experimental results has shown that, for panels loaded in shear, the following empirical laws define the relationships between the critical shear stress coefficient K, the non-dimensional parameter γ, and the effective aspect ratio α_e.

$$K = K_u + A(\gamma)^{\frac{1}{4}},$$

where K_u = critical shear stress coefficient of the unstiffened plate,

K = critical shear stress coefficient of the stiffened plate, being equal to K_L for values of $\gamma \geq \gamma_L$.

A is a constant,

$$\gamma = EI/(Db)$$

$$\gamma_L = \begin{cases} 27{\cdot}75\,(\alpha_e)^{-2} - 7{\cdot}5 \text{ for double-sided stiffeners} \\ 21{\cdot}5\,(\alpha_e)^{-2} - 7{\cdot}5 \text{ for single-sided stiffeners,} \end{cases}$$

$$K_L = 7{\cdot}0 + 5{\cdot}6\,(\alpha_e)^{-2} \text{ for both single- and double-sided stiffeners,}$$

and $\alpha_e = b_c/d_c$ for double-sided stiffeners,

$\alpha_e = b/d_c$ for single-sided stiffeners.

These relationships are only valid for intermediate stiffeners having an attached stiffener leg whose thickness is equal to or greater than the thickness of the web plate.

5. Comparison of Theoretical and Experimental Values

The experimental results support in principle the theoretical work of Stein and Fralich. The form of the experimental K/γ relationships (Figs. 8, 9 and 10) is similar to that obtained theoretically by Stein and Fralich. There is, however, a difference in the magnitude of the values. This is understandable when it is appreciated that the theoretical values were derived for the case of a plate simply-supported at the edges, whereas the empirical values have been obtained from tests on practical girders in which the flange members supply a high degree of rotational restraint to the web plate.

An important difference between the theoretical and experimental work is that from the experiments it has been possible to distinguish between the behaviour of single- and double-sided stiffeners.

To provide a direct comparison between the empirical and theoretical relationships, curves have been obtained by applying equations (4), (6), (7) and (8) to the case of an infinitely long plate reinforced by stiffeners spaced at d_c, $0{\cdot}5\,d_c$ and $0{\cdot}2\,d_c$; they are plotted in Fig. 13, together with Stein and Fralich's theoretical curves. The degree of agreement increases as the stiffener spacing decreases, this no doubt being due to the fact that the increase in the buckling coefficient K obtained with the practical girders, due to rotational restraint supplied by the flanges, becomes proportionally less with a decrease in stiffener spacing.

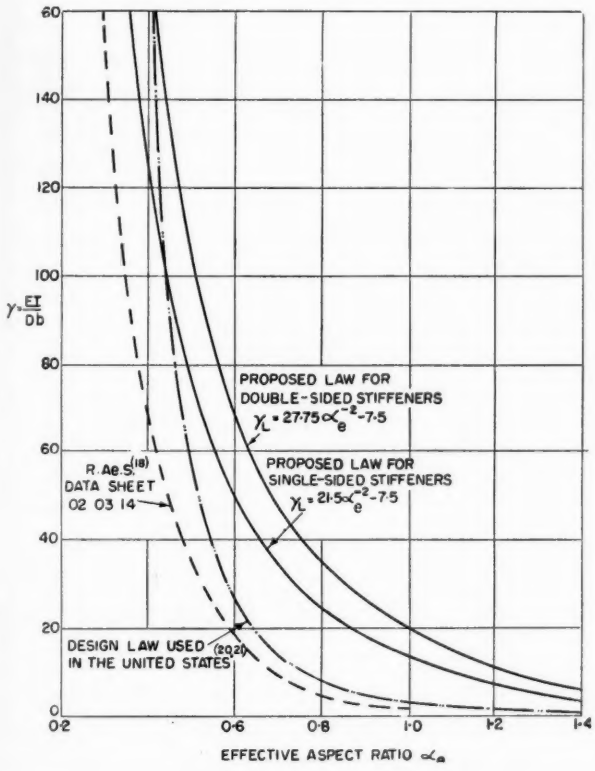

Fig. 14.

6. The Design of Intermediate Vertical Stiffeners

In view of the previous lack of information regarding the influence of the flexural rigidity of intermediate stiffeners upon the buckling stress of plate-stiffener combinations, it is not surprising to find considerable differences in the various design laws in use at the present time (Fig. 14).

It will be noted that the values of γ recommended in the Royal Aeronautical Society's Data Sheet[18] 02.03.14, and which are very close to the values recommended in the German Specification D.4114[19], are much smaller than the empirical values given by equations (7) and (8). The data sheet does recommend that when the edges of the web plate are subject to angular restraint, the value of γ should be increased by approximately 50 per cent. However, even after making this adjustment, for values of α_e greater than 0·5, the data sheet value is low. Such stiffeners will no doubt deflect with the plate and fail to form a nodal line. The same criticism also applies to the design law which is used in certain American Specifications[20, 21].

In addition to its function of increasing the buckling stress of a plate, an intermediate stiffener must help to support the flanges when the web plate is loaded

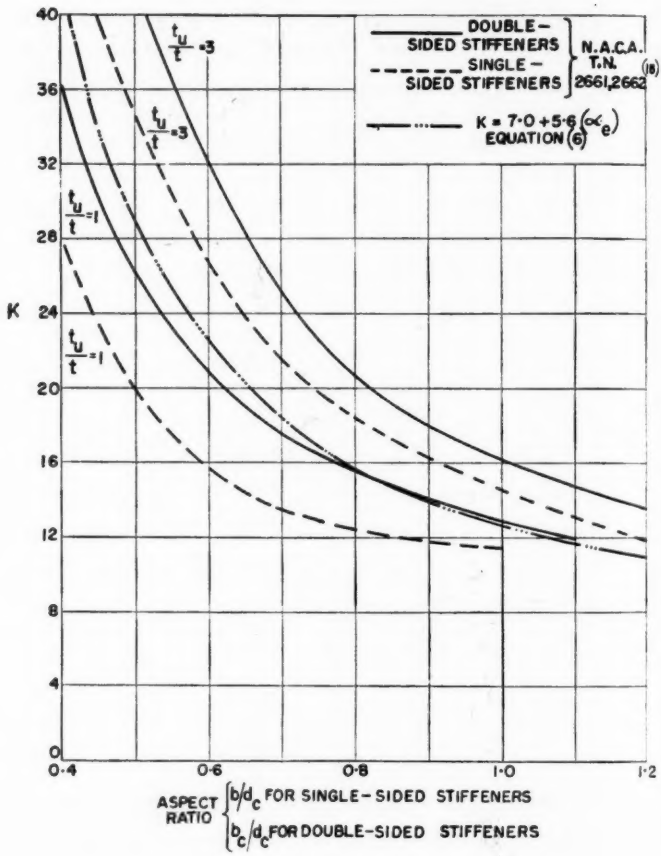

Fig. 15.

beyond its buckling load. Therefore, intermediate stiffeners on shear panels designed to operate at high values of T/T_{cr}, have to be strong and rigid in order to be capable of carrying the vertical component of the diagonal tension field. This requirement has meant that most of the stiffeners used in aircraft structures have possessed an inertia greater than that required by Data Sheet 02.03.14. However, now that more shear panels are being designed to operate at low values of T/T_{cr}, it has become necessary to know the relationships between the size and spacing of intermediate stiffeners and the buckling stress of the stiffened panels.

In the United States the National Advisory Committee for Aeronautics[15] has produced a design procedure for shear panels based upon the extensive tests conducted by Kuhn[22, 23] and others[24, 25]. This design procedure does not contain any clause which states the minimum flexural rigidity which stiffeners should possess. There are, however, two charts from which, together with a formula, the buckling stress of a stiffened panel can be calculated. Instead of employing

the flexural rigidity of the stiffener, the parameter t_u/t is used and two curves are supplied, one for single-sided stiffeners and one for double-sided stiffeners, which provide values of a restraint coefficient in terms of the parameter t_u/t. Using this design procedure, the values of the buckling coefficient K plotted in Fig. 15 can be obtained. Also plotted in Fig. 15 is the empirical relationship given by equation (6).

According to the American design procedure, for given values of the parameter t_u/t and the aspect ratio α_e, a much lower value of the critical shear stress coefficient will be obtained with single-sided stiffeners than with double-sided stiffeners. The investigation conducted by the author has indicated, however, that the value of K obtained with single-sided stiffeners will be very close to the value obtained with double-sided stiffeners spaced so as to provide the same value of α_e. In fact, in Fig. 11 the curve for single-sided stiffeners actually lies just above the curve for double-sided stiffeners.

Another point of interest is that, as a result of the tests, it is doubtful whether there will be so large a gain in the value of K by using values of t_u/t greater than 1, as is indicated in Ref. 15.

A further series of tests is now being done to investigate more fully the parameter t_u/t and, now that the general relationships between the variables K, γ and α_e are known, it is expected that it will be possible to determine quite accurately the influence of the parameter t_u/t.

7. Conclusion

The empirical relationships between the buckling stress of a stiffened panel and the flexural rigidity and spacing of the intermediate stiffeners, which have been presented in this paper, will enable designers to predict with greater accuracy the buckling load of uniformly stiffened plates subjected to shear. One important feature of the new relationships is the different formulae which have been obtained for single- and double-sided stiffeners, thus defining more clearly than hitherto the difference in the effect of the two types of reinforcement.

ACKNOWLEDGMENTS

The investigation described in this paper was carried out in the Engineering Department of the University College of Swansea and was sponsored by the Aluminium Development Association.

REFERENCES

1. TIMOSHENKO, S. *Theory of Elastic Stability.* McGraw-Hill, New York, 1936.
2. STEIN, M. and NEFF, J. Buckling Stress of Simply Supported Rectangular Flat Plates in Shear. N.A.C.A.. T.N. 1222, 1947.
3. BUDIANSKY, B. and CONNOR, R. W. Buckling Stresses of Clamped Rectangular Flat Plates in Shear. N.A.C.A. T.N. 1559, 1948.

4. SCHMIEDEN, C. The Buckling of Stiffened Plates in Shear. Translation No. 31, U.S. Experimental Model Basin, Washington Navy Yard, June 1936.

5. SEYDEL, E. Wrinkling of Reinforced Plates subjected to Shear Stresses. N.A.C.A. T.M. 602, 1931.

6. WANG, T. K. Buckling of Transverse Stiffened Plates under Shear. *Journal of Applied Mechanics*, Vol. 14, No. 4, December 1947.

7. SEYDEL, E. The Critical Shear Load of Rectangular Plates. N.A.C.A. T.M. 705, 1933.

8. MELCON, M. A. and ENSRUD, A. F. Analysis of Stiffened Curved Panels under Shear and Compression. *Journal of the Aeronautical Sciences*, Vol. 20, p. 111, February 1953.

9. WAY, S. Stability of Rectangular Plates under Shear and Bending Forces. *Journal of Applied Mechanics*, Vol. 3, No. 4, December 1936.

10. STEIN, M. and FRALICH, R. W. Critical Shear Stress of Infinitely Long, Simply Supported Plate with Transverse Stiffeners. N.A.C.A. T.N. 1851, 1949.

11. MOORE, R. L. An Investigation on the Effectiveness of Stiffeners on Shear Resistant Plate Girder Webs. N.A.C.A. T.N. 862, September 1942.

12. SCOTT, M. and WEBER, R. L. Requirements for Auxiliary Stiffeners attached to Panels under Combined Compression and Shear. N.A.C.A. T.N. 921, 1943.

13. SPARKES, S. R. The Behaviour of the Webs of Plate Girders. *Welding Research*, Vol. 10, No. 6, 1947.

14. British Standard 1470. Wrought Aluminium and Aluminium Alloys. British Standards Institution, 1948.

15. KUHN, P., PETERSON, J. P. and LEVIN, L. R. A Summary of Diagonal Tension. Parts I and II. N.A.C.A. T.N. 2661 and 2662, May 1952.

16. KUHN, P. and LEVIN, L. R. An Empirical Formula for the Critical Shear Stress of Curved Plates. N.A.C.A. A.R.R. L5.AO5, 1945.

17. BLEICH, F. *Buckling Strength of Metal Structures.* McGraw-Hill, New York, 1952.

18. Royal Aeronautical Society Data Sheet 02.03.14. Minimum Stiffness Criterion for Stiffeners in a Shear Panel, May 1945.

19. German Standard Stabilitätsfalle (Knickung, Kippung, Beulung). DIN 4114, Blatt 2, July 1952.

20. Specifications for the Design and Fabrication of Structures of Alcoa Aluminum Alloy 61S-T6. Aluminum Company of America, April 1948.

21. Specifications for Heavy Duty Structures of High Strength Aluminum Alloy. *Proceedings of the American Society of Civil Engineers*, Vol. 76, No. 22, June 1950.

22. KUHN, PAUL and PETERSON, J. P. Strength Analysis of Stiffened Beam Webs. N.A.C.A. T.M. 1364, 1947.

23. KUHN, P. and CHIARITO, P.T. The Strength of Plane Web Systems in Incomplete Diagonal Tension. N.A.C.A. A.R.R. WR L-367, August 1942.

24. LEVIN, L. R. and SANDLIN, C. W. Strength Analysis of Stiffened Thick Beam Webs. N.A.C.A. T.N. 1820, 1949.

25. LEVIN, L. R. Ultimate Stresses developed by 24S-T and 75S-T Aluminum Alloy Sheet in Incomplete Diagonal Tension. N.A.C.A. T.N. 1756, 1948.

Photoelastic Investigation on Plates with Single Interference-Fit Pins with Load Applied to Plate Only

H. T. JESSOP, C. SNELL and G. S. HOLISTER

(*Department of Civil and Municipal Engineering, University College, London*)

SUMMARY: The introduction of an interference-fit pin in a circular hole in a flat plate is found to result in a reduction in the stress concentration factor at the hole boundary under tension applied to the plate. The S.C.F. decreases rapidly with increase in the ratio of interference stress to applied tension, and decreases also with increase in the ratio of hole diameter to width of plate. Very little difference in the S.C.F. is found for different ratios of Young's modulus of pin and plate.

I. Introduction

This is the third stage of the photoelastic tests in a programme of research initiated by the Royal Aeronautical Society and outlined in Ref. 1. The first and second stages dealt with the stress distributions in tension plates with unfilled holes, and holes filled by a push-fit pin, respectively, and the results were published in Refs. 2 and 3. This investigation deals with tension plates with circular holes filled by interference-fit pins, with the load applied to the plate only.

NOTATION

D	width of plate
d	nominal diameter of empty hole
$d+\varepsilon$	diameter of pin
E	Young's modulus of plate [E (bar)]*
E_1	Young's modulus of pin [E (pin)]*
ν	Poisson's ratio of plate
G	modulus of rigidity of plate $= E/\{2(1+\nu)\}$
p, q	principal stresses

*The symbol in square brackets is the one which has been used in previous papers.

Received September 1955.

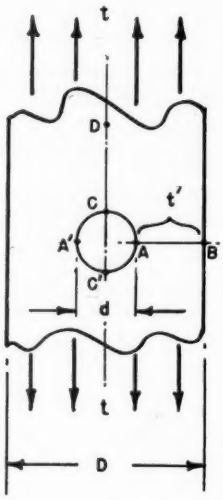

Fig. 1.

σ_r, σ_θ radial and circumferential normal stresses

t mean tensile stress in undrilled plate due to applied tension $[t_0]$*

$t' = Dt/(D-d)$, nominal mean tensile stress across section through the centre, due to applied tension $[t'_0]$*

t_m maximum tensile stress on hole boundary

$s_m = \frac{1}{2}(p-q)_m$, maximum shear stress on hole boundary.

The stress concentration factors derived here are given in terms of the *increase* in peak tensile or shear stress produced by the applied tension.

Thus, S.C.F. for tensile stresses $= \delta t_m/t'$
S.C.F. for shear stresses $= \delta s_m/t'$.

2. Conditions of Tests

2.1. The Models

As in previous tests the models were Araldite plates, 1 in. wide and $\frac{1}{8}$ in. thick, with four hole sizes: $-\frac{1}{8}$, $\frac{1}{4}$, $\frac{3}{8}$ and $\frac{1}{2}$ in. diameter respectively.

Most of the tests were made with pins of brass and Araldite, but a few were made with a type of filled Bakelite. The ratio of the Young's moduli for the pins were: –

	Brass	Bakelite	Araldite
$E_1/E =$	30	2·15	1.

*The symbol in square brackets is the one which has been used in previous papers.

2.2. Degrees of Interference

Two degrees of interference were examined for each size of hole. These were approximately

0·3 per cent and 0·7 per cent for the brass pins
0·4 per cent and 0·9 per cent for the Araldite and Bakelite pins.

These values were found to give comparable amounts of interference stress with the different pin materials and they are specified as "low" and "high" interference respectively.

These two degrees of interference would produce in light alloy plates *maximum elastic shear stresses* at the hole boundary of approximately 21,000 lb. /in.^{2} and 50,000 lb./in.^{2} respectively.

2.3. Applied Tensions

In the first tests, two different tensions were applied to each plate for each degree of interference. In relation to the strains produced these would correspond to *mean elastic tensile stresses* in light alloy plates of 15,000 lb./in.^{2} and 30,000 lb./in.^{2} in the undrilled plate.

Later, in order to trace the changes in S.C.F's more thoroughly, it was found necessary to subject the plates to a range corresponding to 0 to 40,000 lb./in.^{2} in the light alloy.

2.4. Method of Tests

The fringe patterns under the various loads were photographed in light and dark fields on 35 mm. film, and the boundary shear stresses were obtained by extrapolation from graphs plotted from enlargements of the photographs.

To obtain the tensile stresses on the boundary, sets of isoclinic fringes were traced in the projecting polariscope and the separate stresses were evaluated by graphical integration of the equations of equilibrium along the horizontal and vertical axes of symmetry.

3. Stresses due to Interference Fit of Pin

3.1. Degree of Interference

Preliminary tests showed that measurement of the diameters of pin and hole failed to give a reliable estimate of the interference stresses to be expected in a plate, and that this was due to inability to measure the hole diameter to a sufficient degree of accuracy. Further tests with a series of pins measured to an accuracy of 0·0001 in. and inserted in the same hole showed that the shear stress on the hole boundary varied linearly with the diameter of the pin. Extrapolation from a graph then yielded the point at which the production of zero stress indicated the effective hole diameter. In every case tested this was found to be somewhat greater than the measured hole diameter.

In the tests described here therefore, the holes and pins were turned to give as nearly as possible the required degree of interference stress, and this stress, as measured from the photoelastic fringe pattern, was taken to indicate the degree of interference obtained.

3.2. The Shear Stresses

Figures 2 and 3 show the photoelastic fringe patterns in a plate with a $\frac{3}{8}$ in. diameter hole, with low and high interference respectively. The dark fringes are loci of equal shear stress, the stress at each fringe being proportional to the fringe number as shown by the numbers on the photographs.

In all cases the stress around the hole boundary was subject to small variations, through lack of perfect circularity of pin and hole. Also the presence of the pin tended to mask observation of the boundary itself, so that the value of the true boundary stress had to be found by extrapolation from a graph of the stresses along a radial line. The values of the peak fringe numbers so obtained are liable to errors of the order of one-fifth of a fringe (*i.e.* about 5 per cent in the most unfavourable case). Within this limit of error it was found that:—

(*i*) The value of the maximum shear stress was constant around the hole boundary. This applied for all hole sizes and for both low and high interference.

(*ii*) The shear stress on the hole boundary for a given degree of interference was the same for all hole sizes.

(*iii*) The magnitudes of the maximum shear stresses agreed with those given by the theoretical solutions for an oversized pin in an infinite plate. (*See* Appendix).

3.3. The Separate Stresses

(*i*) At the hole boundary on the vertical axis of symmetry (points C, C' in Fig. 1) the circumferential tension and radial compression are equal in magnitude, *i.e.* $\sigma_r = |-\sigma_\theta$ as in the infinite plate solution.

(*ii*) At the hole boundary on the horizontal axis, (points A, A' in Fig. 1), the circumferential tension is greater and the radial compression less, the difference being small for the $\frac{1}{8}$ in. diameter hole, and increasing with the hole size.

The increase in σ_θ and the decrease in $|\sigma_r|$ due to finite width of the plate were, in fact, equal and so caused no variation in shear stress around the hole.

4. Qualitative Effects of Application of Tension to the Plate

Figures 4 and 5 show photoelastic fringe patterns for the plate with a $\frac{3}{8}$ in. diameter hole under tension, Fig. 4 when a small tension is applied with the high interference pin, Fig. 5 when a large tension is applied with the low interference pin.

Fig. 2.
Fringe pattern due to interference fit of pin. $\frac{1}{8}$ in. diameter hole, brass pin, low interference.

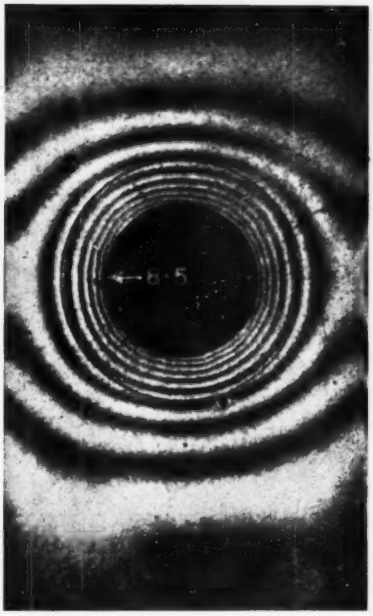

Fig. 3.
Fringe pattern due to interference fit of pin. $\frac{1}{8}$ in. diameter hole, brass pin, high interference.

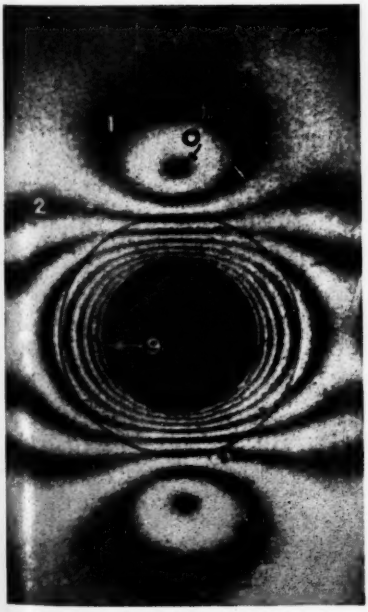

Fig. 4.
Fringe pattern in plate with high interference and low applied tension.

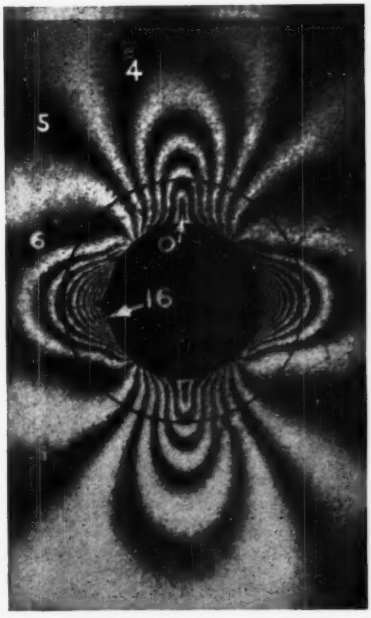

Fig. 5.
Fringe pattern in plate with low interference and high applied tension.

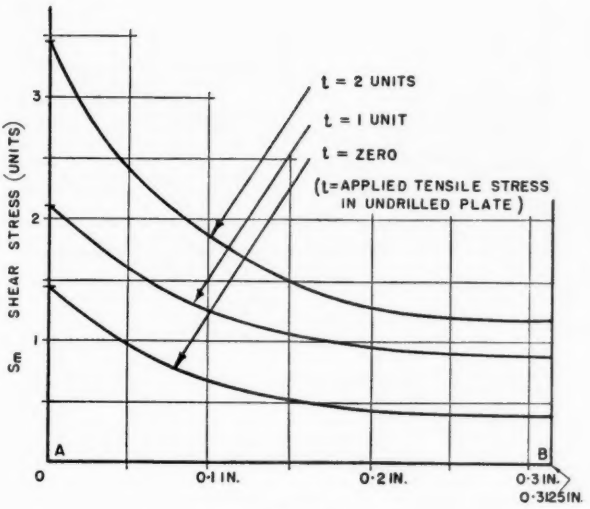

Fig. 6.

Shear stresses on horizontal section AB in plate with $\frac{1}{8}$ in. hole with low interference under zero, low and high loads.

The two points of zero shear stress above and below the hole in Fig. 4 are approximately the points at which the applied vertical tension has neutralised the vertical compression due to interference. In the region between these points and the hole the plate still retains, in this case, some of its initial circumferential tension and radial compression.

As the ratio of applied tension to interference stress increases, these points move closer to the hole, the pressure between pin and plate at the top and bottom of the hole decreases, and slip begins to occur. Eventually the plate begins to "lift" from the pin, and in these top and bottom regions the hole boundary becomes "free" and is subject only to a small circumferential compressive stress. This is the condition illustrated in Fig. 5.

The foregoing sequence is followed as the applied tension increases, for both low and high degrees of interference, but in this series of tests the tensions applied did not reach a sufficiently high value to produce lift with the high interference pin.

5. The Shear Stresses due to Applied Tension

5.1. The Effect of "Lift"

With the low interference pins, lift first became visible under an applied tension t approximately equal to the initial circumferential tension produced by the interference. Lift at top and bottom points must have begun at a somewhat lower load.

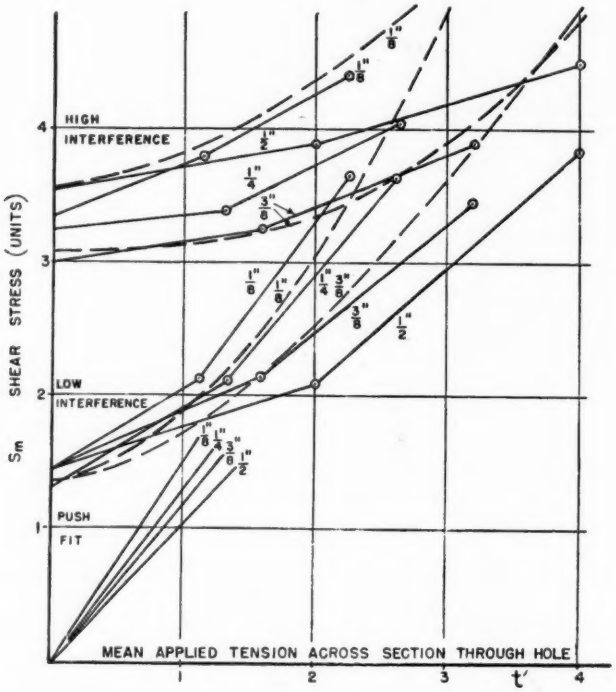

Fig. 7.
Shear stresses on the hole boundary at *A* under low and high loads.

In the early tests, in which two loads only were applied to each plate, a marked increase in S.C.F's on the horizontal section was observed under loads which produced lift. The later tests under progressively increasing load showed, however, that the changes in S.C.F. were continuous and that there was no sudden change in either the S.C.F. or its rate of increase corresponding to the actual occurrence of lift.

5.2. The Shear Stresses on the Horizontal Section

(*i*) Fig. 6 shows the distribution of shear stress* on the horizontal axis of symmetry for the low degree of interference under zero, low and high loads for the $\frac{3}{8}$ in. diameter hole. The distributions are qualitatively very similar for the other hole sizes.

(*ii*) Table I and Fig. 7 show the shear stresses* at the point *A* under both loads for all hole sizes. Also shown, in broken lines on Fig. 7, are the values for the $\frac{1}{8}$ in. and $\frac{3}{8}$ in. holes under gradually increasing load. (These latter curves were obtained from different models from those used in the low and high load observations.)

*The unit of stress corresponds to 15,000 lb./in.^{2} in a light alloy bar.

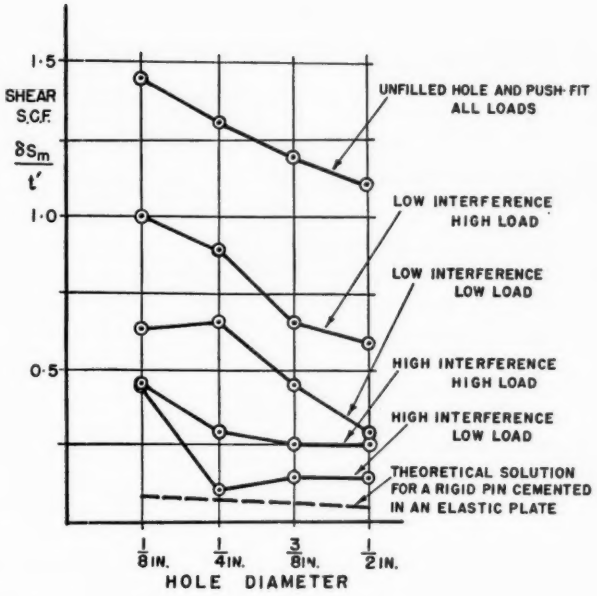

Fig. 8.
Shear stress concentration factors at *A* for low and high loads.

TABLE I

SHEAR STRESS AT HOLE BOUNDARY ON HORIZONTAL SECTION

	Shear stress at A (units)*			*Increments* (units)		*S.C.F.*	
Hole diameter (in.)	Zero load	Low load	High load	Low load	High load	Low load	High load
			(*i*) *Low interference*				
$\frac{1}{8}$	1·45	2·15	3·65	0·70	2·20	0·60	1·00
$\frac{1}{4}$	1·30	2·15	3·65	0·85	2·35	0·65	0·90
$\frac{3}{8}$	1·45	2·15	3·45	0·70	2·05	0·45	0·65
$\frac{1}{2}$	1·50	2·10	3·85	0·60	2·35	0·30	0·60
			(*ii*) *High interference*				
$\frac{1}{8}$	3·35	3·85	4·40	0·50	1·05	0·45	0·45
$\frac{1}{4}$	3·25	3·40	4·05	0·15	0·75	0·10	0·30
$\frac{3}{8}$	3·00	3·25	2·85	0·25	0·85	0·15	0·25
$\frac{1}{2}$	3·55	3·85	4·50	0·30	0·95	0·15	0·25

*In this and subsequent tables the unit of stress corresponds to 15,000 lb./in.^{2} in a light alloy bar.

TABLE II

SHEAR STRESS AT HOLE BOUNDARY ON VERTICAL SECTION

Hole diameter (in.)	*Shear stress at C* (units)*			*Increments* (units)		*S.C.F.*	
	Zero load	Low load	High load	Low load	High load	Low load	High load
			(*i*) *Low interference*				
$\frac{1}{8}$	1·43	0·66	−0·05	−0·75	−1·50	−0·66	−0·70
$\frac{1}{4}$	1·30	0·60	0·06	−0·70	−1·25	−0·52	−0·47
$\frac{3}{8}$	1·46	0·66	0·26	−0·80	−1·20	−0·50	−0·38
$\frac{1}{2}$	1·50	0·60	0·33	−0·90	−1·15	−0·45	−0·57
			(*ii*) *High interference*				
$\frac{1}{8}$	3·33	2·56	1·85	−0·75	−1·50	−0·66	−0·65
$\frac{1}{4}$	3·26	2·30	1·46	−1·10	−1·80	−0·82	−0·80
$\frac{3}{8}$	3·24	2·35	1·46	−0·90	−1·75	−0·56	−0·54
$\frac{1}{2}$	3·45	2·45	1·60	−1·00	−1·85	−0·50	−0·46

On Fig. 7 are also shown the shear stress graphs for a plate with push-fit pin. For the latter stages of loading, with the low interference pin, *i.e.* after lift has occurred, the rate of increase of stress with load approaches that in the push-fit case.

(*iii*) Fig. 8 shows the values of S.C.F. as given in Table I, together with those for the push-fit pin and for the theoretical solution for a rigid pin "fixed" in an infinite plate. (*See* Appendix).

5.3. The Shear Stresses on the Vertical Section

Table II shows the shear stresses on the vertical section at the point *C* on the hole boundary for the same series of tests as before. The addition of tension causes a reduction in the shear stress throughout the range of loading applied.

While there is a general tendency for the S.C.F. to decrease slightly numerically with increase in hole diameter, this effect is small and irregular, and is probably influenced by small differences in the contact conditions with different pins.

There is no significant difference in S.C.F. for either change of load or change of degree of interference until after the occurrence of lift, when a small reduction in the factors occurs with increasing load.

*The unit of stress corresponds to 15,000 lb./in.^{2} in a light alloy bar.

TABLE III

TENSION AT HOLE BOUNDARY ON HORIZONTAL SECTION

Hole diameter (in.)	Tensile stress at A (units)*			Increments (units)		S.C.F.	
	Zero load	Low load	High load	Low load	High load	Low load	High load
			(*i*) *Low interference*				
⅛	1·57	2·13	4·27	0·56	2·70	0·50	1·10
¼	1·43	2·54	4·54	1·11	3·11	0·80	1.20
⅜	1·70	2·47	4·07	0·77	2·37	0·50	0·70
½	2·20	2·60	4·80	0·40	2·60	0·20	0·60
			(*ii*) *High interference*				
⅛	3·56	4·40	5·20	0·84	1·64	0·70	0·70
¼	3·60	3·80	4·60	0·20	1·00	0·20	0·40
⅜	3·60	3·67	3·87	0·07	0·27	0·05	0·10
½	4·80	4·94	5·60	0·14	0·80	0·10	0·20

6. The Tensile Stresses due to Applied Tension

6.1. The Tensile Stresses on the Horizontal Section

These are shown in Table III. The values obtained for stress increases under load are subject in this case to the errors involved in two graphical integrations—one for the tension, due to interference, and one for the total tension under load—in addition to actual observation errors. The values of S.C.F., therefore, show more irregularity than those for the shear stresses; but they show the same general trends as the shear stresses: – a general decrease with hole diameter, as would be expected, and a marked increase when the ratio of applied load to initial interference stress becomes high.

In the most unfavourable case, that of the ⅛ in. hole with approximately 0·3 per cent interference and high load, the S.C.F. is still only about one half of that for the same hole with a push-fit pin.

6.2. Circumferential Stresses

Table IV gives the results for the circumferential stress at points C, C' on the vertical section. As for the shear stress at the same points, the S.C.F. is consistently negative. Under high loads with low degree of interference the circumferential stress may change sign and become a small compression. Accurate evaluation of the separate stresses becomes difficult in this case, however, owing to the difficulty of integrating through the isotropic points, and the values given can only be taken as indicating the order of the tensile S.C.F. at these points.

*The unit of stress corresponds to 15,000 lb./in.² in a light alloy bar.

TABLE IV

TENSION AT HOLE BOUNDARY ON VERTICAL SECTION

Hole diameter (in.)	*Tensile stress at C* (units)*			*Increments* (units)		*S.C.F.*	
	Zero load	Low load	High load	Low load	High load	Low load	High load
			(*i*) *Low interference*				
$\frac{1}{8}$	1·47	1·20	−0·10	−0·37	−1·50	−0·32	−0·68
$\frac{1}{4}$	1·30	0·93	0·13	−0·37	−1·70	−0·28	−0·63
$\frac{3}{8}$	1·47	1·17	0·53	−0·30	−0·90	−0·22	−0·30
$\frac{1}{2}$	1·50	1·90	0·67	−0·60	−0·83	−0·30	−0·40
			(*ii*) *High interference*				
$\frac{1}{8}$	3·34	2·94	2·00	−0·40	−1·34	−0·35	−0·52
$\frac{1}{4}$	3·27	2·53	2·00	−0·74	−1·27	−0·55	−0·48
$\frac{3}{8}$	3·24	3·06	2·60	−0·18	−0·64	−0·11	−0·20
$\frac{1}{2}$	3·47	2·93	2·07	−0·54	−1·40	−0·27	−0·35

7. Comparison of Results for Pins of Different Materials

Plates with pins of brass and Araldite were tested under progressively increasing load with both degrees of interference for three hole sizes, $\frac{1}{8}$ in., $\frac{3}{8}$ in. and $\frac{1}{2}$ in. diameter.

The plate with $\frac{1}{2}$ in. diameter hole was also tested with a Bakelite pin.

Figures 9 and 10 show the shear stresses at *A* and *C* respectively for the $\frac{3}{8}$ in. hole. The other hole sizes gave very similar graphs.

Figure 11 shows graphs of the S.C.F's at the point *A* for all the tests. These values were derived from graphs similar to those of Fig. 9, and represent in each case the ratio of total change in shear stress to applied tension.

In all except two cases the difference between the S.C.F's for brass and Araldite pins is nowhere greater than 0·2. (The two exceptions occur on the vertical section in the early stages of loading with high interference, and may well be attributable to some sort of "settling down" process at the contact surface.)

8. Summary of Results for All Tests

The two critical points on the hole boundary are those at the extremities of the vertical and horizontal diameters. In the former the S.C.F. is always negative, so that the maximum stresses there, both shear and tensile, are those due to the interference fit of the pin. Also the S.C.F's at these points are only substantially greater than those on the horizontal diameter in the case of small loads. On the horizontal diameter the interference stresses are the minimum stresses, and under medium or

*The unit of stress corresponds to 15,000 lb./in.² in a light alloy bar.

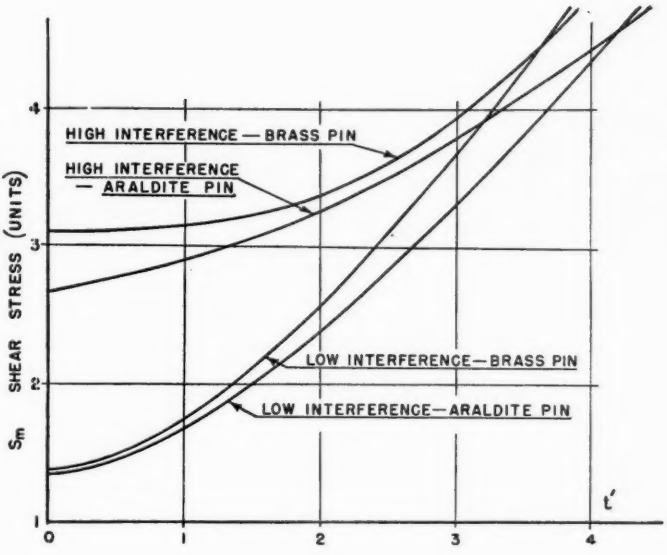

Fig. 9.
Shear stresses at *A* under progressive loading for brass and Araldite pins.

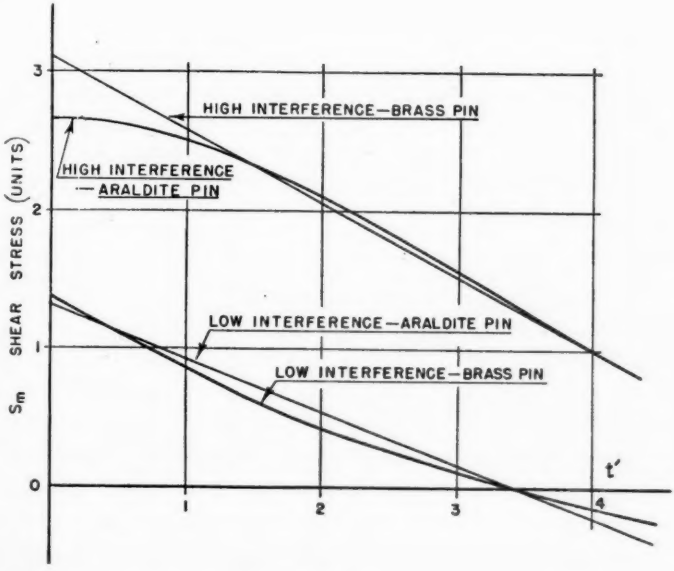

Fig. 10.
Shear stresses at *C* under progressive loading for brass and Araldite pins.

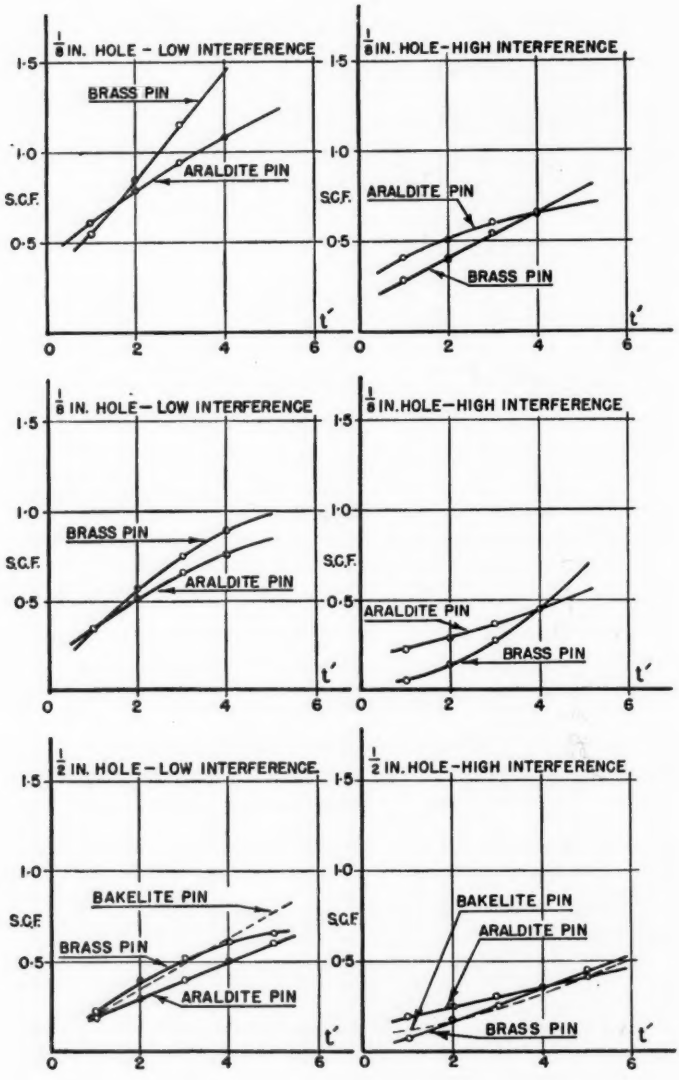

Fig. 11.

Stress concentration factors at *A* for all load and interference conditions.

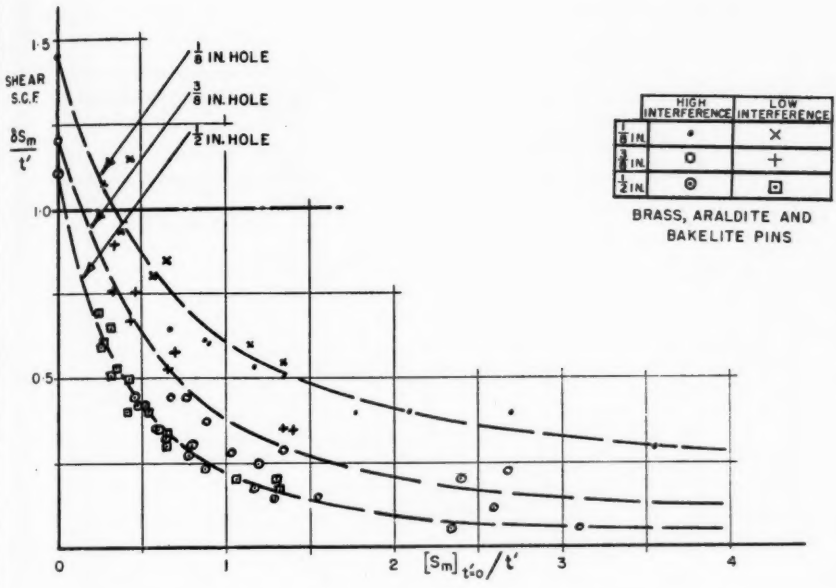

Fig. 12.
Shear stress concentration factor at *A* plotted against ratio of interference stress to applied tension.

high loads the S.C.F's are of the same order of magnitude as those on the vertical diameter. Attention was therefore concentrated upon the points on the horizontal diameter where, in addition, experience had shown that fatigue failure almost invariably occurred.

The trend of the results obtained suggested that the S.C.F. was related, at least qualitatively, to the ratio of degree of interference to magnitude of applied load.

Values of S.C.F. on the horizontal section were, therefore, plotted against the ratio of interference stress to mean applied stress across the section through the hole, and these graphs are shown in Figs. 12 and 13. In Fig. 12 the points plotted include those for all three pin materials, but values of the tensile S.C.F. were obtained only in the brass pin cases.

The accuracy of the S.C.F. as estimated from possible experimental errors is of the order of $\pm$ 0·1, so that the curves drawn in these graphs give a very fair representation of the relation as deduced from the photoelastic tests.

The facts that the values of low and high degrees of interference conform so well to the same curves, and that these curves tend toward the points for zero

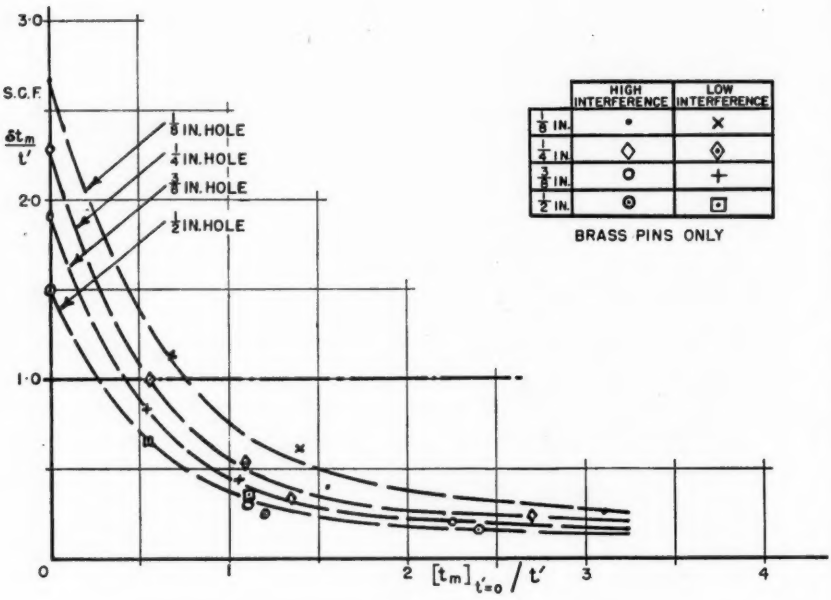

Fig. 13.
Tensile stress concentration factor at A plotted against ratio of interference stress to applied tension.

interference as obtained from the push-fit pin tests[3], indicates that the ratio of interference stress to applied tension is in fact a suitable criterion to adopt for estimation of S.C.F's in this problem.

The significance of these results in the case where the applied tension alternates between zero and a known value t' is probably best seen by plotting the "mean stress-level" (*i.e.* the mean of initial and final values of stress), and the amplitude of the oscillation about this mean value. These will be given by $(x+\frac{1}{2}y)\,t'$ and $(\frac{1}{2}y)\,t'$ respectively from Figs. 12 and 13. In Fig. 14 this has been done for the shear stress for the $\frac{3}{8}$ in. diameter hole.

It is obvious that the stress level rises very rapidly at high degrees of interference and that the useful part of the graph lies in the region of comparatively low ratio of interference to applied load.

9. Effect of Cyclic Application of Loads

Figure 15 shows the shear stresses on the horizontal hole boundary under sequences of loading and unloading. The general effect is to produce a flattening of the stress-load curve in the region of low applied load. This is more pronounced with the high degree of interference. The stresses under the higher loads appear to be unaffected in both cases.

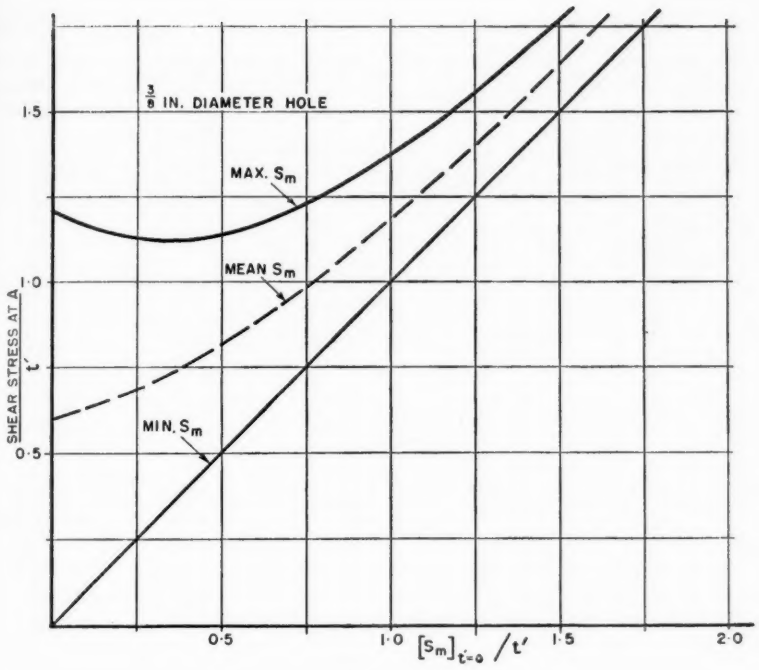

Fig. 14.

Mean value and amplitude of oscillations of shear stress at A for load varying from zero to t', plotted against degree of interference.

The effect of repeated loading and unloading would be, therefore, to raise the mean stress level slightly, while reducing the amplitude of the oscillation.

It should be noted, however, that these effects are likely to vary with different surface contact conditions between pin and plate, and the results cannot be taken as applying quantitatively to pins and plates of different materials.

10. Effect of Plastic Yield in Prototype

The results in these photoelastic tests are valid only so long as the stress distribution in the plate is an elastic one.

If in the prototype the interference is so high that an annulus of the plate surrounding the hole has undergone complete plastic yield, two modifications will be introduced:—

(*i*) The amount of vertical tension which the material above and below the hole can sustain without approaching the conditions in which "slip" and

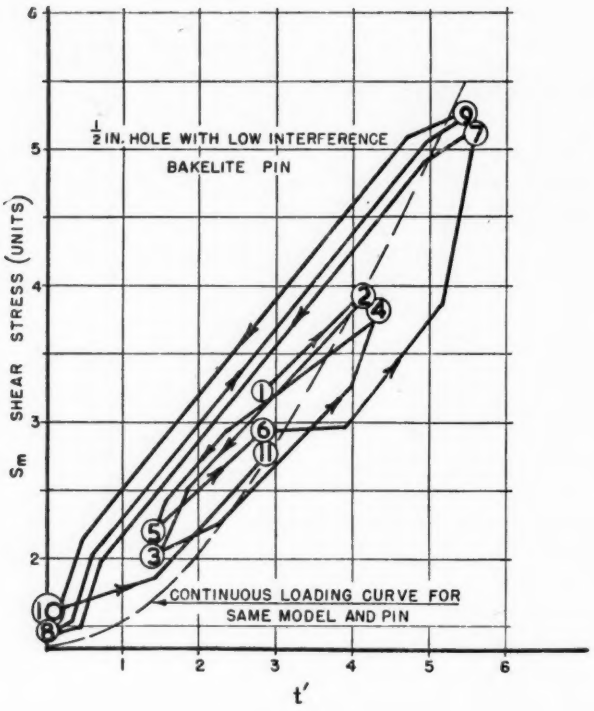

Fig. 15.

Shear stresses at *A* under cycles of loading and unloading, with low interference.

"lift" occur is limited to the maximum radial compressive stress in the plastic annulus. For loads which produce tensions above this limit it is to be expected that a greater portion of the total tension will act across the horizontal section of the plate than in the corresponding elastic distribution.

(*ii*) The material in the "plastic" annulus at the sides of the hole cannot sustain as much additional circumferential tension, so that, whatever the magnitude of the applied load, more of the additional stress must be borne by the remainder of the horizontal section and the area of plastic yield will be extended.

Qualitatively it would appear that plastic yield in the plate, whether produced by the interference alone or by the total effect of interference and load, would tend to reduce the fatigue strength.

REFERENCES

1. WILKINS, E. W. C. and JESSOP, H. T. A Photoelastic-Fatigue Programme of Experimental Research in Connection with Bolted Joints. *Journal of the Royal Aeronautical Society*, June 1954.

2. JESSOP, H. T., SNELL, C. and JONES, I. Results of Photoelastic Investigation of Stresses in a Tension Bar with Unfilled Hole. *Journal of the Royal Aeronautical Society*, January 1955.

3. JESSOP, H. T., SNELL, C. and HOLISTER, G. S. Photoelastic Investigation in Connection with the Fatigue Strength of Bolted Joints (Tension Bar with Hole having a Push-Fit Pin with Load applied to Plate Only). *The Aeronautical Quarterly*, August 1955.

Appendix

Some of the results of the tests have been compared with the following theoretical solutions due to A. C. Stevenson.

(*a*) *Theoretical Solutions for Pins with Interference Fit in a Circular Hole in an Infinite Plate.*

(*i*) For a rigid pin of diameter $(d+\varepsilon)$ inserted in a hole of diameter d in an infinite plate, the stresses at the hole boundary are given by

$$\sigma_\theta = -\sigma_r = 2G\frac{\varepsilon}{d},$$

where G = the rigidity of the plate $= \dfrac{E}{2(1+\nu)}$.

(*ii*) For a pin of the same material as the plate

$$\sigma_\theta = -\sigma_r = \frac{E}{2}\,\frac{\varepsilon}{d}.$$

(*iii*) For a pin of modulus E_1 and Poisson's ratio ν_1 in a plate of moduli E, ν,

$$\sigma_\theta = -\sigma_r = \frac{1}{\dfrac{1-\nu_1}{E_1} + \dfrac{1+\nu}{E}}\,\frac{\varepsilon}{d}.$$

For a steel pin ($E_1 = 30\times10^6$, $\nu_1 = 0{\cdot}25$), in a light alloy plate ($E = 10\times10^6$, $\nu = 0{\cdot}25$), this becomes

$$\sigma_\theta = -\sigma_r = 2\frac{E}{3}\,\frac{\varepsilon}{d}.$$

(*b*) *Theoretical Solution for a "Rigid" Circular Inclusion "Fixed" in an Infinite Plate under Tension T.*

(This solution assumes no displacements of the plate at the hole boundary).

At the edge of the hole on the horizontal section,

$$\sigma_\theta = T\nu\left(1 - \frac{2}{3-4\nu}\right), \qquad \sigma_r = T(1-\nu)\left(1 - \frac{2}{3-4\nu}\right).$$

At the edge of the hole on the vertical section,

$$\sigma_\theta = T\nu\left(1 + \frac{2}{3-4\nu}\right), \qquad \sigma_r = T(1-\nu)\left(1 + \frac{2}{3-4\nu}\right).$$

For an Araldite plate ($\nu = 0{\cdot}38$), these become:—

At the horizontal section

$$\sigma_\theta = -0{\cdot}13T,\ \sigma_r = -0{\cdot}22T,\ \tfrac{1}{2}(\sigma_\theta - \sigma_r) = 0{\cdot}045T.$$

At the vertical section

$$\sigma_\theta = 0{\cdot}89T,\ \sigma_r = 1{\cdot}46T,\ \tfrac{1}{2}(\sigma_\theta - \sigma_r) = -0{\cdot}285T.$$

The stresses at the horizontal section in a plate with a very high interference-fit pin might be expected to approach the values given by this solution, but the S.C.F.'s as given in Tables I-IV show that, even for the case of high interference and low load, the stresses, although small, are still considerably above these values.

On the vertical section the theoretical solution gives a positive S.C.F. for the tensile stress σ_θ, indicating that the boundary conditions there with the interference-fit pin are very different from the state of "fixation" assumed in the theory.

An Energy Approach to Climb Performance Estimation of a Turbo-Jet Transport Aircraft

RAMCHANDRA B. TAMBOLI

(*de Havilland Aircraft, Hatfield**)

SUMMARY: The climb performance of a turbo-jet transport aircraft is considered, using the concept of the energy height. The analytical formulae used in evaluating the time needed, distance covered and fuel consumed during climb under various conditions are developed. It is concluded that the application of this energy approach method to the climb performance estimation of a turbo-jet transport aircraft will prove satisfactory from the points of view both of the accuracy of the results and of saving some of the considerable time needed for the climb calculation by the conventional method. A numerical example is given to illustrate the usefulness, applicability and flexibility of this method.

1. Introduction

The operating data to be supplied with a transport aircraft in connection with the climb performance includes information on the fuel used, distance covered and time taken during the climbs to operating altitude. This information will be required to cover the appropriate ranges of those parameters which cause appreciable change in the quantities.

With a turbo-jet transport aircraft atmospheric temperature is of importance as well as take-off weight and it may be necessary to tabulate information in perhaps twenty to thirty different combinations of weight and temperature. The time taken to evaluate the climb performance under these various conditions by a conventional method (for example, Royal Aeronautical Society Performance Data Sheet EG3/1) is considerable.

The method described here was developed to expedite the climb calculation. It has also shown promise of application in other aspects of performance estimation, in particular the rapid evaluation of the effects on climb of the changes in any of the controlling parameters. It was found convenient to use the concept of the energy height throughout the work, thus following the practice established in Refs. 1, 2 and 3.

---

*Now with de Havilland Aircraft of Canada.

Originally received February 1955.

NOTATION

$a, a', a_1; b, b', b_1; c, c', c_1$
$d, d', d_1; k, k'; l, l'$
$A, A'; B, B'; C; E'; G, R$
} constants as defined in the text

b_w total span of wing (ft.)

e induced drag factor in $C_D = C_{Dz} + C_L^2/(\pi A_w e)$ (also referred to as aeroplane efficiency factor)

g acceleration due to gravity (ft./sec.^{2})

h average slope of the curve of climb speed (T.A.S.) against energy height (ft./sec./ft.)

h' average slope of the curve of climb speed (T.A.S.) against temperature (ft./sec./°C.)

m average slope of the curve of drag against energy height (lb./ft.)

m' average slope of the curve of drag against temperature (lb./°C.)

n average slope of the curve of net thrust against energy height (lb./ft.)

n' average slope of the curve of net thrust against temperature (lb./°C.)

q average slope of the curve of fuel flow against energy height (lb./sec./ft.)

q' average slope of the curve of fuel flow against temperature (lb./sec./°C.)

r average slope of the curve of weight of aircraft during climb against energy height (lb./ft.)

r' average slope of the curve of weight of aircraft during climb against temperature (lb./°C.)

t total time to climb to an energy height (sec.)

A_w aspect ratio (b_w^2/S_w)

C_{Dz} parasite drag coefficient of aircraft

C_L lift coefficient

D drag of aircraft (lb.)

F fuel flow (lb./sec.)

H geometric height of aircraft (ft.)

H_e energy height of aircraft $= H + V^2/(2g)$ (ft.)

H_{e0} datum energy height from which climb is commenced (ft.)

H_{eR} relative energy height with respect to H_{e0} (ft.)

H_p pressure altitude (ft.)

Q total fuel consumed in climb (lb.)

S total distance covered in climb (ft.)

S_w wing area (gross) (ft.^{2})

ΔT temperature in excess of or below I.S.A. (or an arbitrary reference temperature selected) (°C.)

V climb speed (T.A.S.) (ft./sec.)

W weight of the aircraft (lb.)

X net thrust delivered by the power plant of the aircraft (lb.)

γ angle of climb with reference to ground (radians)

ρ air density (slugs/ft.^{3})

Suffix "0" refers to conditions at the commencement of the climb

Abbreviations

E.A.S. equivalent airspeed

T.A.S. true airspeed

I.S.A. international standard atmosphere (I.C.A.N.)

2. The Fundamental Climb Equation

The fundamental climb equation may be obtained by writing down the equation of longitudinal motion of an aircraft climbing at an angle of γ in still air as

$$X - D - W \sin\gamma = \frac{W}{g}\frac{dV}{dt} \quad . \quad . \quad . \quad . \quad . \quad (1)$$

which may be written $$\frac{dH}{dt} = (X-D)\frac{V}{W} - \frac{V}{g}\frac{dV}{dt}. \quad . \quad . \quad . \quad . \quad (2)$$

The energy height is defined as $$H_e = H + \frac{V^2}{2g} \quad . \quad . \quad . \quad . \quad . \quad (3)$$

which, after differentiation with respect to time, becomes

$$\frac{dH_e}{dt} = \frac{dH}{dt} + \frac{V}{g}\frac{dV}{dt}. \quad . \quad . \quad . \quad . \quad (4)$$

Substituting equation (4) in equation (2) gives

$$\frac{dH_e}{dt} = (X-D)\frac{V}{W}. \quad . \quad . \quad . \quad . \quad (5)$$

Equation (5) is referred to in this paper as the energy form of the basic climb equation.

The application of this approach to the estimation of climb performance of a turbo-jet transport aircraft is described here in two parts, according to whether the variation of climb speed, thrust, drag, fuel flow and weight during climb can or cannot be assumed to be a linear function of energy height.

PART I

3. Leading Assumption

In general, for a particular aircraft and at a specified engine r.p.m., the climb speed (T.A.S.), thrust, drag, fuel flow and weight during climb can be expressed as some function of energy height. In Part I their variations with energy height are assumed to be linear or very close to linear.

In addition, the following particulars of the aircraft are assumed to be known:—

(*i*) Drag polar (drag characteristics).

(*ii*) Engine r.p.m. for climb condition.

(*iii*) Climb speed. (This may be obtained from the analysis of the optimum climb technique. In certain cases it may be dictated by the consideration of passenger comfort.)

Engine r.p.m. and climb speed are assumed to be independent of climb weight.

4. Method

The thrust and fuel flow under different temperature conditions for which the climb calculations are required can be evaluated and plotted against energy height and their variations with energy height determined.

The drag of the aircraft is a function of climb speed and climb weight, of which the former is known. The weight of the aircraft during climb is a function of the fuel flow and the rate of climb. The rate of climb, in its turn, depends on the weight of the aircraft during climb: this is a vicious circle. It is therefore suggested that, by using the formula given in Appendix I, first of all a variation of weight of the aircraft during climb with energy height should be established by calculating an average slope of the climb weight–energy height curve. It is then possible to establish the relationship of the drag of the aircraft with energy height based on varying weight in climb.

In short, for a particular aircraft it is possible to establish the relationships of the climb speed (T.A.S.), thrust, fuel flow, drag and weight during climb with energy height for different climb weights and temperature conditions.

5. General Case

5.1. The Basic Equations

Assuming that the thrust, fuel flow, climb speed, drag and weight during climb vary linearly with energy height and temperature:—

Thrust, $$X = X_0 + nH_{eR} + n'\Delta T \quad . \quad . \quad . \quad . \quad (6)$$

Fuel flow, $$F = F_0 + qH_{eR} + q'\Delta T \quad . \quad . \quad . \quad . \quad (7)$$

Climb speed (T.A.S.), $$V = V_0 + hH_{eR} + h'\Delta T \quad . \quad . \quad . \quad . \quad (8)$$

Drag, $$D = D_0 + mH_{eR} + m'\Delta T \quad . \quad . \quad . \quad . \quad (9)$$

Climb weight, $$W = W_0 + rH_{eR} + r'\Delta T \quad . \quad . \quad . \quad . \quad (10)$$

In these expressions X_0, F_0, V_0, D_0 and W_0 are the quantities at an arbitrary datum energy height, H_{e_0}, from which the climb is measured; n, q, h, m, r and n', q', h', m', r' are the slopes of the thrust, fuel flow, climb speed, drag and climb weight curves with energy height and with temperature respectively. ΔT is the temperature in °C. in excess of or below that of the International Standard Atmosphere (I.S.A.), (or an arbitrary reference temperature considered). For convenience the concept of the relative energy height, H_{eR}, is used throughout this paper. Thus H_{eR} is the energy height with reference to an arbitrary datum energy height, H_{e_0}, from which the climb is commenced ($H_{eR}=H_e-H_{e_0}$).

Using equations (6) to (10), equation (5) becomes

$$\frac{dH_{eR}}{dt}=(X-D)\,V/W$$

$$=\frac{\{(X_0+nH_{eR}+n'\Delta T)-(D_0+mH_{eR}+m'\Delta T)\}\,(V_0+hH_{eR}+h'\Delta T)}{W_0+rH_{eR}+r'\Delta T}$$

$$=\frac{a'H_{eR}^2+b'H_{eR}+c'}{W_0+rH_{eR}+r'\Delta T} \quad . \quad . \quad . \quad . \quad . \quad . \quad . \quad (11)$$

where $a'=h\,(n-m)$

$$b'=h\,(X_0-D_0)+(n-m)\,(V_0+h'\Delta T)+h\Delta T\,(n'-m')$$

$$c'=[(X_0-D_0)+\Delta T\,(n'-m')]\,(V_0+h'\Delta T).$$

5.2. Time Integral

The total time t required to climb from an arbitrary datum energy height, H_{e_0}, to any other energy height H_e is given by (using the concept of the relative energy height already explained)

$$t=\int_0^{H_{eR}}\frac{W_0+rH_{eR}+r'\Delta T}{a'H_{eR}^2+b'H_{eR}+c'}\,dH_{eR}. \quad . \quad . \quad . \quad . \quad (12)$$

The solution of this integral depends on whether

(*i*) $b'^2>4a'c'$

(*ii*) $b'^2<4a'c'$

or (*iii*) $b'^2=4a'c'$.

A study of equation (11) will lead to the following conclusions:—

constant c' is always positive (for climb $X_0>D_0$)

constant a' is negative as n is negative and usually greater than m in magnitude while h is positive

constant b' may be positive or negative.

Therefore $b'^2>4a'c'$ (in practical cases).

Hence the time integral becomes

$$t=\frac{W_0+r'\Delta T-rb'/(2a')}{d'}\left[\log_e\left(1+\frac{2a'}{b'-d'}H_{eR}\right)+\log_e\frac{1}{\left(1+\frac{2a'}{b'+d'}H_{eR}\right)}\right]+$$
$$+\frac{r}{2a'}\log_e\left(1+\frac{b'}{c'}H_{eR}+\frac{a'}{c'}H_{eR}^2\right) \quad . \quad . \quad (13)$$

where $d'=\sqrt{(b'^2-4a'c')}$.

5.3. Distance Integral

The total distance S covered during climb from an arbitrary datum energy height H_{e_0} to any other energy height H_e is given by

$$S=\int_0^{H_{eR}}\frac{W_0+rH_{eR}+r'\Delta T}{k'H_{eR}+l'}\,dH_{eR}$$
$$=\frac{k'(W_0+r'\Delta T)-rl'}{k'^2}\log_e\left(1+\frac{k'}{l'}H_{eR}\right)+\frac{r}{k'}H_{eR} \quad . \quad (14)$$

where $k'=n-m$

$l'=(X_0-D_0)+\Delta T(n'-m')$.

5.4. Fuel Integral

Likewise the total fuel Q consumed in climb from an arbitrary energy height H_{e_0} to any other energy height H_e is given by

$$Q=\int_0^{H_{eR}}\frac{(F_0+qH_{eR}+q'\Delta T)(W_0+rH_{eR}+r'\Delta T)}{a'H_{eR}^2+b'H_{eR}+c'}\,dH_{eR} \quad . \quad . \quad (15)$$

or $$Q=\left[A'-\frac{B'b'}{2a'}+\frac{E'(b'^2-2a'c')}{2a'^2}\right]\int_0^{H_{eR}}\frac{dH_{eR}}{a'H_{eR}^2+b'H_{eR}+c'}+$$
$$+\frac{a'B'-E'b'}{2a'^2}\log_e\left(1+\frac{b'}{c'}H_{eR}+\frac{a'}{c'}H_{eR}^2\right)+\frac{E'}{a'}H_{eR}. \quad . \quad (16)$$

where $A'=F_0W_0+\Delta T(q'W_0+F_0r'+q'r'\Delta T)$

$B'=(W_0q+F_0r)+\Delta T(q'r+r'q)$

$E'=rq$.

It may be noted that the integral part and the logarithmic term of equation (16) are already evaluated in the time integral; advantage should be taken of this while performing a numerical calculation for the fuel integral.

6. Special Cases

6.1. Case I (A): At Standard Temperature ($\Delta T=0$)

Under this condition equations (6) to (10) become

$$X=X_0+nH_{eR} \quad . \quad . \quad . \quad . \quad (17)$$

$$F=F_0+qH_{eR} \quad . \quad . \quad . \quad . \quad (18)$$

$$V=V_0+hH_{eR} \quad . \quad . \quad . \quad . \quad (19)$$

$$D=D_0+mH_{eR} \quad . \quad . \quad . \quad . \quad (20)$$

$$W=W_0+rH_{eR}. \quad . \quad . \quad . \quad . \quad (21)$$

Energy climb equation (5) becomes

$$\frac{dH_{eR}}{dt}=(X-D)V/W$$

$$=\frac{\{(X_0+nH_{eR})-(D_0+mH_{eR})\}(V_0+hH_{eR})}{W_0+rH_{eR}}$$

$$=\frac{aH_{eR}^2+bH_{eR}+c}{W_0+rH_{eR}} \quad . \quad . \quad . \quad . \quad . \quad . \quad . \quad . \quad . \quad (22)$$

where $a=a'=h(n-m)$

$$b=h(X_0-D_0)+V_0(n-m)$$

$$c=V_0(X_0-D_0).$$

The time needed, distance covered and fuel used in climb from an arbitrary energy height H_{e_0} to any other energy height H_e are evaluated as in the general case already discussed. The final results are

Time Integral

$$t=\frac{W_0-rb/(2a)}{d}\left[\log_e\left(1+\frac{2a}{b-d}H_{eR}\right)+\log_e\frac{1}{\left(1+\frac{2a}{b+d}H_{eR}\right)}\right]+$$

$$+\frac{r}{2a}\log_e\left(1+\frac{b}{c}H_{eR}+\frac{a}{c}H_{eR}^2\right). \quad . \quad (23)$$

where $d=\sqrt{(b^2-4ac)}$.

Distance Integral

$$S=\frac{kW_0-rl}{k^2}\log_e\left(1+\frac{k}{l}H_{eR}\right)+\frac{r}{k}H_{eR} \quad . \quad . \quad . \quad (24)$$

where $k=k'=n-m$

$l=X_0-D_0$.

Fuel Integral

$$Q=\left[F_0W_0-\frac{b(W_0q+F_0r)}{2a}+\frac{rq(b^2-2ac)}{2a^2}\right]\int_0^{H_{eR}}\frac{dH_{eR}}{aH_{eR}^2+bH_{eR}+c}+$$

$$+\left(\frac{W_0q+F_0r}{2a}-\frac{rbq}{2a^2}\right)\log_e\left(1+\frac{b}{c}H_{eR}+\frac{a}{c}H_{eR}^2\right)+\frac{rq}{a}H_{eR} \quad . \quad (25)$$

Once again the integral part and the logarithmic term of equation (25) will have been evaluated in the time integral; advantage should be taken of this while performing the numerical calculation for the fuel integral.

6.2. Case I (B): Constant Climb Weight ($dW/dH_{eR}=r=0$)

Further, if the weight of an aircraft during climb is assumed constant (and equal to either the weight at the commencement of climb or an average weight during climb), that is, $dW/dH_{eR}=r=0$, the time, distance and fuel integrals become as follows:—

Time Integral, from equation (23),

$$t=\frac{W_0}{d}\left[\log_e\left(1+\frac{2a}{b-d}H_{eR}\right)+\log_e\frac{1}{\left(1+\frac{2a}{b+d}H_{eR}\right)}\right]. \quad . \quad (26)$$

Distance Integral, from equation (24),

$$S=\frac{W_0}{k}\log_e\left(1+\frac{k}{l}H_{eR}\right). \quad . \quad . \quad . \quad . \quad (27)$$

Fuel integral, from equation (25),

$$Q=\left(F_0W_0-\frac{W_0bq}{2a}\right)\int_0^{H_{eR}}\frac{dH_{eR}}{aH_{eR}^2+bH_{eR}+c}+\frac{W_0q}{2a}\log_e\left(1+\frac{b}{c}H_{eR}+\frac{a}{c}H_{eR}^2\right). \quad (28)$$

6.3. Case II

A particular case with the following assumptions is now considered:—

(*i*) standard reference temperature ($\Delta T = 0$),

(*ii*) climb speed : constant E.A.S.

(*iii*) constant engine r.p.m.

(*iv*) climb weight constant during climb (*see* note below).

By virtue of these assumptions the forms of equations (17) to (19) remain unaffected, while equations (20) and (21) become

$D = D_0$ (constant, neglecting Reynolds number and compressibility effects)

$W = W_0$ (constant).

Energy climb equation (5) becomes

$$\frac{dH_{eR}}{dt} = (X - D)\,V/W = \frac{(X_0 + nH_{eR} - D_0)(V_0 + hH_{eR})}{W_0}$$

$$= \frac{a_1 H_{eR}^2 + b_1 H_{eR} + c_1}{W_0},$$

where $a_1 = nh$

$b_1 = nV_0 + h(X_0 - D_0)$

$c_1 = c = (X_0 - D_0)\,V_0$.

Time Integral

$$t = \int_0^{H_{eR}} \frac{W_0}{a_1 H_{eR}^2 + b_1 H_{eR} + c_1}\, dH_{eR}$$

$$t = \frac{W_0}{d_1}\left[\log_e\left(1 + \frac{2a_1}{b_1 - d_1} H_{eR}\right) + \log_e \frac{1}{\left(1 + \frac{2a_1}{b_1 + d_1} H_{eR}\right)}\right] \quad . \quad (29)$$

where $d_1 = \sqrt{(b_1^2 - 4a_1c_1)}$.

Distance Integral

$$S = \int_0^{H_{eR}} \frac{W_0}{X_0 - D_0 + nH_{eR}}\, dH_{eR}$$

$$S = \frac{W_0}{n} \log_e\left(1 + \frac{n}{X_0 - D_0} H_{eR}\right) \quad . \quad . \quad . \quad (30)$$

Fuel Integral

$$Q=\int_0^{H_{eR}} \frac{W_0(F_0+qH_{eR})}{a_1H_{eR}^2+b_1H_{eR}+c_1}\,dH_{eR}$$

$$Q=\left(F_0W_0-\frac{W_0qb_1}{2a_1}\right)\int_0^{H_{eR}} \frac{dH_{eR}}{a_1H_{eR}^2+b_1H_{eR}+c_1}+\frac{W_0q}{2a_1}\log_e\left(1+\frac{b_1}{c_1}H_{eR}+\frac{a_1}{c_1}H_{eR}^2\right) \quad . \quad . \quad . \quad . \quad (31)$$

The integral part of equation (31) will have been evaluated in the time integral.

Note: If a variation of climb weight with energy height is assumed, then the drag, which is a function of weight, will also vary with energy height. Case II then becomes identical with Case I (A) already discussed.

6.4. Case III

Another particular case with the following assumptions is considered:—

(*i*) standard reference temperature ($\Delta T=0$),

(*ii*) constant engine r.p.m.

(*iii*) climb speed : constant T.A.S.

(*iv*) climb weight is assumed to vary with energy height. (Expressions for constant weight will be derived as corollaries).

By virtue of these assumptions the forms of equations (17), (18), (20) and (21) remain unaffected while equation (19) becomes

$$V=V_0 \text{ (constant)}.$$

Energy climb equation (5) becomes

$$\frac{dH_{eR}}{dt}=(X-D)V/W=\frac{\{(X_0+nH_{eR})-(D_0+mH_{eR})\}V_0}{W_0+rH_{eR}}.$$

Time Integral

$$t=\int_0^{H_{eR}} \frac{W_0+rH_{eR}}{V_0[(X_0-D_0)+H_{eR}(n-m)]}\,dH_{eR}$$

$$t=\frac{W_0(n-m)-r(X_0-D_0)}{V_0(n-m)^2}\log_e\left[1+\frac{n-m}{X_0-D_0}H_{eR}\right]+\frac{r}{V_0(n-m)}H_{eR}. \quad (32)$$

If the weight is assumed constant during climb ($r=0$), then

$$t=\frac{W_0}{V_0(n-m)}\log_e\left[1+\frac{n-m}{X_0-D_0}H_{eR}\right]. \quad . \quad . \quad . \quad (32a)$$

Distance Integral

$$S=V_0\int_0^{H_{eR}}\frac{(W_0+rH_{eR})}{[(X_0-D_0)+(n-m)H_{eR}]V_0}\,dH_{eR}$$

$$S=V_0\,[\text{time integral (32)}]. \quad . \quad . \quad . \quad . \quad . \quad . \quad (33)$$

For constant weight during climb ($r=0$),

$$S=V_0\,[\text{time integral (32}a\text{)}]. \quad . \quad . \quad . \quad (33a)$$

Fuel Integral

$$Q=\int_0^{H_{eR}}\frac{(F_0+qH_{eR})(W_0+rH_{eR})}{V_0\{(X_0-D_0)+(n-m)H_{eR}\}}\,dH_{eR}. \quad . \quad . \quad (34)$$

For constant weight during climb,

$$Q=\int_0^{H_{eR}}\frac{(F_0+qH_{eR})W_0}{V_0\{(X_0-D_0)+(n-m)H_{eR}\}}\,dH_{eR}. \quad . \quad . \quad . \quad (34a)$$

Both equations (34) and (34*a*) can be evaluated in the usual way.

PART II

In those cases where the main assumptions in Part I, namely, that the variations of thrust, climb speed, fuel flow and drag are linear with energy height, are found hard to justify, the following approach is suggested.

7. Method

Where the climb calculations are required for various climb weights and temperature conditions by using the method described in Part II, it is advisable to select a reference climb weight and temperature such that they lie roughly in the middle of the range of the climb weights and temperatures for which the calculations are required. For example, if it is expected to perform the climb calculations for a climb weight bracket from 80,000 lb. to 120,000 lb. and a temperature bracket from I.S.A. to I.S.A.+30°C., then the reference climb weight and temperature should be 100,000 lb. and I.S.A.+15°C. respectively.

The calculations should then be made for $(X-D)V/W$ for the reference climb weight and temperature selected as just mentioned, and plotted against energy height. Such a plot may be linear or very close to linear up to an energy height at which $(X-D)V/W$ is about 300 or 400 ft./min., in which case, for practical purposes, a straight line may be drawn through these points and the relation may be expressed as

$$(X-D)V/W = C + BH_{eR} \quad . \quad . \quad . \quad . \quad . \quad (35)$$

where B and C are constants.

The time integral then becomes

$$t = \int_0^{H_{eR}} \frac{dH_{eR}}{C + BH_{eR}} . \quad . \quad . \quad . \quad . \quad . \quad (36)$$

As in Part I the concept of the relative energy height is used. Integral (36) can be evaluated in the usual way.

When a plot of $(X-D)V/W$ against energy height for a reference climb weight and temperature is not linear, as assumed in equation (35), the relationship could be expressed as

$$(X-D)V/W = aH_{eR}^2 + bH_{eR} + c \quad . \quad . \quad . \quad . \quad (37)$$

where a, b and c are constants. The constants a and b can be determined by differentiating equation (37) with respect to energy height.

The time integral becomes

$$t = \int_0^{H_{eR}} \frac{dH_{eR}}{aH_{eR}^2 + bH_{eR} + c} . \quad . \quad . \quad . \quad (38)$$

Integral (38) may be evaluated in the same manner as equation (12) in Part I.

The distance and fuel integrals in both these cases may then be evaluated either mathematically, as has been done in Part I if fuel flow and climb speed can be expressed approximately as linear functions of energy height; otherwise graphically, as in the conventional method.

Once the constants a, b, c or B and C are determined for a reference climb weight and temperature then the effect of a change of climb weight and/or temperature from the reference case on these constants can be evaluated approximately by the formulae given in Appendix I. Thus, once a relationship between $(X-D)V/W$ and energy height is established in the form of either equation (35) or (37) for a reference climb weight and temperature, a similar relationship for other climb weights and/or temperature conditions can be established in the same form without any further calculations for $(X-D)V/W$ for those particular cases. The time, distance and fuel integrals can be evaluated as already discussed.

8. Discussion

In equations (6) to (10) the constants n, q, h, m and r which are slopes of thrust, fuel flow, climb speed (T.A.S.), drag and climb weight curves with energy height are assumed to be independent of temperature. Similarly the constants n', q', h', m' and r' which are slopes of the thrust, fuel flow, climb speed, drag and climb weight curves with temperature are assumed to be independent of energy height. These criteria will not rigorously be met in practice. However, if the variations of these slopes are not appreciable, a mean value may be assumed in the calculations.

For better accuracy, however, a slightly different procedure described under Case I (A) may be followed. That is to say, all the five equations from (17) to (21) should be established for different climb weights and temperature conditions to be considered. Then by using the appropriate formulae the time, distance and fuel integrals should be evaluated.

Where there is a change of slope of speed or thrust or fuel flow curve with energy height the method could be applied in two stages. For example, it may be desirable for a turbo-jet aircraft to make a climb at certain speed and engine r.p.m. up to a certain altitude and then change the climb speed and/or engine setting. This change in climb technique at certain altitude, demanded by certain reasons, will cause changes in the slopes of the curves of speed, thrust and fuel flow against energy height above that particular altitude. In these circumstances it is desirable to evaluate the time, distance and fuel integrals in two stages.

The accuracy of the results by this energy method depends entirely on the degree with which the basic assumption of linear variation of thrust, fuel flow, speed and drag with energy height is met. It is therefore mandatory that the variation of thrust, fuel flow, climb speed and drag (based on constant weight for this purpose) with energy height should be examined before a calculation is undertaken. The degree of deviation of these quantities from the linear assumption will give an approximate idea of discrepancy between the estimated results and those which may be expected from flight tests.

Good approximate results with some saving in time required for climb calculations may be obtained by using a constant climb weight (an average weight during climb).

Moderately satisfactory results may be obtained by using the method described in Part II. This method is simpler and quicker inasmuch as it is necessary to establish a relationship of $(X-D)V/W$ against energy height only for a reference climb weight and temperature, in the form of either equation (35) or (37). Then that form of equation can be extended to other weights and/or temperature conditions without actually doing the calculations for and making a plot of $(X-D)V/W$ against energy height for those particular conditions. Once again the degree of accuracy of the results will depend on the degree with which the assumptions made in deriving equations (47), (49), (50), (51), and so on, in

Appendix I are met. By virtue of the approximations and assumptions made in deriving equation (35) or equations (47), (49), and so on, just mentioned, a high degree of accuracy of the results should not be expected. Nevertheless this method will give satisfactory results with considerable saving in the time required for climb calculations.

9. Conclusions

As a result of the investigations carried out in developing and applying the energy approach method described in this paper to the climb performance estimation of a civil turbo-jet transport aircraft, the following conclusions are drawn.

(*i*) The application of the energy approach method to the climb performance estimation of a turbo-jet transport aircraft for various climb weights and temperature conditions will prove satisfactory from the points of view both of the accuracy of the results and of saving some of the considerable time needed for such calculations by the conventional method.

Some idea of the time saved by this method during the calculations of a group of three different climb weights and temperature conditions can be obtained from the following table, which is based on the author's experience.

Conventional method		*Energy approach method*		
		Part I		*Part II*
3	:	2	:	1

However, if the climb calculation is desired for only one climb weight and temperature condition, then there is very little to choose between the energy approach method and the conventional method. The conventional method in this case is quite satisfactory.

(*ii*) The energy approach method will prove useful both in the preliminary design stages and in the development stages of a turbo-jet transport aircraft as a quick means of studying the effects of small changes in one or more of the controlling parameters of climb performance, such as thrust, drag characteristics, and so on, on the climb performance of an aircraft under various climb conditions.

(*iii*) The method developed in Part II is simpler and quicker than that in Part I; as a result its application will save still more of the time required for such a calculation.

(*iv*) The operational and development sections of the airlines should also benefit by this method.

(*v*) It is thought that the application of this method to the descent performance estimation, as well as to the calculation of the drift-down after an engine failure, will also prove satisfactory.

ACKNOWLEDGMENTS

The author wishes to thank the de Havilland Aircraft Company for permission to publish this paper, and also acknowledges gratefully the valuable advice and comments rendered by Mr. D. R. Newman, of the same firm, in the preparation of this paper. The opinions expressed are those of the author.

REFERENCES

1. RUTOWSKI, E. S. Energy Approach to General Aircraft Performance Problems. *Journal of the Aeronautical Sciences*, Vol. 21, No. 3, pp. 187-195, March 1954.

2. KELLY, L. Optimum Climb Technique for a Jet Propelled Aircraft. The College of Aeronautics, Cranfield, Report No. 57, April 1952.

3. LUSH, K. J. A Review of the Problem of Choosing a Climb Technique With Proposals for a New Climb Technique for High Performance Aircraft. R. & M. 2557, 1951.

Appendix I

1. EFFECT ON THE SLOPE OF THE CURVE OF CLIMB WEIGHT AGAINST ENERGY HEIGHT OF A CHANGE IN (*a*) CLIMB WEIGHT AND (*b*) TEMPERATURE

(*a*) At I.S.A. conditions (or at the reference temperature considered, that is at $\Delta T=0$) the relation between the weight in climb and energy height can be expressed approximately as

$$W=W_0+rH_{eR}. \quad . \quad . \quad . \quad . \quad . \quad . \quad (39)$$

The decrease in weight during climb is equal to the fuel consumed in climb.

$$dQ=-dW=-F\times\Delta t$$

$$=-\frac{F\times dH_{eR}}{(X-D)\,V/W}. \quad . \quad . \quad . \quad . \quad (40)$$

Therefore

$$r=-\frac{dW}{dH_{eR}}=-\frac{F}{(X-D)\,V/W} \quad . \quad . \quad . \quad . \quad (41)$$

where F = mean fuel flow

Δt = time to climb energy height, dH_{eR}

$(X-D)\,V/W$ = mean rate of climb during height, dH_{eR}.

By equation (41), r is a function of fuel flow and rate of climb, which in turn are functions of energy height. For a first approximation an average value of r may be evaluated at 67 per cent of the expected cruise height at a reference climb weight.

The drag during climb, which depends on the weight, may be evaluated by successive approximations at the same height at which r is to be evaluated. In practice two successive approximations are found to be satisfactory. As thrust, fuel flow and climb speed, by assumption, are independent of climb weight, r could be evaluated by using equation (41) for different climb weights.

So that equation (41) may be written as

$$r = -\left[\frac{F}{(X-D)\,V/W}\right]_{67 \text{ per cent cruise height}} \quad . \quad . \quad . \quad (42)$$

That is, F, X, D and V are to be evaluated at 67 per cent of the expected cruise height at a reference climb weight.

(*b*) Temperature effect, like weight effect on r, may be evaluated in a similar manner, so that

$$r = -\left[\frac{F}{(X-D)\,V/W}\right]_{67 \text{ per cent cruise height}} \quad . \quad . \quad . \quad . \quad (43)$$

where F, X, D and V are evaluated under appropriate temperature conditions at 67 per cent of the expected cruise height.

2. Effect of a Change in Climb Weight on Constants a, b, c, B and C in Equations (35) and (37) at I.S.A. Conditions (or at Reference Temperature Considered)

For the purpose of calculating the effects of change in climb weight and temperature on the constants a, b, c, B and C in equations (35) and (37) the following simplifications and approximations are made:—

(*i*) The thrust and climb speed (T.A.S.) are approximately linear with energy height. (If however thrust and climb speed are expressed as some other convenient function of energy height, a similar treatment on the lines mentioned in what follows can easily be developed for those cases).

(*ii*) The weight of the aircraft during climb is held constant.

By virtue of these assumptions and approximations, equations (17) to (21) in the main text can be used. The basic expression for $(X-D)\,V/W$ then becomes

$$(X-D)\frac{V}{W} = \frac{1}{W}\{V_0\,(X_0 - D_0) + H_{eR}\,[V_0\,(n-m) + h\,(X_0 - D_0)] + hH_{eR}^2\,(n-m)\}. \quad (44)$$

Constants C in equation (35) and c in equation (37) are given by

$$C, c = (X_0 - D_0)\,V_0/W \quad . \quad . \quad . \quad . \quad . \quad . \quad (45)$$

and B in equation (35) is given by

$$B = \frac{d}{dH_{eR}}\left[(X-D)\frac{V}{W}\right] = \frac{1}{W}\,[V_0\,(n-m) + h\,(X_0 - D_0) + 2hH_{eR}\,(n-m)]. \quad (46)$$

Assuming m to be constant with weight and

$$D_0 \simeq \tfrac{1}{2} C_{D_2} \rho V^2 S_w + \frac{W^2}{b_w^2 \pi e \tfrac{1}{2}\rho V^2}$$

$$= G + RW^2,$$

where $\quad G = C_{D_2} \tfrac{1}{2}\rho V^2 S_w, \qquad R = \dfrac{1}{b_w^2 \pi e \tfrac{1}{2}\rho V^2},$

equation (46) becomes

$$B=\frac{1}{W}\{(V_0+2hH_{eR})(n-m)+h(X_0-G-RW^2)\}. \quad . \quad . \quad (46a)$$

The effect of change of weight on the constant B can be evaluated by differentiating equation (46*a*) with respect to weight.

Thus $$\frac{d}{dW}(B)=-\left(2hR+\frac{B}{W}\right) \quad . \quad . \quad . \quad . \quad . \quad (47)$$

Equation (44) may be rearranged as follows:—

$$(X-D)\frac{V}{W}=aH_{eR}^2+bH_{eR}+c \quad . \quad . \quad . \quad . \quad . \quad (48)$$

where $$a=\frac{h(n-m)}{W}$$

$$b=\frac{V_0(n-m)+h(X_0-D_0)}{W}$$

$$c=\frac{V_0(X_0-D_0)}{W}.$$

Equation (48) is the same as equation (37).

The effect of change of weight on constants a, b and c in equation (48) may be evaluated by differentiating these constants with respect to weight.

Thus $$\frac{d}{dW}(a)=-\frac{a}{W} \quad . \quad . \quad . \quad . \quad . \quad . \quad . \quad (49)$$

$$\frac{d}{dW}(b)=-\left(2hR+\frac{b}{W}\right) \quad . \quad . \quad . \quad . \quad . \quad (50)$$

$$\frac{d}{dW}(c)=-\left(2V_0R+\frac{c}{W}\right). \quad . \quad . \quad . \quad . \quad (51)$$

Equations (47), (49), (50) and (51) are obviously valid for assessing the effect of only small changes in climb weight of the aircraft. For large variation in climb weight, however, the modified formulae given in what follows should be used.

Let W_1 be a reference weight and $W_2=W_1+\Delta W$, where ΔW is 5 per cent or more of the reference weight. From equation (46*a*)

$$B_1-B_2=dB=-(W_1-W_2)\left\{\frac{B_1}{W_2}+Rh\left(1+\frac{W_1}{W_2}\right)\right\}. \quad . \quad . \quad (52)$$

A similar approach will modify equations (49), (50) and (51) to

$$a_1 - a_2 = da = -(W_1 - W_2)\frac{a_1}{W_2} \quad . \quad . \quad . \quad . \quad . \quad . \quad . \quad . \quad (53)$$

$$b_1 - b_2 = db = -(W_1 - W_2)\left\{\frac{b_1}{W_2} + hR\left(1 + \frac{W_1}{W_2}\right)\right\} \quad . \quad . \quad . \quad (54)$$

$$c_1 - c_2 = dc = -(W_1 - W_2)\left\{\frac{c_1}{W_2} + RV_0\left(1 + \frac{W_1}{W_2}\right)\right\} . \quad . \quad . \quad (55)$$

3. Effect of Change in Temperature on Constants a, b, c, B and C in Equations (35) and (37) at Constant Weight

By virtue of the assumptions and approximations made in the previous section, equations (6) to (9) in the main text can be used. Thus the basic expression for $(X-D)V/W$ becomes

$$(X-D)\frac{V}{W} = \frac{1}{W}\left\{(X_0 + n'\Delta T - D_0 - m'\Delta T)(V_0 + h'\Delta T) + H_{eR}\left[(n-m)(V_0 + h'\Delta T) + \right.\right.$$

$$\left.\left. + h(X_0 + n'\Delta T - D_0 - m'\Delta T)\right] + hH_{eR}^2(n-m)\right\} . \quad . \quad (56)$$

Differentiating equation (56) with respect to H_{eR}, the constant B in equation (35) is obtained as

$$\frac{d}{dH_{eR}}\left[(X-D)\frac{V}{W}\right] = B = \frac{1}{W}\left\{(n-m)(V_0 + 2hH_{eR}) + \right.$$

$$\left. + h(X_0 - D_0) + \Delta T[h'(n-m) + h(n'-m')]\right\} . \quad (57)$$

As ΔT is a relative temperature with respect to the I.S.A. conditions or the reference temperature considered, the difference in the value of B_1 (say) at the I.S.A. condition (or at the reference temperature) and B_2 (say) at a temperature which is equal to I.S.A. (or the reference temperature) $\pm\Delta T°C$ is obviously given from equation (57) as

$$B_1 - B_2 = dB = \pm\Delta T\left\{\frac{1}{W}[h'(n-m) + h(n'-m')]\right\} . \quad . \quad . \quad (58)$$

At the I.S.A. conditions (or at the reference temperature), that is $\Delta T = 0$, $dB = 0$.

Now equation (56) could be rearranged as

$$(X-D)\frac{V}{W} = aH_{eR}^2 + bH_{eR} + c \quad . \quad . \quad . \quad . \quad . \quad (59)$$

where $a = \dfrac{h(n-m)}{W}$

$$b = \frac{1}{W}\left\{V_0(n-m) + h(X_0 - D_0) + \Delta T[h'(n-m) + h(n'-m')]\right\}$$

$$c = \frac{1}{W}\left\{(X_0 - D_0)V_0 + \Delta T[V_0(n'-m') + h'(X_0 - D_0)] + \Delta T^2 h'(n'-m')\right\} .$$

Equation (59) is the same as equation (37).

The difference between a_1, b_1 and c_1 (say) at the I.S.A. condition (or at the reference temperature) and a_2, b_2 and c_2 (say) at a temperature which is equal to the I.S.A. (or the reference temperature) $\pm\Delta T$°C is obtained from equation (59) as follows:—

$$a_1 - a_2 = da = 0 \quad . \quad . \quad . \quad . \quad . \quad . \quad . \quad . \quad . \quad . \quad . \quad . \quad . \quad (60)$$

$$b_1 - b_2 = db = \pm\Delta T \left\{ \frac{1}{W} [h'(n-m) + h(n'-m')] \right\} \quad . \quad . \quad . \quad . \quad . \quad (61)$$

$$c_1 - c_2 = dc = \pm \frac{1}{W} \left\{ \Delta T [V_0 (n'-m') + h'(X_0 - D_0)] + h'\Delta T^2 (n'-m') \right\} \quad . \quad (62)$$

If the constants h, n and m are not independent of temperature, the constants a, b, c, B and C ought to be determined for each temperature condition to be considered. If, however, h, n and m are very nearly independent of temperature (this will be the case for a small variation of temperature from the reference case), then equations (58), (60), (61) and (62) may be used to evaluate an effect of change in temperature on a, b, c, B and C.

m' in equations (58), (61) and (62) is usually very small in comparison with n' and hence may be neglected.

Appendix II

Illustrative Example

For a turbo-jet transport it is required to estimate the time needed, distance covered and fuel consumed in a climb from 5,000 ft. to 35,000 ft. pressure altitude under the following conditions:—

(*i*) climb speed: constant E.A.S.; 260 m.p.h.

(*ii*) engine speed: maximum continuous r.p.m.

(*iii*) climb weight: 80,000 lb., 100,000 lb. and 120,000 lb. at I.S.A. + 10°C.

and (*iv*) at temperature I.S.A. − 5°C. and I.S.A. + 25°C. for 100,000 lb.

The reference climb weight and temperature in this case are 100,000 lb. and I.S.A. + 10°C. respectively. It is thus intended to cover a climb weight bracket of 20 per cent of the reference weight and the temperature bracket is equal to the reference temperature ± 15°C.

From the calculations and plots of thrust, fuel flow and climb speed (T.A.S.) against energy height under the temperature conditions just mentioned, the constants in equations (17), (18) and (19) are determined by assuming a linear relationship of those quantities with energy height. (*See* Table I.)

Using equations (42) and (43), first the average values of the slope r of the curve of climb weight against energy height were determined and then the average values of the slope m of the curve of drag against energy height were established. The results of the calculations are given in Table II.

TABLE I

CONSTANTS IN EQUATIONS (17), (18), (19)

	Climb speed		*Net thrust*		*Fuel flow*	
	V_0 (ft./sec.)	h $\left(\frac{\text{ft./sec.}}{\text{ft.}}\right)$	X_0 (lb.)	n (lb./ft.)	F_0 (lb./sec.)	q $\left(\frac{\text{lb./sec.}}{\text{ft.}}\right)$
I.S.A.−5°C.	396	$8{\cdot}10\times10^{-3}$	$17{\cdot}8\times10^{3}$	$-0{\cdot}255$	4·550	$-7{\cdot}41\times10^{-5}$
I.S.A.+10°C.	408	$7{\cdot}89\times10^{-3}$	$15{\cdot}5\times10^{3}$	$-0{\cdot}200$	4·085	$-6{\cdot}40\times10^{-5}$
I.S.A.+25°C.	418	$7{\cdot}55\times10^{-3}$	$13{\cdot}9\times10^{3}$	$-0{\cdot}173$	3·700	$-5{\cdot}75\times10^{-5}$

V_0, X_0 and F_0 correspond to 5,000 ft. (H_p) from which the climb is commenced.

TABLE II

VALUES OF r IN $W=W_0+rH_{eR}$; AND m IN $D=D_0+mH_{eR}$

I.S.A.+10°C.			
Climb weight: lb.	80,000	100,000	120,000
r : lb./ft.	$-0{\cdot}063$	$-0{\cdot}087$	$-0{\cdot}121$
m: lb./ft.	$-1{\cdot}54\times10^{-3}$	$-2{\cdot}65\times10^{-3}$	$-4{\cdot}4\times10^{-3}$
100,000 lb.			
Temperature	I.S.A.−5°C.	I.S.A.+10°C.	I.S.A.+25°C.
r : lb./ft.	$-0{\cdot}8$	$-0{\cdot}087$	$-0{\cdot}102$
m: lb./ft.	$-2{\cdot}44\times10^{-3}$	$-2{\cdot}65\times10^{-3}$	$-3{\cdot}1\times10^{-3}$

Part I. Having thus established all the constants in equations from (17) to (21), the time, distance and fuel integrals were evaluated by using equations (23), (24) and (25) respectively. The results of the calculations are presented in Table IV.

Part II. The actual plot of $(X-D)V/W$ against energy height at the reference weight and temperature (100,000 lb. and I.S.A.+10°C.) was not quite linear, but an approximate linear relationship was assumed so that

$$(X-D)\frac{V}{W}=C+BH_{eR}$$

where $C=42{\cdot}7$ ft./sec.

$B=-6{\cdot}47\times10^{-4}$ ft./sec./ft.

Constant C here is not the actual value of $(X-D)V/W$ when $H_{eR}=0$, but an intercept on the ordinate of the curve of $(X-D)V/W$ against H_{eR}, assumed a straight line.

The effect of the change in weight from 100,000 lb. to 80,000 lb. and 120,000 lb. on the values of the constants B and C was calculated by using equations (52) and (55).

The temperature effect on the value of B was evaluated by making a straightforward calculation using equation (57) at a mean energy height, as equation (58) could not be used because h, n and m are not independent of temperature (*see* Table I).

As C in this case is an intercept on the ordinate of the curve of $(X-D)V/W$ against energy height, it was corrected for different temperature by using equation (62).

The values of B and C are collected in Table III.

TABLE III

VALUES OF B AND C IN $(X-D)V/W=C+BH_{eR}$

I.S.A.+10°C.			
Climb weight: lb.	80,000	100,000	120,000
B: $\frac{\text{ft./sec.}}{\text{ft.}}$	$-7{\cdot}51\times10^{-4}$	$-6{\cdot}47\times10^{-4}$	$-5{\cdot}85\times10^{-4}$
C: ft./sec.	56·2	42·7	33·2
100,000 lb.			
Temperature	I.S.A.−5°C.	I.S.A.+10°C.	I.S.A.+25°C.
B: $\frac{\text{ft./sec.}}{\text{ft.}}$	$-5{\cdot}96\times10^{-4}$	$-6{\cdot}47\times10^{-4}$	$-4{\cdot}96\times10^{-4}$
C: ft./sec.	49·4	42·7	35·5

Using the values of B and C given in Table III the time, distance and fuel integrals were evaluated and the final results of the calculations are presented in Table IV.

For convenience the final results of the calculations for time are given in minutes instead of seconds and for distance in statute miles instead of feet.

SUMMARY OF THE RESULTS

The results of the climb calculations in terms of the time needed, distance covered, fuel consumed and air miles per pound of fuel in climb from 5,000 ft. to 35,000 ft. pressure altitude, in the illustrative example, are summarised in Table IV.

TABLE IV

I.S.A.+10°C.						
Initial climb weight: lb.	80,000		100,000		120,000	
	By method in Part I	*By method in Part II*	*By method in Part I*	*By method in Part II*	*By method in Part I*	*By method in Part II*
Time: min.	14·75	14·75	20·6	20·6	28·8	28·8
Distance: statute miles	96	95	133	134	189	187
Fuel: lb.	2,480	2,470	3,430	3,424	4,790	4,738
Air miles per lb. of fuel × 10^2	3·87	3·85	3·88	3·91	3·95	3·95
100,000 lb.						
Temperature	I.S.A.−5°C.		I.S.A.+10°C.		I.S.A.+25°C.	
Time: min.	15·2	14·35	20·6	20·6	29·75	26·5
Distance: statute miles	95	89·4	133	134	195·5	178·5
Fuel: lb.	2,872	2,825	3,430	3,424	4,220	3,935
Air miles per lb. of fuel × 10^2	3·31	3·17	3·88	3·91	4·62	4·54

Comments on the Results

The method described in Part II of the paper, in spite of its approximate nature, gives results in this case which are satisfactory when compared with the results obtained by the method described in Part I. The maximum discrepancy between the results of the two methods occurs for a weight of 100,000 lb. with I.S.A. + 25°C, where it is about 8·7 per cent in distance covered and about 6·7 per cent in fuel used during climb. It is interesting to note that the discrepancy in the results obtained by the two methods, whatever its magnitude may be, is of the same sign both for the distance covered and fuel consumed during climb. For this reason the air miles per pound of fuel during climb are about the same by both the methods. The discrepancy in the air miles per pound of fuel during climb in the case given (I.S.A. + 25°C) is only 1·7 per cent, the maximum being 4·2 per cent at I.S.A. – 5°C.

The comparison which was made separately of the results of calculations by these two methods with those obtained by the conventional method has also shown the same tendency for fuel and distance discrepancy of the same sign.

The Natural Frequencies of Thin Skew Plates

R. K. KAUL and V. CADAMBE

(*National Physical Laboratory of India*)

SUMMARY: Using Rayleigh's principle, the natural frequencies of thin isotropic rhombic plates, with three possible combinations of boundary conditions obtained by combining clamped-clamped and clamped-supported edge conditions, are determined in Part I of this paper. To introduce constant limits of integration, non-orthogonal co-ordinate systems are used and the wave shape for the vibrating plate is approximated by using normal functions representing mode shapes of corresponding bars. To estimate the accuracy of these eigenvalues, Kato's theorem is used and the lower bounds for the natural frequencies are determined in Part II of the paper. It is also shown that normal beam functions are not generally suitable for the determination of eigenfrequencies of skew plates with large skew angles.

1. Introduction

The study of natural inextensional vibrations of thin oblique plates, with particular reference to the determination of eigenfrequencies and mode shapes, is a problem of considerable interest. Other methods are available but Rayleigh's minimal principle[1] finds great favour in spite of certain limitations. One of the difficulties is the suitable selection of a minimising sequence and therefore quite often, to get a closer approximation to the natural frequencies, it it necessary to resort to the " device of variable parameters " apparently due to Rayleigh, although sometimes attributed to Ritz[2].

Rayleigh's energy principles shows that first order errors in the tentative mode of vibration produce only second order effects in the estimate of natural frequency and, since it is not possible to admit all possible functions, the Rayleigh's ratio is therefore no longer the exact solution λ_r^2 but only a close *upper bound* to the natural frequency. In a number of cases this principle leads to surprisingly close results; but, in cases where exact values of the frequencies cannot be calculated, a

Received July 1955.

criterion is needed to judge the accuracy of the results obtained. The only justification is then to calculate the close *lower bounds* to the natural frequencies, a knowledge of which would be as useful, for practical purposes, as an exact value of the frequency.

By using a condition of " weak minimum ", Weinstein[3] has shown how lower bounds to a clamped plate problem can be obtained. But recently Kato in a singularly simple and elegant theorem gave a method, which applies not merely to fundamental mode, but to any overtone of a vibrating system with any number of degrees of freedom, finite or infinite. Temple[4] (1952) extended Kato's theorem to vibrating systems with both elastic and inertial coupling and further obtained generalisations of his results.

In Part I of this paper, using Rayleigh's principle, approximate frequency equations are derived and eigenvalues determined for three different boundary conditions of skew plates when vibrating in modes of the type m/n and $(m/n \pm n/m)$. In Part II, Kato's theorem is used for determining the close lower bounds for which the upper bounds are provided by Rayleigh's principle.

Notation

V_w reduced elastic strain energy of the bending of the plate

T_w reduced kinetic energy of the plate vibrating harmonically

E, ν Young's modulus and Poisson's ratio of the plate material respectively

D_0 flexural stiffness, $Eh^3/\{12(1-\nu^2)\}$

x, y / ξ, ζ rectangular and oblique co-ordinates, respectively

σ_0 constant mass per unit area of the plate of uniform thickness h

ω natural circular frequency, $2\pi f$

λ_r^2 exact eigenfrequency, $\omega^2(\sigma_0/D_0)\cos^4\alpha$

ρ_R^2 Rayleigh's ratio

$\Phi_m(\xi), \Psi_n(\zeta)$ normed-orthogonal bar eigenfunctions representing normal modes of vibration of a uniform bar

δ_{mn} Kronecker's delta $\begin{cases} =0, \text{ for } m \neq n \\ =1, \text{ for } m = n \end{cases}$

ε_0^2 measure of accuracy

R residual inertial force

A, B symbols used in Kato's lemma

α^2, β^2 two eigenvalues defined in Part II

PART I

ON THE CALCULATION OF UPPER BOUNDS TO NATURAL FREQUENCIES

2. Basic Theory

The equation of motion of a thin isotropic plate is governed by the fourth order partial differential equation

$$D_0\Delta^4 w_0+\sigma_0\frac{\partial^2 w_0}{\partial t^2}=0 \text{ in domain D} \quad . \quad . \quad . \quad (1)$$

where w_0 is the displacement at any point (x, y) at time t. It is assumed that the motion is simple harmonic and therefore

$$w_0=w\sin(\omega t+\delta),$$

where w satisfies the boundary conditions of the plate. The formal approach to the problem consists in selecting for w a double infinite series, each term of which satisfies equation (1) and some of the boundary conditions. Then, by judiciously combining an infinite number of these, the remaining boundary conditions can be satisfied. This procedure, first adopted by Taylor[5] in the analysis of statical problems of buckling of a clamped rectangular plate, was later used by Tomotika[6] for a similar problem in vibrations of plates. The procedure leads to an infinite determinant, the roots of which give the natural frequencies. Normally, by taking a few rows and columns, the roots converge, but the process is fairly laborious.

Using Rayleigh's minimal principle the natural frequencies of a vibrating system can be quite closely estimated. If the *reduced* potential and kinetic energies of a continuous system be represented by V_w and T_w, then Rayleigh's principle states that for a tentative mode w, $\rho_R^2=V_w/T_w$ is stationary, *i.e.* first order errors in the tentative mode produce only second order effects in the frequency. When no exact solution can be found, w can be approximated in the form

$$w=\alpha_1 w_1+\alpha_2 w_2+\alpha_3 w_3+\ldots\ldots+\alpha_n w_n,$$

in which w_k satisfies the artificial boundary constraints of the problem and the constant co-ordinates α_k are to be so adjusted as to render V_w/T_w a minimum. Differentiating with respect to these arbitrary parameters and equating to zero, the general frequency equation is

$$\frac{\partial\rho_R^2}{\partial\alpha_k}=\frac{\partial}{\partial\alpha_k}\{V_w-\rho_R^2 T_w\}=0 \quad . \quad . \quad . \quad . \quad (2)$$

For thin plates the quadratic functionals V_w and T_w are defined by the following bi-linear expressions:—

$$\left.\begin{aligned} V_w &= \int\int \left[(\nabla^2 w)^2 - 2(1-\nu)\left\{\frac{\partial^2 w}{\partial x^2}\,\frac{\partial^2 w}{\partial y^2} - \left(\frac{\partial^2 w}{\partial x \partial y}\right)^2\right\}\right] dx\,dy \\ \text{and} \quad T_w &= \int\int w^2\,dx\,dy \end{aligned}\right\} \quad . \qquad (3)$$

For plates of polygonal shapes, when w vanishes on the boundary, it can be shown that

$$\int\int \left\{\frac{\partial^2 w}{\partial x^2}\,\frac{\partial^2 w}{\partial y^2} - \left(\frac{\partial^2 w}{\partial x \partial y}\right)^2\right\} dx\,dy = 0,$$

and therefore

$$V_w = \int\int (\nabla^2 w)^2\,dx\,dy.$$

Hence the eigenfrequencies for such plates are given by the simpler equations

$$\frac{\partial}{\partial \alpha_k}\int\int \{(\nabla^2 w)^2 - \rho_R{}^2 w^2\}\,dx\,dy = 0 \quad . \quad . \quad . \quad . \qquad (4)$$

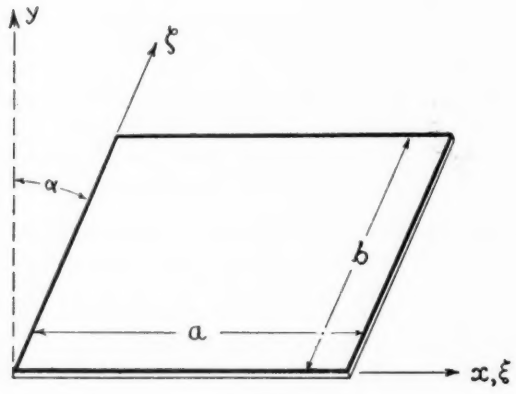

Fig. 1.

Thin plate of oblique plan form.

For a plate of oblique plan form, as shown in Fig. 1, the co-ordinate transformation relations are

$$\xi = x - y \tan \alpha$$

$$\zeta = y \sec \alpha,$$

and therefore $$\frac{\partial}{\partial x}=\frac{\partial}{\partial \xi}\,, \qquad \frac{\partial}{\partial y}=\sec\alpha\left\{\frac{\partial}{\partial \zeta}-\sin\alpha\frac{\partial}{\partial \xi}\right\},$$

and Jacobian $$J\left(\frac{x,\ y}{\xi,\ \zeta}\right)=\cos\alpha.$$

Therefore the equivalent frequency equations in terms of the skew co-ordinate system (ξ, ζ) are

$$\frac{\partial}{\partial \alpha_k}\int\int\left[\left\{\frac{\partial^2 w}{\partial \xi^2}+2\frac{\partial^2 w}{\partial \xi\,\partial \zeta}\sin\alpha+\frac{\partial^2 w}{\partial \zeta^2}\right\}^2-\rho_R{}^2 w^2\right]d\xi\,d\zeta=0, \quad . \qquad (5)$$

where $$\rho_R{}^2=\omega^2\frac{\sigma_0}{D_0}\cos^4\alpha.$$

This leads to a system of n simultaneous linear homogeneous equations in n coefficients and the eigenvalues $\rho_{Rn}{}^2$. For a non-trivial solution to exist it is necessary that the determinant of the system of equations be zero; the successive roots in the ascending order $\rho_{R1}{}^2 \leqslant \rho_{R2}{}^2 \leqslant \rho_{R3}{}^2 \leqslant \ldots\ldots, \leqslant \rho_{Rn}{}^2$ are the discrete eigenvalues of the continuous system. Since in the selection of an assumed form for a corresponding mode of vibration all possible modes are not admitted, the estimate of eigenvalue on the basis of the stationary property will always err on the side of excess, and therefore Rayleigh's ratio $\rho_R{}^2 \geqslant \lambda^2$. The order by which Rayleigh's estimate approximates the exact frequency depends however on the selection of the plate deflection function and the closeness with which it represents the actual wave form. Though it is possible to improve the approximation and refine the method into a rapidly convergent procedure, the detail of the numerical computation increases inordinately with each improvement of approximation and therefore becomes more and more laborious.

3. Bar Eigenfunctions

For the skew plate with edges parallel to ξ and ζ co-ordinates, the series approximation for the plate deflection w *is* taken in the form

$$w=\sum_m^r\sum_n^s \alpha_{mn}\,\Phi_m(\xi)\,\Psi_n(\zeta),$$

where α_{mn} are the arbitrary parameters consistent with the required normalisation condition, and $\Phi_m(\xi)$ and $\Psi_n(\zeta)$ are sets of " admissible " functions. These functions admissible for competition must explicitly satisfy the *" artificial boundary conditions "*, since fixed boundary values of these functions, or their first derivatives which imply slope, correspond to rigid constraints on the boundary of the plate. On the other hand, *natural boundary conditions* need not be stipulated in advance, as these

express the equilibrium of the plate along the boundary, and are implied in the variational problem[7]. In the present case a very good approximation to the admissible set of deflection functions is the choice of eigenfunctions defining normal modes of vibrations of corresponding bars and which satisfy the required boundary conditions. These *normed*-orthogonal bar eigenfunctions are:—

(*i*) *Clamped-clamped bar*

$$\Phi_m(\xi)=\frac{1}{\sqrt{a}}\left\{\frac{\sin\{k_m(\xi-a/2)\}}{\sin(k_ma/2)}-\frac{\sinh\{k_m(\xi-a/2)\}}{\sinh(k_ma/2)}\right\}\cos^2\frac{m\pi}{2}+$$

$$+\frac{1}{\sqrt{a}}\left\{\frac{\cos\{k_m(\xi-a/2)\}}{\cos(k_ma/2)}-\frac{\cosh\{k_m(\xi-a/2)\}}{\cosh(k_ma/2)}\right\}\sin^2\frac{m\pi}{2}$$

$$\text{for } m=1, 2, 3, \ldots\ldots, r, \quad . \quad . \quad . \quad . \quad (6)$$

where k_ma is the m^{th} positive root of the transcendental equation

$$\tan(k_ma/2)=(-1)^m\tanh(k_ma/2)$$

or its equivalent $\qquad \cosh k_ma=\sec k_ma.$

(*ii*) *Clamped-supported bar*

$$\Phi_m(\xi)=\frac{1}{\sqrt{a}}\left\{\frac{\sin\{k_m(\xi-a)\}}{\cos k_ma}-\frac{\sinh\{k_m(\xi-a)\}}{\cosh k_ma}\right\} \quad . \quad . \quad (7)$$

$$\text{for } m=1, 2, 3, \ldots\ldots, r,$$

where k_ma is the m^{th} root of the transcendental equation

$$\tan k_ma=\tanh k_ma.$$

The functions are not only continuously differentiable in the range $0\leqq\xi\leqq a$ but also satisfy the homogeneous differential equation

$$\frac{\partial^4\Phi_m(\xi)}{\partial\xi^4}-k_m{}^4\Phi_m(\xi)=0 \quad . \quad . \quad . \quad . \quad . \quad (8)$$

and the terminal conditions of corresponding uniform bars vibrating harmonically. Further the set of functions selected are normed-orthogonal within the range of integration and satisfy the condition

$$\int_0^a \Phi_r(\xi)\,\Phi_s(\xi)\,d\xi=\delta_{rs},$$

where δ_{rs} is the Kronecker's delta.

The second derivatives of these functions are also orthogonal and satisfy the relations

$$\int_0^a \Phi_r''(\xi)\,\Phi_s''(\xi)\,d\xi = k_r^4 \delta_{rs},$$

where k,a is the r^{th} bar eigenvalue. These ortho-normal bar eigenfunctions, in addition to the usual properties of Fourier series also possess the property

$$\int_0^a \Phi_r(\xi)\,\Phi_s''(\xi)\,d\xi = -\int_0^a \Phi_r'(\xi)\,\Phi_s'(\xi)\,d\xi.$$

Similar properties also hold good for the function $\Psi_n(\zeta)$.

4. Approximate Frequency Equation (Rayleigh's)

Using Rayleigh's principle, the tentative shape for the type mode m/n is taken in the simplest form

$$w = \Phi_m(\xi)\,\Psi_n(\zeta) \quad . \quad . \quad . \quad . \quad . \quad (9)$$

where $\Phi_m(\xi)$ and $\Psi_n(\zeta)$ are the m^{th} and n^{th} eigenfunctions of corresponding bars in the ξ – and ζ – directions. On substituting for w in the frequency equation (5) and using the properties of the normed-orthogonal functions described earlier, the following equation for the Rayleigh's ratio is obtained

$$\rho_R^2 = \frac{1}{a^2b^2}\left\{\frac{b^2}{a^2}(k_m a)^4 + \frac{a^2}{b^2}(k_n b)^4 + \right.$$

$$\left. + 2a^2b^2(1+2\sin^2\alpha)\int_0^a\int_0^b \Phi_m(\xi)\,\Phi_m''(\xi)\,\Psi_n(\zeta)\,\Psi_n''(\zeta)\,d\xi d\zeta\right\} . \quad . \quad (10)$$

Besides modes of the type m/n, *i.e.* m half-waves along the ξ – direction and n half-waves along the ζ – direction, the nodal patterns of which are lines parallel to the co-ordinate directions, there also exist normal modes of the type $(m/n \pm n/m)$ when the frequencies of the modes m/n and n/m are identical. The nodal patterns for these are formed from the simultaneous existence of two component vibrations m/n and n/m at a point and the resultant amplitude is governed by their in-phase or out-of-phase relationship. The two new modes $(m/n \pm n/m)$ have two discrete eigenfrequencies and the nodal patterns are also discrete. If the wave form for such a mode is represented by

$$w = \{\Phi_m(\xi)\,\Psi_n(\zeta) \pm \Phi_n(\xi)\,\Psi_m(\zeta)\} \quad . \quad . \quad . \quad . \quad (11)$$

then the eigenfrequency ρ_R^2 for the distinctly discrete set $(m/n \pm n/m)$ is given by

$$\rho_R^2 = \frac{1}{2a^2b^2}\Big[\frac{b^2}{a^2}\{(p_m a)^4 + (p_n a)^4\} + \frac{a^2}{b^2}\{(q_m b)^4 + (q_n b)^4\} + \\ + 2a^2b^2(1 + 2\sin^2\alpha)\int_0^a\int_0^b \{\Phi_m(\xi)\Phi_m''(\xi)\Psi_n(\zeta)\Psi_n''(\zeta) + \\ + \Phi_n(\xi)\Phi_n''(\xi)\Psi_m(\zeta)\Psi_m''(\zeta) \pm 2\Phi_m(\xi)\Phi_n''(\xi)\Psi_m(\zeta)\Psi_n''(\zeta)\}\, d\xi d\zeta\Big] \quad . \quad (12)$$

Expressions for the various definite integrals which occur in the frequency equations are given in the Appendix.

(*a*) *Oblique plate clamped on all edges*

For clamped-clamped skew plates, the same bar eigenfunction (6) is used along the two co-ordinate directions. In the frequency equation (12) the integral

$$I_{mn''} = \int_0^a \Phi_m(\xi)\Phi_n''(\xi)\, d\xi \quad \text{or} \quad J_{mn''} = \int_0^b \Psi_m(\zeta)\Psi_n''(\zeta)\, d\zeta$$

is zero when $(m+n)$ is odd, and therefore in this case discrete modes of the type $(m/n \pm n/m)$ exist only for those combinations when $(m-n) = \pm 2, \pm 4, \pm 6, \ldots\ldots$. For other combinations of m and n, only modes of the type m/n exist, the eigenfrequencies of which are given by equation (10). For a square plate or when the skew angle is small ($\alpha \leqslant 15°$), the nodal patterns corresponding to modes m/n are straight lines parallel to the edges of the plate. But for modes of the type $(m/n \pm n/m)$ it is not so and the amplitude of any point, depending upon the phase relationship, is the sum or difference of the amplitudes of that point for the component vibrations m/n and n/m.

(*b*) *Oblique plate clamped on three edges and supported on the fourth*

Both eigenfunctions (6) and (7) are necessary in this case to represent the plate deflection wave form. The function $\Phi_m(\xi)$ represents the deflection of the plate in the clamped-clamped direction and the function $\Psi_n(\zeta)$ in the clamped-supported direction. Although in the frequency equation (12) the integral $I_{mn''}J_{mn''}$ has definite positive values for those combinations of m and n when $(m-n) = \pm 2, \pm 4, \ldots\ldots$ associated modes of the type of $(m/n \pm n/m)$ cannot exist, since for this unsymmetrical set of boundary conditions the eigenfrequencies of modes m/n and n/m are different. Therefore for all combinations of m and n, only modes of the type m/n will exist.

(*c*) *Oblique plate with two adjacent edges clamped and the other two freely supported*

The clamped-supported bar eigenfunction (7) is used to represent the deflection of the plate in this case. The integral $I_{mn''}$ or $J_{mn''}$ has a definite value for every

TABLE I

FREQUENCY FACTOR FOR SKEW PLATES (RAYLEIGH'S)*

$$\rho_R = \omega \left\{ \frac{\sigma_0}{D_0} \right\}^{\frac{1}{2}} \cos^2\alpha$$

(a) *Clamped-clamped plate*

	1/1	1/2	2/2	1/3−3/1	1/3+3/1	3/2	3/3	2/4−4/2	2/4+4/2
0°	36·108 68	73·737 20	108·849 92	131·766 43	133·195 89	165·922 64	220·906 26	242·824 25	245·228 91
15°	36·665 95	74·759 47	111·429 44	132·902 44	133·707 92	169·560 38	226·761 35	246·907 61	249·665 88
30°	38·146 97	77·483 62	118·190 16	135·957 65	138·031 24	179·122 58	242·036 64	258·015 03	261·404 20
45°	40·081 73	81·057 07	126·844 50	140·023 54	142·702 83	191·414 41	261·464 90	272·359 86	276·635 31

(b) *Clamped on three edges and supported on the fourth*

	1/1	1/2	2/1	2/2	1/3	3/1	2/3	3/2	3/3
0°	31·953 69	63·659 44	71·425 74	101·256 02	116·969 91	130·837 68	152·748 15	159·998 16	209·968 42
15°	32·541 06	64·760 57	72·397 74	103·827 18	118·287 59	132·034 25	156·500 28	163·512 17	215·821 39
30°	34·094 21	67·677 63	75·038 74	110·581 01	121·814 89	135·111 34	166·320 28	172·748 55	231·057 35
45°	36·108 06	71·470 26	78·458 77	119·178 60	126·474 41	139·253 90	178·865 52	184·620 44	250·373 73

(c) *Clamped on two adjacent edges and supported on the other two*

	1/1	1/2−2/1	1/2+2/1	2/2	1/3−3/1	1/3+3/1	2/3−3/2	2/3+3/2	3/3
0°	27·194 78	60·690 28	61·292 75	93·129 78	115·055 20	115·306 00	145·977 78	146·813 03	198·547 91
15°	27·837 75	61·729 39	62·400 77	95·740 32	116·290 09	116·571 44	149·579 42	150·503 59	204·427 91
30°	29·523 10	64·481 47	65·330 68	102·534 13	119·598 90	119·960 65	159·003 87	160·153 25	219·691 44
45°	31·680 75	68·061 82	69·133 17	111·145 57	124·441 33	124·441 33	171·040 79	172·464 67	238·971 51

* Common constant multiplier $(1/a^2)$.

combination of m and n, ($m \neq n$). Further the boundary conditions are symmetrical along the diagonal of the plate and therefore eigenfrequencies of modes m/n and n/m will be identical, in which case compounding of modes will take place, leading to discrete modes ($m/n \pm n/m$). In this particular case the eigenfrequencies of the two associated modes ($m/n \pm n/m$) are very nearly equal. This is because the contribution of the integral $I_{mn''}J_{mn''}$ in the frequency equation (12) is very small. Thus, if the mode is wrongly assumed to be pure m/n and the effect of n/m is neglected, the error introduced in the results will be negligible.

For each of the three sets of boundary conditions just discussed, Rayleigh's ratio is calculated for both modes of the type m/n and ($m/n \pm n/m$). Plates having skew angles of 0°, 15°, 30° and 45° and lateral dimensions ($a \times a$) are considered and the successive eigenvalues in the ascending order

$$\rho_{R1} \leqslant \rho_{R2} \leqslant \rho_{R3} \leqslant \ldots\ldots \leqslant \rho_{Rn}$$

are given in Table I.

PART II

ON THE CALCULATION OF LOWER BOUNDS TO NATURAL FREQUENCIES

5. Basic Theory

From a practical standpoint (when an amount of uncertainty is involved in the physical data) it is essential to know the margin by which the frequencies err on the side of over-estimation. Rayleigh's principle therefore suffers from a serious drawback in that it provides only an upper estimate for the frequencies. Rayleigh himself has given two "Comparison Theorems" which provide the lower estimate, but with far less accuracy than his energy method provides the upper bounds. The singularly simple theorem of Kato answers the requirement in that it provides really close lower bounds to the natural frequencies. The original results of Kato are restricted to systems with no inertial coupling and do not apply to general Lagrangian systems. These were recently extended by Temple[4] to systems with both elastic and inertial coupling and are used here in the determination of lower bounds for the natural frequencies of skew plates for which the upper estimate (in Part I) is based on Rayleigh's principle. The theory of the principle is taken *mutatis mutandis* from Ref. 4 and therefore only portions relevant to the problem under consideration are discussed here.

Let α^2 and β^2 be two eigenvalues corresponding to two distinct normal modes of vibrations (which by convention are normed), and selected such that

$$\alpha^2 < \rho_R{}^2 < \beta^2,$$

while no eigenvalue $\lambda_r{}^2$ of the system lies in the interval

$$\alpha^2 < \lambda_r{}^2 < \beta^2.$$

To maintain oscillations in the trial mode w for which the approximate eigenvalue is ρ_R^2, a residual frictionless force R will come into play and therefore, for the trial mode w,

$$R = \nabla^4 w - \rho_R^2 w . \quad . \quad . \quad . \quad . \quad . \quad (13)$$

Similarly, if the residual forces corresponding to two eigenvalues α^2 and β^2 be A and B, then

$$\begin{aligned}(A \,.\, B) &= (\nabla^4 w - \alpha^2 w)(\nabla^4 w - \beta^2 w) \\ &= \{R + (\rho_R^2 - \alpha^2)\, w\}\ \{R + (\rho_R^2 - \beta^2)\, w\}\end{aligned}$$

and since external forces are supposed to do no work on the system, we have

$$(A \,.\, B) = R \,.\, R + (\rho_R^2 - \alpha^2)(\rho_R^2 - \beta^2)\, w \,.\, w \quad . \quad . \quad . \quad (14)$$

Further, in accordance with Kato's lemma, by using the theory of normal modes and principal co-ordinates, it can be shown that

$$K_w \equiv (A \,.\, B) = \Sigma \alpha_r^2 (\lambda_r^2 - \alpha^2)(\lambda_r^2 - \beta^2). \quad . \quad . \quad . \quad (15)$$

But α^2 and β^2 have been chosen so that no eigenvalue λ_r^2 lies in the interval

$$\alpha^2 < \lambda_r^2 < \beta^2.$$

Therefore $(\lambda_r^2 - \alpha^2)$ and $(\lambda_r^2 - \beta^2)$ will always have the same sign, making

$$K_w \equiv (A \,.\, B) \geqslant 0.$$

Hence, *a fortiori*, from equation (14),

$$(\rho_R^2 - \alpha^2)(\beta^2 - \rho_R^2) \leqslant \varepsilon_0^2,$$

where $$\varepsilon_0^2 = (R \,.\, R)/(w \,.\, w),$$

and in rectangular co-ordinates

$$\varepsilon_0^2 = \frac{\int_0^a \int_0^b (\nabla^4 w - \rho_R^2 w)^2 \, dx \, dy}{\int_0^a \int_0^b w^2 \, dx \, dy} \quad . \quad . \quad . \quad (16)$$

In applying this principle for determining the lower bounds to an eigenvalue λ_1^2 (say), for which the close upper bound is $\rho_{R1}^2 \geqslant \lambda_1^2$, we take $\alpha^2 = \lambda_1^2$ and $\beta^2 = \mu^2$ where μ^2 is the smallest eigenvalue greater than λ_1^2 and a lower estimate to λ_2^2.

Although such a choice implies multiplicity of λ_1^2, at the same time it fulfils the basic condition of Kato's lemma that no eigenvalue λ_r^2 lies in the interval $\alpha^2 < \lambda_r^2 < \beta^2$. Since $\rho_{R_1}^2 \geqslant \lambda_1^2$, we have

$$\left\{ \rho_R^2 - \frac{\varepsilon_0^2}{(\beta^2 - \rho_R^2)} \right\} \leqslant \alpha^2,$$

and therefore the bounds to λ_1^2 are given by the "bracket"

$$\left\{ \rho_R^2 - \frac{\varepsilon_0^2}{(\beta^2 - \rho_R^2)} \right\} \leqslant \lambda_1^2 \leqslant \rho_R^2 \quad . \quad . \quad . \quad . \quad (17)$$

6. Application to Skew Plates

In the skew co-ordinate system, the equation of motion of a thin plate, corresponding to equation (1), is

$$\nabla^2 \left\{ \nabla^2 w - 4 \sin \alpha \frac{\partial^2 w}{\partial \xi \partial \zeta} \right\} + 4 \sin^2 \alpha \frac{\partial^4 w}{\partial \xi^2 \partial \zeta^2} - \lambda_r^2 w = 0 \quad . \quad . \quad (18)$$

where $\nabla^2 = \left(\frac{\partial^2}{\partial \xi^2} + \frac{\partial^2}{\partial \zeta^2} \right)$ and $\lambda_r^2 = \omega^2 \frac{\sigma_0}{D_0} \cos^4 \alpha.$

For Rayleigh's ratio ρ_R^2, determined on the basis of an assumed mode shape, the measure of accuracy is

$$\varepsilon_0^2 = \frac{\int_0^a \int_0^b \left[\nabla^2 \left\{ \nabla^2 w - 4 \sin \alpha \frac{\partial^2 w}{\partial \xi \partial \zeta} \right\} + 4 \sin^2 \alpha \frac{\partial^4 w}{\partial \xi^2 \partial \zeta^2} - \rho_R^2 w \right]^2 d\xi d\zeta}{\int_0^a \int_0^b w^2 d\xi d\zeta} \quad . \quad (19)$$

For the type mode m/n, we take the simplest approximation (equation (9)) for the mode shape and, since $\Phi_m(\xi)$ and $\Psi_n(\zeta)$ are normed-orthogonal functions, we have, on substituting in equation (19),

$$\begin{aligned} \varepsilon_0^2 = {} & (k_m^4 + k_n^4)(k_m^4 + k_n^4 - 2\rho_R^2) + \rho_R^4 + 4\{(1 + 2\sin^2\alpha)^2 + 8\sin^2\alpha\} k_m^4 k_n^4 + \\ & + 4(1 + 2\sin^2\alpha)(k_m^4 + k_n^4 - \rho_R^2) \int_0^a \int_0^b \Phi_m(\xi) \Phi_m''(\xi) \Psi_n(\zeta) \Psi_n''(\zeta) \, d\xi d\zeta + \\ & + 16 \sin^2 \alpha \int_0^a \int_0^b \{\Phi_m'(\xi) \Phi_m'(\xi) \Psi_n'''(\zeta) \Psi_n'''(\zeta) + \Phi_m'''(\xi) \Phi_m'''(\xi) \Psi_n'(\zeta) \Psi_n'(\zeta)\} \, d\xi d\zeta \end{aligned}$$

. . . . . (20)

where, using the terminal conditions, the transformations are

$$\int_0^a \Phi_m'(\xi)\,\Phi_m'(\xi)\,d\xi = -\int_0^a \Phi_m(\xi)\,\Phi_m''(\xi)\,d\xi$$

and

$$\int_0^a \Phi_m''''(\xi)\,\Phi_m''''(\xi)\,d\xi = \left[\Phi_m''(\xi)\,\Phi_m'''(\xi)\right]_0^a - k_m^4 \int_0^a \Phi_m(\xi)\,\Phi_m''(\xi)\,d\xi$$

for clamped-clamped and clamped-supported functions.

Equation (20) holds good for the general case of oblique plates with skew angle α, vibrating in mode m/n. When the plate vibrates in an associated mode $(m/n \pm n/m)$, the simplest approximation for the mode shape is taken in the form

$$w = \{\Phi_m(\xi)\,\Psi_n(\zeta) \pm \Phi_n(\xi)\,\Psi_m(\zeta)\}.$$

Substituting for w in equation (19), the measure of accuracy for the particular case of a square plate is

$$\varepsilon_0^2 = (k_m^4 + k_n^4)(k_m^4 + k_n^4 - 2\rho_R^2) + 4k_m^4 k_n^4 + \rho_R^4 + 4(k_m^4 + k_n^4 - \rho_R^2)\{I_{mm''}\,J_{nn''} \pm I_{mn''}\,J_{mn''}\} \quad . \quad . \quad (21)$$

where

$$I_{mm''} = \int_0^a \Phi_m(x)\,\Phi_m''(x)\,dx, \qquad I_{mn''} = \int_0^a \Phi_m(x)\,\Phi_n''(x)\,dx$$

$$J_{nn''} = \int_0^b \Psi_n(y)\,\Psi_n''(y)\,dy, \qquad J_{mn''} = \int_0^b \Psi_m(y)\,\Psi_n''(y)\,dy.$$

Corresponding expressions for ε_0^2 can similarly be worked out when the trial mode is made up of a number of vector components with arbitrary parameters α_k. For determining the lower bounds, it is now only necessary to know β^2 (a lower estimate to the next higher eigenvalue λ_r^2). This can be calculated by using Rayleigh's Comparison Theorem[8], and for a continuous system typified by

$$R = \lambda_r^2\,Tw - Vw$$

(where V and T denote the bounded operators which specify the potential and kinetic energies) it is given by the smallest of the quotients $\{Vw/Tw\}$, for a *necessarily* positive product $(w.\,Tw)$. As an alternative, Rayleigh's ratio ρ_R^2 for the next eigenvalue may be used as an approximation. Kato's inequality (17) now yields the lower bounds.

7. Comparative Results and Discussion

On the basis of the theory developed in the previous section, lower bounds to the eigenvalues of a skew plate are determined, for which the upper estimate on the basis of the Rayleigh's principle is obtained in Part I. Taking simplest tentative modes, the measure of accuracy is calculated in each case from equations (20) or

TABLE II

LIMITING BOUNDS OF RHOMBIC SKEW PLATES*

$$\rho_K = \left\{ \rho_R^2 - \frac{\epsilon_0^2}{(\beta^2 - \rho_R^2)} \right\}^{\frac{1}{2}}, \text{ Kato's lower bound.}$$

$$\rho_R = \omega \left\{ \frac{\sigma_0}{D_0} \right\}^{\frac{1}{2}} \cos^2\alpha, \quad \text{Rayleigh's upper bound.}$$

Skew angle	*Mode type*	*Lower and upper bounds* $\rho_K \leqq \lambda_r \leqq \rho_R$		*Mean value*	*Percentage deviation from mean*
		(*a*) *Clamped-clamped skew plate*			
0°	1/1	35·33322	36·10868	35·72095	1·074
	1/2	71·76754	73·73720	72·75237	1·328
	2/2	104·98783	108·84992	106·91886	1·774
15°	1/1	34·69011	36·66593	35·67802	2·694
	1/2	63·68607	74·75947	69·22277	7·406
30°	1/1	32·95941	38·14697	35·55319	6·799
45°	1/1	30·63837	40·08173	35·36005	11·360
		(*b*) *Clamped on three edges and supported on the fourth*			
0°	1/1	31·46043	31·95364	31·70704	0·772
	1/2	62·22732	63·65944	62·94338	1·125
15°	1/1	31·46798	32·54105	32·00451	1·649
	1/2	60·88146	64·76057	62·82102	2·995
30°	1/1	30·35069	34·09421	32·22245	5·490
45°	1/1	29·46388	36·10806	32·78597	9·200
		(*c*) *Clamped on two adjacent edges and supported on the other two*			
0°	1/1	26·22513	27·19478	26·70995	1·783
	1/2–2/1	59·40657	60·69028	60·04842	1·057
15°	1/1	24·91261	27·83775	26·37517	5·254
30°	1/1	21·45018	29·52310	25·48664	13·672

* Common constant multiplier $(1/a^2)$.

(21) and, for the next eigenvalue β^2, Rayleigh's ratio ρ_R^2 is used. Values of the beam functions for different normal modes are obtained from tables of Characteristics Functions compiled by Young and Felgar[9], and values of definite integrals are given in the Appendix.

In Table II the lower and upper bounds are given for the first few mode shapes of skew plates for the three different sets of boundary conditions. The mean value is shown, and the percentage difference of the upper estimate from the mean.

From the estimate of the lower limits it is apparent that with square plates very close bounds for the first few eigenvalues can be obtained by using only one term in the series representation of plate deflection. The " brackets " in this case are very narrow and the results so obtained should for all practical purposes be equal to an exact solution. With skew plates such a simple approximation is not quite adequate and it becomes necessary to use more terms in the plate deflection series with increase in the order of the mode and the skew angle. For plates satisfying boundary conditions $w=0$ on the edges and having skew angles less than 30°, closer brackets to the natural frequencies can be obtained by using two or three terms in the series. But for angles greater than 30°, the estimates obtained are very poor; the widening of the inequality brackets is due to the fact that for higher skew angles the beam functions do not form a rapidly converging set. It is therefore necessary that, for large skew angles, either many more terms are used in the series representation of plate deflection, in which case the numerical computation becomes very laborious, or, if orthodox analysis permits, a more suitable function may be sought.

ACKNOWLEDGMENT

The work described in this paper forms part of the research programme of the National Physical Laboratory of India and is published by permission of the Director.

Appendix

TABLE OF DEFINITE INTEGRALS

The definite integrals which enter in the calculations are listed here.

(*i*) *Clamped-clamped beam*

$$\int_0^a \Phi_m(\xi)\,\Phi_n''(\xi)\,d\xi = -\int_0^a \Phi_m'(\xi)\,\Phi_n'(\xi)\,d\xi$$

$$= 0 \qquad (m+n \text{ odd})$$

$$= \frac{8\,k_m^2\,k_n^2}{a^2\,(k_n^4 - k_m^4)}\left\{k_n a \cot(k_n a/2) - k_m a \cot(k_m a/2)\right\} \qquad (m, n \text{ even})$$

$$= \frac{8\,k_m^2\,k_n^2}{a^2\,(k_n^4 - k_m^4)}\left\{k_m a \tan(k_m a/2) - k_n a \tan(k_n a/2)\right\} \qquad (m, n \text{ odd})$$

$$= \frac{1}{a^2}\left\{2\,k_m a \cot(k_m a/2) - \{k_m a \cot(k_m a/2)\}^2\right\} \qquad (m \text{ even})$$

$$= -\frac{1}{a^2}\left\{\{k_m a \tan(k_m a/2)\}^2 + 2k_m a \tan(k_m a/2)\right\} \qquad (m \text{ odd})$$

where $k_m a$ is the m^{th} positive root of the transcendental equation $\tan(k_m a/2) = (-1)^m \tanh(k_m a/2)$ or of its equivalent $\cosh k_m a = \sec k_m a$.

(ii) Clamped-supported beam

$$\int_0^a \Phi_m(\xi)\,\Phi_n''(\xi)\,d\xi = -\int_0^a \Phi_m'(\xi)\,\Phi_n'(\xi)\,d\xi$$

$$= \frac{4\,k_m^2\,k_n^2}{a^2\,(k_m^4 - k_n^4)}\left\{k_m a \tan k_n a - k_n a \tan k_m a\right\} \quad . \quad . \quad (m \neq n)$$

$$= \frac{1}{a^2}\left\{k_m a \tan k_m a - (k_m a)^2\right\} \quad . \quad . \quad . \quad . \quad . \quad . \quad (m = n)$$

where $k_m a$ is the m^{th} positive root of the transcendental equation $\tan k_m a = \tanh k_m a$.

REFERENCES

1. RAYLEIGH, LORD. *Theory of Sound*, Second Edition, Macmillan, 1894. Dover Publications, New York, pp. 109-13, 1945.
2. RITZ, W. Über eine neue Method zur Lösung gewissen Variations-Probleme der mathematische Physik. *Zeitschrift für reine und angewandte Mathematik*, Vol. 135, pp. 1-61, 1909.
3. WEINSTEIN, A. Etude des spectres des équations aux dérivées partielles de la théorie des plaques élastiques. *Mémorial des Sciences Mathematiques*, No. 88, 1937.
4. TEMPLE, G. The Accuracy of Rayleigh's Method of Calculating the Natural Frequencies of Vibrating Systems. *Proc. Roy Soc.*, A, Vol. 211, pp. 204-24, 1952.
5. TAYLOR, G. I. The Buckling Load for a Rectangular Plate with Four Clamped Edges. *Zeitschrift für angewandte Mathematik und Mechanik*, Vol. 13, No. 2, pp. 147-52, 1933.
6. TOMOTIKA, S. The Transverse Vibration of a Square Plate Clamped at Four Edges. *Phil. Mag.*, Series 7, Vol. 21, pp. 745-60, 1936.
7. COURANT. R. Variational Methods for the Solution of Problems of Equilibrium and Vibration. *Bulletin of the American Mathematical Society*, Vol. 49, pp. 1-23, 1939.
8. SOUTHWELL, R. V. On the Natural Frequencies of Vibrating Systems. *Proc. Roy. Soc.*, A, Vol. 174, pp. 433-57, 1940.
9. YOUNG, D. and FELGAR, R. P. Tables of Characteristic Functions Representing the Normal Modes of Vibration of a Beam. *Engineering Research Series*, No. 44, University of Texas. July 1949.

The Behaviour of Damped Linear Systems in Steady Oscillation

R. E. D. BISHOP

ADDENDUM TO THE PAPER PUBLISHED IN MAY 1956

In this paper (published in *The Aeronautical Quarterly*, Vol. VII, Part 2, p. 156, May 1956), a set of equations is derived giving the responses at the generalised co-ordinates $q_1, q_2, \ldots q_n$ which are caused by a harmonic generalised force $\Phi_s e^{i\omega t}$ corresponding to q_s. They are equations (26), namely

$$q_1 = \left[\frac{{}_1B_{1s}}{\xi_1 - \omega^2} + \frac{{}_2B_{1s}}{\xi_2 - \omega^2} + \ldots + \frac{{}_nB_{1s}}{\xi_n - \omega^2}\right]\Phi_s e^{i\omega t}$$

$$q_2 = \left[\frac{{}_1B_{2s}}{\xi_1 - \omega^2} + \frac{{}_2B_{2s}}{\xi_2 - \omega^2} + \ldots + \frac{{}_nB_{2s}}{\xi_n - \omega^2}\right]\Phi_s e^{i\omega t}$$

. . . . . .

. . . . . .

$$q_n = \left[\frac{{}_1B_{ns}}{\xi_1 - \omega^2} + \frac{{}_2B_{ns}}{\xi_2 - \omega^2} + \ldots + \frac{{}_nB_{ns}}{\xi_n - \omega^2}\right]\Phi_s e^{i\omega t}.$$

This note is concerned with a sentence which follows these equations which says (of them) that " . . . there is no longer any assurance that the ratios between the constants ${}_mB_{rs}$ in any column of partial fractions are the same for all co-ordinates q_s at which excitation is applied, since the previous limiting condition cannot now be applied. Thus the shapes of the ' modes ' which are associated with the various columns depend upon the nature of the applied harmonic excitation."

The " previous limiting condition " referred to the conservative system and meant letting ω approach a natural frequency at the same time as the amplitude of the excitation is diminished. In fact, this assurance *can* be obtained even for the damped system by letting

$$\omega^2 \longrightarrow \xi_m, \qquad \Phi_s \longrightarrow 0,$$

where $m = 1, 2, \ldots n$. But, in using this limiting process, the reservation must be made that it has only mathematical (and not its previous physical) meaning. Thus it is not necessary to draw the conclusion as to the variation of the resonant modes with the point of excitation.

Suppose that the limiting process is used. A set of ratios is found, namely

$$\Psi_1 : \Psi_2 : \ldots : \Psi_n : : {}_mB_{1s} : {}_mB_{2s} : \ldots : {}_mB_{ns},$$

where the Ψ's are the amplitudes of the q's. Now this ratio is that which is found to correspond with the root $\omega^2 = \xi_m$ of the equation

$$\Delta = 0,$$

where Δ is the n^{th} order determinant formed from the coefficients of equations (17) of the paper. It follows that it is immaterial which co-ordinate q_s is used in establishing the ratios by the limiting process since there is only one set to be found from the equation $\Delta = 0$.

This argument must be regarded as a purely mathematical one and, to see this, it is necessary to examine equations (17) of the paper. If the constants Φ_r are all zero in those equations, the relation $\Delta = 0$ is the condition that finite complex solutions for the Ψ's may exist. Now if the system is conservative, so that all the d_{rs} terms are zero, then the equations (17) are those of free vibration and the solutions referred to determine the principal modes; one set of ratios exists for each root of $\Delta = 0$. But if the d_{rs} are not zero, the homogeneous equations have no meaning, since the motion will not be harmonic and the d_{rs} have meaning only when it is.

It is commonly found that a modal shape of an aircraft which is found by a ground resonance test is dependent to some extent upon the point of excitation. For instance, the aircraft may be excited at a point on a wing at a resonant frequency and the corresponding modal shape determined by means of suitably-placed accelerometers. If, now, the excitation is applied athwartships with the same frequency at a point on the rear fuselage, the aircraft will again resonate. But discrepancies will be found between the second modal shape and the first which are such that the motion of the tail unit will be more pronounced in the former.

This effect is due to the existence of damping forces. It can be explained in a rough-and-ready fashion by consideration of the problem as one of elastic wave propagation within the structure. It will also be seen that it is not inconsistent with the foregoing argument that the modal shape associated with the numerators of any column of fractions is the same no matter what is the driving point of the system concerned.

When a particular column of fractions is brought to resonance, so that its contribution to the response predominates, other columns will account for some of the motion. The extent to which these extraneous modes modify the predominating mode depends upon (*a*) the damping forces present, (*b*) the proximity of other resonant frequencies and (*c*) the point of excitation. For, while the complex ratios between the numerators of other columns do not depend upon the point of excitation, the actual values of the numerators do.

INDEX TO VOLUME VII

AERODYNAMICS

See also Noise, Jet Flap, Stability.

Note on the Wave Drags of Untapered Wings with Streamwise Tips at Zero Lift, A. D. Young, p. 240 (August 1956).

On a Class of Laminar Viscous Flows Within One or Two Bounding Cones, A. J. A. Morgan, p. 225 (August 1956).

Perturbations of Supersonic Nozzle Flows, R. E. Meyer, p. 71 (February 1956).

ARMSTRONG, W. D. and W. R. HAWTHORNE

Shear Flow Through a Cascade, p. 247 (November 1956).

BISHOP, R. E. D.

The Behaviour of Damped Linear Systems in Steady Oscillation, p. 156 (May 1956).

Addendum, p. 353 (November 1956).

The General Theory of "Hysteretic Damping," p. 60 (February 1956).

BLADES

See Cascades, Vibration.

CADAMBE, V. and R. K. KAUL

The Natural Frequencies of Thin Skew plates, p. 337 (November 1956).

CASCADES

Shear Flow Through a Cascade, W. R. Hawthorne and W. D. Armstrong, p. 247 (November 1956).

CLIMB

See Performance.

COX, HUGH L. and BERTRAM KLEIN

Vibration of Isosceles Triangular Plates Having the Base Clamped and Other Edges Simply - Supported, p. 221 (August 1956).

CREEP

Buckling of Columns in the Presence of Creep, Sharad A. Patel, p. 125 (May 1956).

Creep Buckling, N. J. Hoff, p. 1 (February 1956).

HAWTHORNE, W. R. and W. D. ARMSTRONG

Shear Flow Through a Cascade, p. 247 (November 1956).

HEMP, W. S.

Fundamental Principles and Theorems of Thermo-Elasticity, p. 184 (August 1956).

HOFF, N. J.

Creep Buckling, p. 1 (February 1956).

HOLISTER, G. S., H. T. JESSOP and C. SNELL

Photoelastic Investigation on Plates with Single Interference-Fit Pins with Load Applied to Plate Only, p. 297 (November 1956).

JESSOP, H. T., C. SNELL and G. S. HOLISTER

Photoelastic Investigation on Plates with Single Interference-Fit Pins with Load Applied to Plate Only, p. 297 (November 1956).

JET FLAP

Early Thoughts on the Jet Flap, B. S. Stratford, p. 45 (February 1956).

Mixing and the Jet Flap, B. S. Stratford, p. 85 (May 1956).

A Further Discussion on Mixing and the Jet Flap, B. S. Stratford, p. 169 (August 1956).

KAUL, R. K. and V. CADAMBE

The Natural Frequencies of Thin Skew Plates, p. 337 (November 1956).

KLEIN, BERTRAM and HUGH L. COX

Vibration of Isosceles Triangular Plates Having the Base Clamped and Other Edges Simply - Supported, p. 221 (August 1956).

MARTIN, A. I.

Some Integrals Relating to the Vibration of a Cantilever Beam and Approximation for the Effect of Taper on Overtone Frequencies, p. 109 (May 1956).

MEYER, R. E.

Perturbations of Supersonic Nozzle Flows, p. 71 (February 1956).

MILES, JOHN W. and LEE WINOGRAD

Numerical Results for the Longitudinal Stability Derivatives and Stability Loci of a Low Aspect Ratio Rectangular Wing in Supersonic Flow, p. 106 (May 1956).

MORGAN, A. J. A.

On a Class of Laminar Viscous Flows Within One or Two Bounding Cones, p. 225 (August 1956).

NOISE

Supersonic Bangs, P. Sambasiva Rao. Part I, p. 21 (February 1956). Part II, p. 135 (May 1956).

PATEL, SHARAD A.

Buckling of Columns in the Presence of Creep, p. 125 (May 1956).

PERFORMANCE

An Energy Approach to Climb Performance Estimation of a Jet Transport Aircraft, R. B. Tamboli, p. 315 (November 1956).

PHOTOELASTICITY

Photoelastic Investigation on Plates with Single Interference-Fit Pins with Load Applied to Plate Only, H. T. Jessop, C. Snell and G. S. Holister, p. 297 (November 1956).

INDEX

RAO, P. SAMBASIVA
Supersonic Bangs
Part I, p. 21 (February 1956).
Part II, p. 135 (May 1956).

REVIEW
The Theory of Hydrodynamic Stability, by C. C. Lin. Reviewed by G. Temple, p. 246 (August 1956).

ROCKEY, K. C.
The Design of Intermediate Vertical Stiffeners on Web Plates Subjected to Shear, p. 275 (November 1956).

SHIMMY
The Theory and Prevention of Undamped Aeroplane Nosewheel Shimmy, D. Williams, p. 193 (August 1956).

SNELL, C., H. T. JESSOP and G. S. HOLISTER
Photoelastic Investigation on Plates with Single Interference-Fit Pins with Load Applied to Plate Only, p. 297 (November 1956).

STABILITY
Numerical Results for the Longitudinal Stability Derivatives and Stability Loci of a Low Aspect Ratio Rectangular Wing in Supersonic Flow, Lee Winograd and John W. Miles, p. 106 (May 1956).

STIFFENERS
The Design of Intermediate Vertical Stiffeners on Web Plates Subjected to Shear, K. C. Rockey, p. 275 (November 1956).

STRATFORD, B. S.
Early Thoughts on the Jet Flap, p. 45 (February 1956).
Mixing and the Jet Flap, p. 85 (May 1956).
A Further Discussion on Mixing and the Jet Flap, p. 169 (August 1956).

STRUCTURES
See Creep, Stiffeners, Thermo-Elasticity, Vibration.

SUPERSONIC BANGS
See Noise.

TAMBOLI, R. B.
An Energy Approach to Climb Performance Estimation of a Jet Transport Aircraft, p. 315 (November 1956).

THERMO-ELASTICITY
Fundamental Principles and Theorems of Thermo-Elasticity, W. S. Hemp, p. 184 (August 1956).

VIBRATION
Some Integrals Relating to the Vibration of a Cantilever Beam and Approximation for the Effect of Taper on Overtone Frequencies, A. I. Martin, p. 109 (May 1956).
The Behaviour of Damped Linear Systems in Steady Oscillation, R. E. D. Bishop, p. 156 (May 1956).
Addendum, p. 353 (November 1956).
The General Theory of "Hysteretic Damping," R. E. D. Bishop, p. 60 (February 1956).
The Natural Frequencies of Thin Skew Plates, R. K. Kaul and V. Cadambe, p. 337 (November 1956).
Vibration of Isosceles Triangular Plates Having the Base Clamped and Other Edges Simply-Supported, Hugh L. Cox and Bertram Klein, p. 221 (August 1956).

WEB PLATES
See Stiffeners.

WILLIAMS, D.
The Theory and Prevention of Undamped Aeroplane Nosewheel Shimmy, p. 193 (August 1956).

WINOGRAD, LEE and JOHN W. MILES
Numerical Results for the Longitudinal Stability Derivatives and Stability Loci of a Low Aspect Ratio Rectangular Wing in Supersonic Flow, p. 106 (May 1956).

YOUNG, A. D.
Note on the Wave Drags of Untapered Wings with Streamwise Tips at Zero Lift, p. 240 (August 1956).